

Jagiellonian University
Faculty of Physics, Astronomy and Applied Computer Science
Department of Advanced Materials Engineering



Ph.D. Thesis

Magnetic properties of molecular transition metals compounds

mgr Anna Małgorzata Majcher

Under the supervision of dr hab. Michał Rams

Kraków, 2013

*To my Mother
Mojej Mamie*

Abstract

In this Thesis, magnetic properties of several new molecular magnets, based on transition metals connected through cyanide bridges, were investigated by means of bulk and single crystal magnetic and heat capacity measurements. Five systems demonstrating interesting magnetic behaviour were described. A chiral compound based on $\text{Mn}^{\text{II}}\text{-Nb}^{\text{IV}}$ was found to be a weakly anisotropic, soft ferromagnet with ordering temperature of 43 K. Another molecular system, based on $\text{Co}^{\text{II}}\text{-W}^{\text{V}}$, occurred to be a strongly anisotropic, layered molecular magnet ordering below 6 K. Magnetic structure of the system was numerically simulated. The compound based on $\text{Ni}^{\text{II}}\text{-Nb}^{\text{IV}}$ was proven to be water-sensitive. The primary ferromagnetic phase existing below 12 K is destroyed by dehydration, which creates a spin glass-like phase, rehydration partly restores the original and creates an additional phase. Two analogous double-layer systems, based on $\text{Cu}^{\text{II}}\text{-Mo}^{\text{V}}$ and $\text{Cu}^{\text{II}}\text{-W}^{\text{V}}$, were found to have ordering temperatures of 27.5 and 32.8 K, respectively. Both exhibit a spin-flip transition. The last investigated molecular compound, $\text{Cu}^{\text{II}}\text{-Mo}^{\text{IV}}$, originally paramagnetic, showed noticeable photomagnetic effect upon violet and blue light irradiation. The Thesis is a detailed record of used experimental approach, demonstrates the variety of possible magnetic behaviour of molecular magnets and shows additional means to control the magnetization which will hopefully be of applicational use.

Streszczenie

W niniejszej pracy przedstawione są własności magnetyczne kilku nowych magnetyków molekularnych opartych na metalach przejściowych połączonych mostkami cyjankowymi. Badania próbek proszkowych i monokryształów przeprowadzono za pomocą magnetometrii i pomiarów ciepła właściwego. Opisano pięć interesujących związków. Chiralny związek oparty na $\text{Mn}^{\text{II}}\text{-Nb}^{\text{IV}}$ okazał się być miękkim ferrimagnetykiem o temperaturze porządkowania 43 K, wykazującym słabą anizotropię. Kolejny magnetyk molekularny, $\text{Co}^{\text{II}}\text{-W}^{\text{V}}$ o warstwowej strukturze, wykazał silną anizotropię. Porządkuje się on magnetycznie poniżej 6 K. Przeprowadzona została symulacja numeryczna jego uporządkowania magnetycznego. Własności magnetyczne związku opartego na $\text{Ni}^{\text{II}}\text{-Nb}^{\text{IV}}$ okazały się być zależne od stopnia nawodnienia próbki. Ferromagnetyczna faza pierwotna, istniejąca poniżej 12 K, jest niszczone przez wysuszenie próbki i powstaje faza przypominająca szkło spinowe. Ponowne nawodnienie przywraca częściowo fazę pierwotną i tworzy dodatkową. Dwa kolejne, analogiczne, dwuwarstwowe związki, $\text{Cu}^{\text{II}}\text{-Mo}^{\text{V}}$ i $\text{Cu}^{\text{II}}\text{-W}^{\text{V}}$, porządkują się magnetycznie poniżej odpowiednio 27.5 i 32.8 K. Oba wykazują przejście metamagnetyczne. Ostatni z badanych związków, bazujący na $\text{Cu}^{\text{II}}\text{-Mo}^{\text{IV}}$, pierwotnie paramagnetyczny, wykazał znaczący efekt fotomagnetyczny po naświetlenu światłem fioletowym i niebieskim. Praca ta zawiera również szczegółowy opis wykonanych eksperymentów, prezentuje mnogość możliwych własności magnetycznych materiałów molekularnych, a także pokazuje dodatkowe sposoby sterowania magnetyzacją, co może znaleźć zastosowania użytkowe.

Contents

Contents	i
1 Introduction	5
1.1 Molecular magnets	5
1.2 Magnetism and magnetic ordering	7
1.2.1 Definitions and the origin of magnetism	7
1.2.2 Magnetic properties of non-interacting localized magnetic moments	8
1.2.3 The interaction between metal centers in molecular magnets	12
1.2.4 Models of spontaneous long-range magnetic ordering	13
1.2.5 Anisotropy	19
1.3 Magnetic heat capacity	21
1.4 Photomagnetism	22
2 Experimental methods	23
2.1 Magnetometry	23
2.1.1 SQUID magnetometry - the idea	23
2.1.2 Quantum Design MPMS XL system	26
2.1.3 Horizontal Sample Rotator	27
2.1.4 Fiberoptic Sample Holder	29
2.2 Heat capacity measurements	31
2.2.1 Heat capacity measurements - the idea	31
2.2.2 Quantum Design PPMS	31
3 Results and analysis	35
3.1 A new chiral molecular magnet: 3D cyano-bridged $\text{Mn}^{\text{II}} - \text{Nb}^{\text{IV}}$. .	35
3.1.1 Structure	35
3.1.2 Experimental	37
3.1.3 Magnetic studies of $\text{Mn}_2^{\text{II}} - \text{Nb}^{\text{IV}}$	41
3.1.4 Summary	50

3.2	Magnetic anisotropy of $\text{Co}_3^{\text{II}} - \text{W}_2^{\text{V}}$ ferromagnet	51
3.2.1	Structure	51
3.2.2	Experimental	53
3.2.3	Magnetic studies of $\text{Co}_3^{\text{II}} - \text{W}_2^{\text{V}}$	55
3.2.4	Heat capacity measurement of $\text{Co}_3^{\text{II}} - \text{W}_2^{\text{V}}$	70
3.2.5	Summary	73
3.3	$\text{Ni}_2^{\text{II}} - \text{Nb}^{\text{IV}}$ - a water sensitive ferromagnetic network	74
3.3.1	Structure	74
3.3.2	Experimental	74
3.3.3	Magnetic properties of $\text{Ni}_2^{\text{II}} - \text{Nb}^{\text{IV}}$	75
3.3.4	Summary	82
3.4	$\text{Cu}^{\text{II}} - \text{Mo}^{\text{V}}$ and $\text{Cu}^{\text{II}} - \text{W}^{\text{V}}$ with incorporated guanidinium ions: double-layers magnetic system	83
3.4.1	Structure	83
3.4.2	Experimental	84
3.4.3	Magnetic properties of $\text{Cu}^{\text{II}} - \text{Mo}^{\text{V}}$ and $\text{Cu}^{\text{II}} - \text{W}^{\text{V}}$	84
3.4.4	Heat capacity measurement for $\text{Cu}^{\text{II}} - \text{Mo}^{\text{V}}$	93
3.4.5	Summary	95
3.5	$\text{Cu}_2^{\text{II}} - \text{Mo}^{\text{IV}}$ - a photosensitive magnetic network	96
3.5.1	Structure	96
3.5.2	Experimental	96
3.5.3	Light absorption measurements	97
3.5.4	Magnetic properties and photomagnetism of $\text{Cu}_2^{\text{II}} - \text{Mo}^{\text{IV}}$	98
3.5.5	Summary	101
4	Summary	103
	Bibliography	113
	List of Figures	119
	List of Tables	125

Acknowledgements

I want to thank several people who made writing this Thesis possible and helped me on the way:

- My supervisor **dr hab. Michał Rams** for his assistance, support and guidance, and for many valuable discussions leading to my better understanding of the science of molecular magnets.
- The whole **prof. dr hab. Barbara Sieklucka's group**, in particular **dr Dawid Pinkowcz**, **Szymon Chorąży**, **dr Beata Nowicka** and **Olaf Stefańczyk** for preparing the compounds investigated in this Thesis, the help with their structure characteristics and understanding their chemistry.
- My friends from the Institute of Physics: **Natalia Tomaszewska**, **Magdalena Halastra**, **Agnieszka Korpała** and **Aleksandra Kubica** for their constant presence, support and brightening my days.
- My **Father** who led me onto the path of Science and my **Mother** who always supported me following it. Thank you for your unconditional love, care and presence.
- My fiancé **Ravi Kumar Krishnappa** for the love, understanding and support in the fight for the better future.

Foreword

This Thesis is focused on investigating the magnetic properties of several new molecular magnets. The subject of molecular magnetism is interdisciplinary, connecting advanced chemical syntheses and thorough characterisation of physical properties of this new class of materials with many possible future applications. This Thesis is a set of examples of different new molecular magnets and their magnetic behaviour, chosen from over a hundred samples measured by the author.

All the samples were synthesised by prof. dr hab. Barbara Sieklucka's Inorganic Molecular Materials Group from the Jagiellonian University that also provided us with structural characterization. Each of the samples was thoroughly investigated by the author for magnetic properties, and each displayed different and fascinating magnetic behaviour, dependent on external conditions varying from case to case.

The structure of this Thesis can be outlined as follows:

- Chapter 1 gives the theoretical basis necessary to understand the class of materials which are molecular magnets and their physics, a detailed introduction on magnetic behaviour of matter and a brief overview of magnetic heat capacity and photomagnetism.
- Chapter 2 presents an overview of the experimental methods used to investigate the physical properties of these systems, specifically magnetometry and heat capacity measurements.
- Chapter 3 displays the results of the magnetic measurements of five different molecular transition metals compounds with the analysis and conclusions on each compound, some accompanied by heat capacity measurements, resulting in thorough magnetic characterization for all the analyzed samples.
- Chapter 4 contains a summary and comparison of the results presented in Chapter 3.

- The Appendices contain a brief chapter on magnetic units and a short explanation about demagnetization corrections.
- The Thesis ends with a Bibliography containing the references used in this work, the List of all author's publications, a List of Figures and a List of Tables.

Chapter 1

Introduction

1.1 Molecular magnets

Molecular magnets are organic or inorganic/organic hybrid materials, comprised of discrete molecular building blocks (organic molecules, coordination complexes). Unlike the classical magnets, for which magnetic properties arise from a network of magnetic moments, their magnetic properties are of molecular origin, the building blocks arranging into zero-, one-, two- or three-dimensional arrays.

Molecular magnets are produced in a bottom-up approach, where the techniques of molecular chemistry are employed in order to design and synthesise new classes of magnetic materials. Compared to the classical magnets, molecular magnets are already dispersed and are also soluble in different solvents or can be placed in some other matrix, like a polymer, and they will still show the same magnetic properties.

Such molecular systems have features which can be considered both in classical (e.g. magnetic hysteresis, switching, exchange coupling) as well as in quantum (e.g. quantum tunnelling of magnetisation) regime [1].

The most astonishing example of molecular magnetic materials is a single molecule magnet (SMM). It can be magnetized in a magnetic field, and it will remain magnetized even after switching off the field, which is a property of the molecule itself. No interaction between the molecules is necessary for this phenomenon to occur. This gives an opportunity for a more dense data storage than the classical one.

The most famous molecular magnet, discovered in 1980, is a dodecanuclear manganese cluster of formula $[\text{Mn}_{12}\text{O}_{12}(\text{CH}_3\text{COO})_{16}(\text{H}_2\text{O})_4] \cdot 4\text{H}_2\text{O} \cdot 2\text{CH}_3\text{COOH}$ for short called Mn_{12}Ac [2]. A sketch of this molecule is shown in Fig. 1.1.

The Mn^{III} ions form an external octanuclear ring, and the Mn^{IV} an internal tetrahedron. The ground state is $S = 10$ (all the spins of Mn^{III} $S = 2$ up and

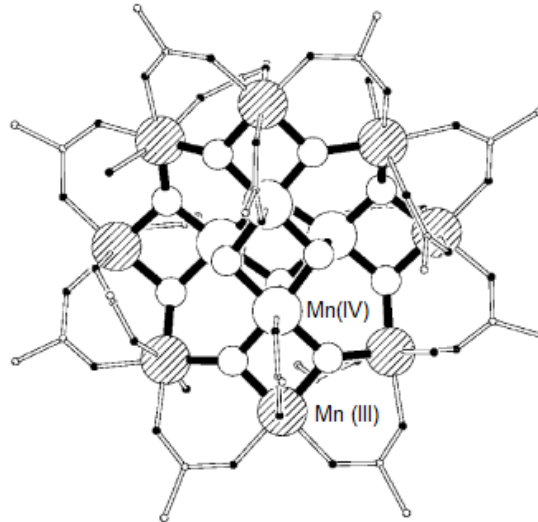


Figure 1.1: A schematic picture of the first historic molecular magnet, Mn_{12}Ac . Source: [3]

Mn^{IV} $S = 3/2$ down). It showed a magnetic hysteresis of a purely molecular origin, with a characteristic stepped curve, and the relaxation time was estimated to be 50 years at 1.5 K. This gave the idea of storing information in a single molecule and opened the possibility of molecular density data storage. Also, relaxation through quantum tunneling was first observed in mesoscopic magnets in this system, and this was possible due to the absolute mono-dispersion of the Mn_{12}Ac molecules [3].

Later, many types of molecular magnets were synthesised:

- Molecular organic magnets based on s- and p- electrons and polymers (the only known type before 1990s)
- Molecular inorganic-organic magnets
 - Oxalato-based 1D-, 2D-, and 3D-magnets
 - Cyano-based magnets (on which this work is focused)
- Finite Cluster Compounds (SMMs)
- Molecular Single Chain Magnets
- Magnetic Molecular Wheels

to mention only a few types [1].

1.2 Magnetism and magnetic ordering

1.2.1 Definitions and the origin of magnetism

Magnetic moment of an electron

Magnetism has its origin in the motion of charged particles, and the intrinsic magnetic moments (*spins*), of particles. The definition of the magnetic moment due to movement of charge is

$$\vec{\mu} = I\vec{S},$$

where \vec{S} is a vector area enclosed by the current loop. From this, an *angular orbital magnetic moment* of an electron on its orbit can be calculated

$$\vec{\mu}_l = I\vec{S} = \frac{-e\omega}{2\pi} \cdot \pi r^2 = \frac{-e}{2m_e c} \hbar \vec{l} = -\mu_B \vec{l},$$

where $\hbar \vec{l}$ is the orbital angular momentum ($l = 0, 1, 2, \dots$ is the quantum number describing the orbit, s, p, d, ... respectively), $\mu_B = e\hbar/2m_e c = 9.27400968(20) \cdot 10^{21} \text{ erg} \cdot \text{G}^{-1}$ is the Bohr magneton, and other symbols have their usual meaning. An electron has an intrinsic angular momentum, spin \vec{s} (derived from the Dirac equation):

$$\vec{\mu}_s = -g_s \frac{e}{2m_e c} \hbar \vec{s} \approx -2\mu_B \vec{s},$$

where $g_s = 2.002319 \approx 2$ is the electron g -factor [4] and \vec{s} is the spin. Thus, the total intrinsic magnetic moment of an electron is

$$\vec{\mu}_{int} = -\mu_B(\vec{l} + 2\vec{s}).$$

Spin-orbit coupling

An electron moving on the orbit sees the electric field of the nucleus partly as a magnetic field, which interacts with the spin of the electron. The energy shift calculated for this phenomenon is:

$$\Delta E = \frac{1}{2m_e^2 c^2} \frac{1}{r} \frac{\partial U}{\partial r} \vec{l} \cdot \vec{s},$$

where $U = V \cdot e$ is the potential energy of the electron in the central field. When we take into account all the electrons in the shell

$$\vec{L} = \sum_i \vec{l}_i, \quad \vec{S} = \sum_i \vec{s}_i, \quad \vec{J} = \vec{S} + \vec{L}.$$

For a closed shell, owing to the Pauli exclusion principle, $\vec{L} = \vec{S} = 0$. For an underfilled shell

$$\Delta E = \xi \cdot \vec{L} \cdot \vec{S}.$$

The energy of the state depends on the value of the total angular momentum \vec{J} . The spin - orbit interaction is, therefore, responsible for splitting of energy levels in atomic spectra, but each of the energy levels is $(2J+1)$ times degenerate, as determined by the possible values of $m_J = -J, \dots, +J$.

The Zeeman effect

Now, we have to take into account the interaction of the magnetic moment with the external magnetic field $E = -\vec{\mu} \cdot \vec{H}$. The $(2J+1)$ degeneracy is removed by applying an external magnetic field, which leads to further splitting of electron energy levels into $(2J+1)$ states and is known as the Zeeman effect. The potential energy of the atom in an applied external magnetic field H is:

$$E = m_J g_L \mu_B H,$$

where g_L is the Landé factor:

$$g_L = \frac{J(J+1) + S(S+1) - L(L+1)}{2J(J+1)}.$$

1.2.2 Magnetic properties of non-interacting localized magnetic moments

Having learned the quantum origin of magnetism, we can now discuss the possible magnetic behaviour of the matter and how to recognize it. Before we start analyzing the magnetic behaviour of substances, however, we need one more definition - the magnetic susceptibility χ :

$$\chi = \frac{\langle \mu \rangle}{H},$$

where H is the external field applied to the sample and $\langle \mu \rangle$ is the average magnetic moment along the \vec{H} direction per unit volume. χ has no dimension. Often $\langle \mu \rangle$ is calculated not per unit volume, but per mole or per gram, the molar (or mass) susceptibility gaining a unit $\text{cm}^3 \text{mol}^{-1}$ or $\text{cm}^3 \text{g}^{-1}$, respectively (see Appendices: Units in Magnetism).

Diamagnetism

Diamagnetism is an underlying property of matter. In a case when no magnetic interactions have to be taken into account, the total susceptibility of the sample is a sum of paramagnetic and diamagnetic susceptibilities [5]:

$$\chi = \chi_D + \chi_P.$$

The value of χ_D is negative, independent of the temperature and the strength of the applied field, and can be calculated from quantum mechanics (per one electron):

$$\chi_D = -\frac{e^2 \langle r^2 \rangle}{6m_e}.$$

where $\langle r^2 \rangle$ is the average squared radius of the orbit and the other symbols have their usual meaning. χ_D depends on the size of the atoms and is tabulated for different ions in so-called Pascal tables [6].

For bulk molecular samples, it can be roughly estimated:

$$\chi_D = \kappa M \cdot 10^{-6} \text{cm}^3 \text{mol}^{-1},$$

where M is the molecular weight of the compound and $\kappa = 0.4 \div 0.5$ [5].

When χ_D is dominant, the total susceptibility is also negative and the substance is considered diamagnetic. Fig. 1.2 shows the schematic behaviour of a diamagnetic substance.

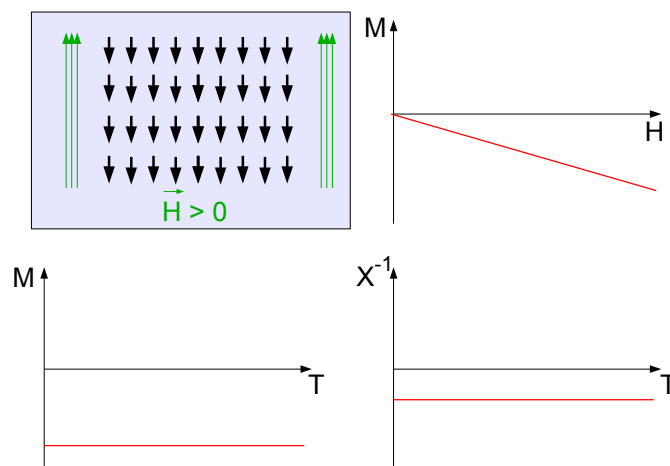


Figure 1.2: A schematic drawing of the field-induced magnetic moments in a purely diamagnetic substance, the macroscopic magnetization versus field, magnetization versus temperature and inverse magnetic susceptibility versus temperature.

The magnetic moments in a purely diamagnetic substance are induced by an external magnetic field and are directed opposite to the field. The magnetic moment of the system is then independent of the temperature and changes linearly with the magnetic field.

An example of this behaviour is observed for the gelatine capsule used as a sample holder for the measurements and described in Chapter 3.1.2.

Paramagnetism

The paramagnetic susceptibility χ originates from unequal thermal occupation of energy levels E_n in the applied magnetic field H . The microscopic magnetic moment of an energy level n is equal to

$$\mu_n = -\frac{\partial E_n}{\partial H}.$$

The macroscopic molar magnetization is then the sum of μ_n weighed by the Boltzmann distribution law:

$$M = \frac{N_A \sum_n (-\partial E_n / \partial H) \cdot \exp(-E_n / kT)}{\sum_n \exp(-E_n / kT)}, \quad (1.1)$$

where $k = 1.3806488(13) \cdot 10^{-16}$ erg \cdot K $^{-1}$ is the Boltzmann constant. This expression is the fundamental expression of molecular magnetism [5].

If we define a partition function

$$Z = \sum_n \exp(-E_n / kT),$$

then, after a few simple transformations, we obtain a formula for molar paramagnetic susceptibility

$$\chi = N_A kT \frac{\partial^2 \ln Z}{\partial H^2}.$$

This formula requires the knowledge of E_n as a function of the field H . A solution was proposed by Van Vleck in 1932. He expanded the energies E_n according to the increasing powers of H :

$$E_n = E_n^{(0)} + E_n^{(1)} \cdot H + E_n^{(2)} \cdot H^2 + \dots$$

then

$$\mu_n = -E_n^{(1)} - 2E_n^{(2)} \cdot H + \dots$$

Another assumption is that H/kT is small. The exponent in (1.1) becomes

$$\exp(-E_n / kT) = \exp(-E_n^{(0)} / kT) (1 - E_n^{(1)} H / kT).$$

Including these two approximations into equation (1.1) we obtain:

$$M = \frac{N_A \sum_n (-E_n^{(1)} - 2E_n^{(2)} \cdot H) \exp(-E_n^{(0)} / kT) (1 - E_n^{(1)} H / kT)}{\sum_n \exp(-E_n^{(0)} / kT) (1 - E_n^{(1)} H / kT)}. \quad (1.2)$$

We have to add another condition of magnetization vanishing in zero field:

$$\sum_n E_n^{(1)} \exp(-E_n^{(0)} / kT) = 0. \quad (1.3)$$

After incorporating (1.3) into (1.2), we obtain a formula for M , and therefore for the susceptibility as a function of temperature:

$$\chi = \frac{N_A \sum_n ((E_n^{(1)})^2/kT - 2E_n^{(2)}) \exp(-E_n^{(0)}/kT)}{\sum_n \exp(-E_n^{(0)}/kT)}, \quad (1.4)$$

which is the Van Vleck formula. Values of $E_n^{(0)}$ are the eigenvalues of the Hamiltonian in the zero field, while $E_n^{(1)}$ and $E_n^{(2)}$ can be calculated from the perturbation theory:

$$E_n^{(1)} = \langle n | H_Z | n \rangle$$

$$E_n^{(2)} = \sum_m \frac{\langle n | H_Z | m \rangle^2}{E_n^{(0)} - E_m^{(0)}} \quad E_m^{(0)} \neq E_n^{(0)}$$

where $H_Z = \mu_B \sum_i (\vec{l}_i + 2\vec{s}_i) \cdot \vec{H}$ is the Zeeman Hamiltonian and $|n\rangle$ are the eigenstates of the Hamiltonian in the zero field [5].

A paramagnetic substance is the simplest case of magnetic behaviour. If we assume a situation in which the ground state has no first-order angular momentum ($\vec{L} = 0$) and has a large separation energy from the first excited states [5] - there is no magnetic coupling between the spin carriers. When an external magnetic field is applied, the energies of $2S + 1$ Zeeman components are given by

$$E_n = m_S g_s \mu_B H, \quad m_S = -S, \dots, +S.$$

The energies E_n are linear in H , so the second order Zeeman coefficients vanish and the Van Vleck formula (1.4) simplifies to

$$\chi = \frac{N_A \sum_n (E_n^{(1)})^2 \exp(-E_n^{(0)}/kT)}{kT \sum_n \exp(-E_n^{(0)}/kT)}. \quad (1.5)$$

If the temperature is large and H/kT is small, then $E_n^{(0)} = 0$ and $E_n^{(1)} = m_S g \mu_B$, we obtain a formula

$$\chi = \frac{N_A g^2 \mu_B^2}{3kT} S(S+1) \equiv \frac{C}{T}, \quad (1.6)$$

which is known as the **Curie law** that describes the behaviour of a paramagnet in large temperatures.

In the case of large H/kT , the magnetization reaches a value called the saturation value $M_{\text{sat}} = N_A g \mu_B S$ when all the spins align parallel to the applied magnetic field. The magnetization versus field dependence of a paramagnet is well described, without regard to the magnitude of H/kT , by the Brillouin function, which is given below:

$$\frac{M}{M_{\text{sat}}} = B_S(y),$$

where $B_S(y)$ is the Brillouin function:

$$B_S(y) = \frac{2S+1}{2S} \coth\left(\frac{2S+1}{2S}y\right) - \frac{1}{2S} \coth\left(\frac{1}{2S}y\right),$$

and y is defined by:

$$y = \frac{g\mu_B SH}{kT}.$$

The macroscopic behaviour of a paramagnetic substance is illustrated in fig. 1.3.

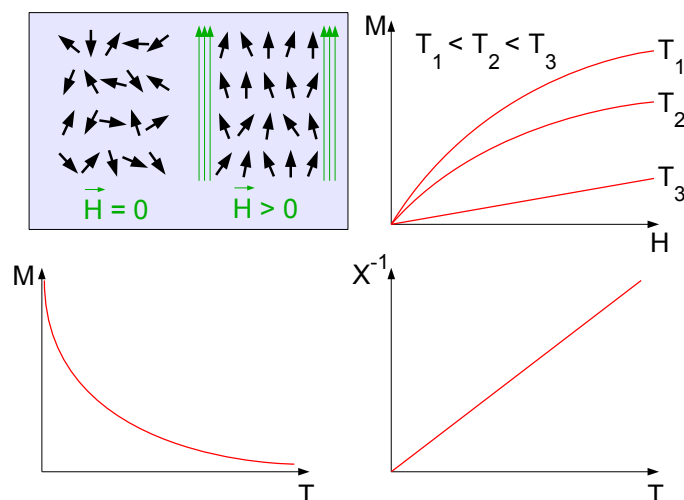


Figure 1.3: A schematic drawing of the spin alignment in a paramagnetic substance without (left) and with applied magnetic field (right), together with the macroscopic magnetization versus field, magnetization versus temperature and inverse magnetic susceptibility versus temperature which obeys the Curie law.

An example of such behaviour was observed for a compound described in Chapter 3.5.

1.2.3 The interaction between metal centers in molecular magnets

In the case of the molecular compounds of transition metals investigated in this Thesis, the magnetic moments are localized on the transition metals atoms which are a part of the crystal structure. Their magnetism originates from partially filled d atomic shell: in the case of Mn, Co, Ni, Cu it is the $3d$, in the case of Nb and Mo - the $4d$ and in the case of W - the $5d$ shell. The metal centers are connected with CN molecular bridges bridges ($M_1 - CN - M_2$) through which coupling between them can occur. It usually happens in the mechanism of superexchange interaction (described well by the Heisenberg Hamiltonian, see Chapter 1.2.4): the singly-occupied orbitals of the magnetic centers overlap indirectly through the relevant orbital(s) of the molecular bridge.

This mechanism can lead to two situations [5], [7]:

- **Antiferromagnetic:** the two magnetic centers M_1 and M_2 have one singly occupied $d_{x^2-y^2}$ orbital each and are connected by a linear CN bridge. The overlap of $d_{x^2-y^2}$ of both the magnetic centers and the antibonding π^* CN molecular orbital can lead to the partial backdonation of the spin density from both metal centers to the ligand. Such superexchange pathway can only lead to the antiferromagnetic interaction due to the Pauli exclusion principle.
- **Ferromagnetic:** M_1 has one singly occupied $d_{x^2-y^2}$ orbital and M_2 's unpaired electron is localized on its d_{xy} orbital. In this situation, there is no efficient overlap - d_{xy} is orthogonal to CN's π^* and ferromagnetic interaction is allowed.

The situations presented above concern only two neighbouring metal centers. However, in a situation where all magnetic centers are close enough to interact or are all connected through molecular bridges, a possibility of long-range magnetic ordering has to be acknowledged.

1.2.4 Models of spontaneous long-range magnetic ordering

In this Section systems with an existing coupling mechanism between the metal centers and therefore with magnetic ordering below a critical temperature T_C will be described.

In general, the coupling between the spins is well described by the Heisenberg Hamiltonian:

$$H_H = - \sum_{i,j} J_{ij} \vec{s}_i \cdot \vec{s}_j,$$

where J_{ij} is the interaction parameter between two neighbouring spins on sites i and j . $J_{ij} > 0$ indicates ferromagnetic coupling, while $J_{ij} < 0$ – antiferromagnetic. If we consider the case of a single spin, with a field applied along the z direction, $J_{ij} = J$ for a pair of nearest neighbours, the total Hamiltonian can be written as:

$$H = g\mu_B S_z H - Jz \langle S_z \rangle S_z,$$

where z is the number of neighbours. The eigenvalues are thus

$$E(S, m_S) = m_S(g\mu_B H - Jz \langle S_z \rangle).$$

$\langle S_z \rangle$ can be calculated from the Boltzmann distribution

$$\langle S_z \rangle = \frac{\sum_{m_S=-S}^S m_S \exp(-E(S, m_S)/kT)}{\sum_{m_S=-S}^S \exp(-E(S, m_S)/kT)},$$

which can be simplified, after expanding the exponents up to the first order, into

$$\langle S_z \rangle = \frac{\sum_{m_S=-S}^S m_S [1 - m_S(g\mu_B H - Jz \langle S_z \rangle)/kT]}{\sum_{m_S=-S}^S [1 - m_S(g\mu_B H - Jz \langle S_z \rangle)/kT]}.$$

After the summation, an expression for $\langle S_z \rangle$ can be extracted:

$$\langle S_z \rangle = -\frac{S(S+1)g\mu_B H}{3kT - zJS(S+1)}.$$

For a polyatomic system in the molecular field approximation, the magnetization per one mole of substance is

$$M = N_A \cdot \langle m \rangle = -N_A g \mu_B \langle S_z \rangle,$$

from which a formula for susceptibility $\chi = \partial M / \partial H$ can be concluded:

$$\chi = \frac{N_A g^2 \mu_B^2 S(S+1)}{3kT - zJS(S+1)} \equiv \frac{C}{T - \theta},$$

which is known as the **Curie-Weiss law**. C is the previously defined Curie constant and θ is the Weiss temperature

$$\theta \equiv \frac{zJS(S+1)}{3k}.$$

It indicates the intermolecular interactions: positive value means ferromagnetic, negative - antiferromagnetic interactions [5].

The Weiss theory predicts $\theta = T_C$, but in fact it is only an upper limit for the critical temperature, which is often decreased by short range of the interactions and the quantum nature of the moments [8].

All the compounds investigated in Chapters 3.2 – 3.4 are Curie-Weiss paramagnets in high temperatures.

Ferromagnetism

In a ferromagnetic substance, the moments tend to align parallel to each other giving rise to a spontaneous magnetization below T_C even without applying the external magnetic field. The typical behaviour of a ferromagnetic sample is depicted in fig. 1.4.

The magnetization in zero temperature rises instantly to its saturation value (meaning all the moments aligned in the same direction). Closer to the T_C , spontaneous magnetization is still present, but the saturation value is reached only in higher fields (T_1 in fig. 1.4). Above the T_C , spontaneous magnetization vanishes and the sample becomes paramagnetic. Inverse susceptibility obeys the Curie-Weiss law above the T_C with a positive θ value.

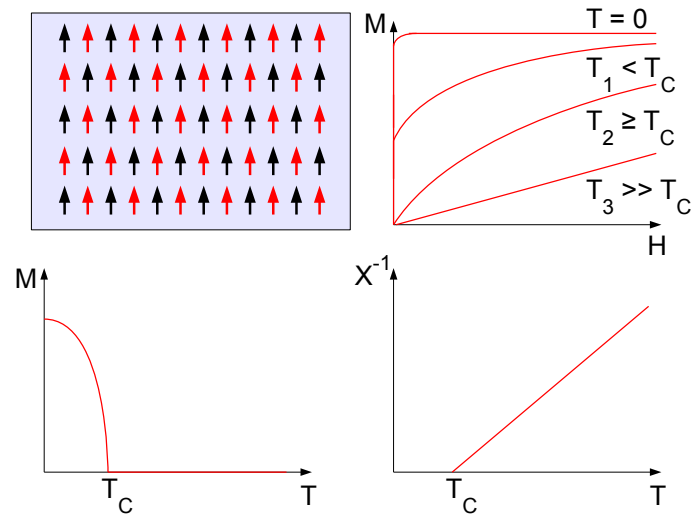


Figure 1.4: A schematic drawing of the spin alignment in a ferromagnetic substance, together with the macroscopic magnetization versus field in different temperatures, magnetization versus temperature and inverse magnetic susceptibility versus temperature which obeys the Curie-Weiss law above T_C .

Despite exhibiting spontaneous magnetization below T_C , a sample of a ferromagnet is not necessarily magnetised due to the existence of magnetic domains. Ferromagnetic materials may display a **hysteresis** below T_C (fig. 1.5).

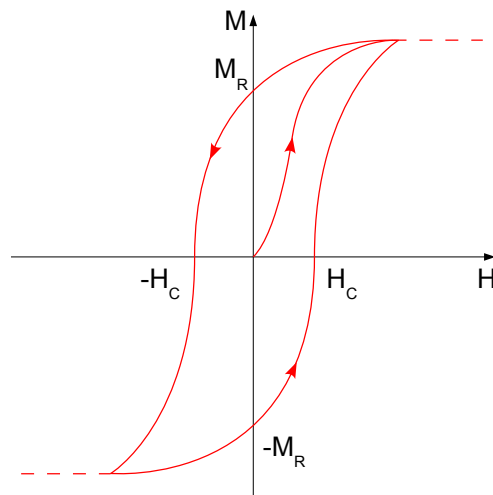


Figure 1.5: A schematic drawing of a typical ferromagnetic hysteresis loop close to $T = 0$ K. H_C - coercivity field, M_R - remnant magnetization.

Starting at the zero point ($M = 0, H = 0$), below T_C , a positive field is applied,

giving rise to the *initial magnetization curve*. Then the field is lowered back to zero, however, a *remnant magnetization* M_R is displayed by the sample in $H = 0$. Further applying a field of negative direction lowers the magnetization to zero at $H = H_C$, which is called *the coercive field*. The process is symmetric and further changes of the field in positive and negative direction will cause the magnetization to follow the hysteretic loop. Increase in the temperature will cause the loop to shrink (lower value of H_C) and magnetization will not reach its saturation value as soon as in fig. 1.5. When the critical temperature is reached, the loop vanishes completely.

Most technological applications of hard magnetic materials and magnetic recording rely on the existence of the hysteresis [9]. Compounds investigated in Chapters 3.2 – 3.4 display ferromagnetic behaviour and hysteresis loops.

Antiferromagnetism

In the case of an antiferromagnetic substance, the magnetic interactions tend to align the neighbouring moments antiparallel to each other and, as a result, there is no spontaneous magnetization below the critical temperature, which in case of the antiferromagnet is called the Néel temperature T_N .

In the simplest case, an antiferromagnet can be imagined as two identical interpenetrating ferromagnetic sublattices, which respective magnetizations are of identical value but opposite directions. The behaviour of an antiferromagnet is shown in fig. 1.6.

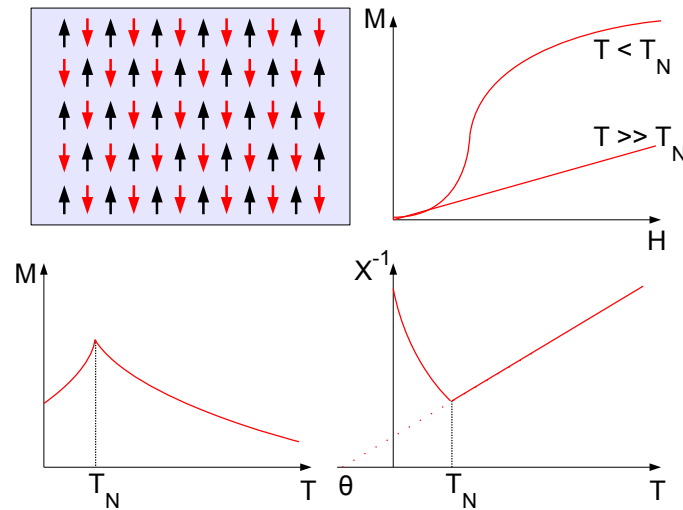


Figure 1.6: A schematic drawing of the spin alignment in an antiferromagnetic substance, together with the macroscopic magnetization versus field in different temperatures, magnetization versus temperature and inverse magnetic susceptibility versus temperature which obeys the Curie-Weiss law above T_N .

The magnetization behaviour in field is similar to the one of a paramagnet in high temperatures. In temperatures below T_N , a spin-flip transition may occur when the external field is strong enough to overcome the molecular field and align all the spins in the same direction. The difference between antiferromagnetism and other types of magnetic ordering is clearly visible in the inverse susceptibility as a function of temperature - it has a minimum at T_N and it obeys the Curie-Weiss law in higher temperatures with a negative value of θ .

Examples of spin-flip transitions can be found in Chapters 3.2 and 3.4.

Ferrimagnetism

A ferrimagnet is a substance much like the antiferromagnet, but in this case the sublattices do not exactly compensate each other and a spontaneous magnetization remains. That may happen due to the sublattices being composed of atoms of different spins and/or to unequal number of atoms in each sublattice. Ferrimagnetism was predicted by L. Néel before being confirmed by experiment [9]. In the molecular field model, two colinear sublattices are considered, with different magnetizations, M_A and M_B . Let $w_{AB} = w_{BA} = -w$ ($w > 0$), $w_{AA} = \alpha_A w$ and $w_{BB} = \alpha_B w$ (w_{AA} and $w_{BB} > 0$) be the various molecular field coefficients. The Curie constants of the sublattice i , $C_i = N_A g^2 S_i(S_i + 1) \mu_B^2 / 3k_B$ ($i = A, B$). In this model, the susceptibility is predicted to be:

$$\frac{1}{\chi} = \frac{T - \theta_P}{C} - \frac{\gamma}{T - \theta}, \quad (1.7)$$

where in general case:

$$C = C_A + C_B, \quad (1.8)$$

$$\theta = \frac{w(2 + \alpha_A + \alpha_B)C_A C_B}{C_A + C_B}, \quad (1.9)$$

$$\gamma = \frac{w^2 C_A C_B [C_A(1 + \alpha_A) - C_B(1 + \alpha_B)]^2}{(C_A + C_B)^3}, \quad (1.10)$$

$$\theta_P = w \frac{\alpha_A C_A^2 + \alpha_B C_B^2 - 2C_A C_B}{C_A + C_B}. \quad (1.11)$$

In a simple case of sublattices interacting only with each other and assuming that there are no interactions between atoms of the same sublattice, equation (1.7) becomes much easier for application. In such a case we assume $\alpha_A = 0 = \alpha_B$. Equations (1.9) and (1.11) can be now summarized in one:

$$\theta = \frac{2w C_A C_B}{C_A + C_B} = -\theta_P, \quad (1.12)$$

and the equation (1.10) becomes:

$$\gamma = w^2 \frac{C_A C_B (C_A - C_B)^2}{(C_A + C_B)^3}. \quad (1.13)$$

Having incorporated both equations (1.12) and (1.13) into eq. (1.7), we obtain a formula:

$$\frac{1}{\chi} = \frac{T^2 - w^2 C_A C_B}{T(C_A + C_B) - 2w C_A C_B} \quad (1.14)$$

This model describes the susceptibility well in high temperatures. The reciprocal susceptibility follows a hyperbolic law, with the following asymptotes: in high temperatures a Curie-Weiss line with $\theta_{CW} = \theta_P$ and near the critical temperature a vertical asymptote $T = \theta$ (see fig. 1.7). The above model was used to interpret the data in Chapter 3.1.

The behaviour of a macroscopic ferrimagnetic sample is gathered in fig. 1.7. Below T_C , and in the absence of the external magnetic field, there are two typical cases of the behaviour of the magnetization (depicted in fig. 1.7 in red and green). The first case is similar to the ferromagnetic behaviour, while in the second the spontaneous magnetization passes through zero at a *compensation temperature* $T_{comp} < T_C$. This case occurs when the thermal variation of the magnetization of the sublattice which dominates over that of the other at low temperatures is faster than the other [9]. Magnetization versus field resembles the one of a ferromagnet – with the spontaneous magnetic moment vanishing in T_C .

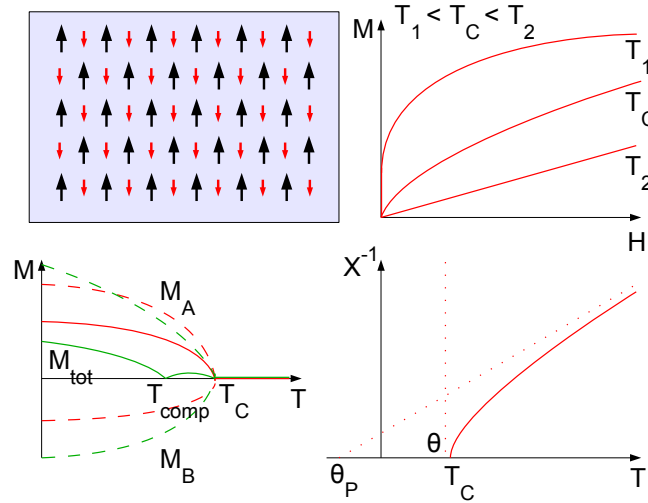


Figure 1.7: A schematic drawing of the spin alignment in a ferrimagnetic substance at $T = 0$, together with the macroscopic magnetization versus field in different temperatures, magnetization versus temperature (two typical cases in red and green) and inverse magnetic susceptibility.

Other types of magnetic freezing: spin glasses

The situations described above are the basic cases of magnetic ordering. There are more complicated situations, like spin glasses, which are disordered materials with different interactions, both ferromagnetic and also antiferromagnetic, which are randomly distributed. Below a certain temperature (called the *freezing* temperature T_f) the spins freeze into a glass-like disordered state with randomly distributed, finite, locally ordered clusters [10].

The main features of a spin glass are:

- Paramagnetic behaviour above the freezing temperature T_f .
- Characteristic shape of zero-field cooling/field cooling magnetization, with small irreversibility.
- A peak in χ' , accompanied by a relaxation process visible in χ'' .
- A distorted hysteresis in magnetization versus field dependence in $T < T_f$, lack of saturation.

Spin glasses are a broad subject and a wider description can be found in [10], [11].

Spin glass-like behaviour is suspected for two samples described in Chapter 3.3.

1.2.5 Anisotropy

Magnetic anisotropy is a situation when the ferro/antiferromagnetic axis of a compound lies along fixed direction(s) (called the *easy axis(es)*). The stronger the anisotropy, the *harder* the magnet. This tendency is represented by the *anisotropy energy* E_a , in which the leading term is

$$E_a = K_1 \sin^2 \zeta, \quad (1.15)$$

where K_1 is the anisotropy constant and ζ is the angle between the magnetization and the easy axis.

Anisotropy limits the coercivity available in hard magnets:

$$H_C < 2K_1/M_S,$$

and it also leads to unwanted coercivity in soft magnets.

There are three main sources of anisotropy:

- *Shape anisotropy* depends on the sample's shape and derives from demagnetizing field (see Appendices).

- *Magnetocrystalline anisotropy* which is an intrinsic property of the substance. The magnetization behaves differently when field is applied along different crystallographic directions, and usually the anisotropy reflects the crystal's symmetry. It originates from the crystal-field interaction and spin-orbit coupling, or else the interatomic dipole-dipole interaction.
- *Induced anisotropy* is caused by applied stress or by depositing or annealing a disordered compound in a magnetic field.

In the case of molecular magnets, the second case is to be considered.

The magnetization of anisotropic single crystals approaches the saturation differently in fields applied along different directions. This is summarized in fig. 1.8.

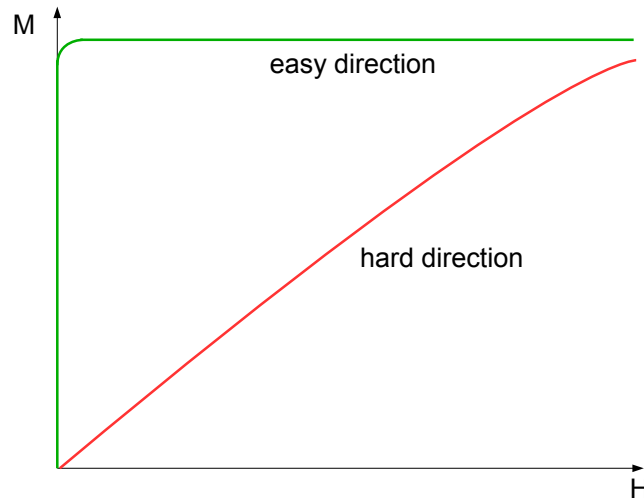


Figure 1.8: Example behaviour of magnetization curves of an anisotropic crystal when field is applied along easy (green) and hard (red) magnetization directions.

The anisotropy is not necessarily uniaxial, although that is a prerequisite for permanent magnetism. It depends on the symmetry of the crystal.

The **anisotropy field** is defined as the field needed to saturate the magnetization of a uniaxial crystal in a hard direction, and is equal to $H_a = 2K_1/(g\mu_B M_s)$ [7].

Anisotropy is often described in the terms of an anisotropic g factor: $g = (g_x, g_y, g_z)$ which is then a tensor with different values along different axes. In most cases polycrystalline samples are investigated and the data are interpreted with an average g defined as $g^2 = (g_x^2 + g_y^2 + g_z^2)/3$ [5].

Anisotropic behaviour was investigated in cases presented in Chapters 3.1 and 3.2, in the latter the anisotropic g factor approach was used to simulate the magnetic structure.

1.3 Magnetic heat capacity

Heat capacity is usually measured under constant pressure and is defined by:

$$C_P = \left(\frac{dQ}{dT} \right)_P,$$

where C_P is heat capacity of the material at a constant pressure, Q is the heat delivered to/emitted from the system and T is temperature.

Entropy is defined as such:

$$S = \int \frac{dQ}{T} = \int \frac{C_P}{T} dT.$$

In magnetic materials, there is a significant contribution to the heat capacity near the ordering temperature. The entropy gain induced by the magnetic ordering near the phase transition is predicted theoretically to be:

$$\Delta S = kN_A \ln(2S + 1) = R \ln(2S + 1)$$

where $R = kN_A$ is the gas constant and S is the spin of the magnetic centers [12]. To extract the magnetic contribution to the heat capacity, the phonon heat capacity has to be subtracted from the total heat capacity and that can be roughly done using the Debye model or the Einstein model of the lattice heat capacity [8]. The peak anomaly in magnetic heat capacity usually reflects the magnetic transition in the materials. If external field is applied, the alignment change of the magnetic moments is no longer so rapid and the change in entropy is stretched over a larger range of temperatures, making the anomaly harder to extract from the phonon background.

Examples of heat capacity measurements for molecular compounds and data analysis can be found in Chapters 3.2 and 3.4.

1.4 Photomagnetism

The photomagnetic effect takes place when a material changes its magnetic properties upon irradiation with light. It is a relatively new subject in molecular magnetism, first demonstrated in Prussian blue analogues [13].

The potential applications of materials featuring reversible modification of magnetic properties upon light irradiation is promising for writing/erasing devices.

There are several possible processes leading to photomagnetic behaviour in molecular crystals [14]:

1. A light-sensitive building block can be used for synthesis of polymetallic substances, which can exhibit MLCT (metal-to-ligand charge transfer).
2. It is also possible to use a metal center as, for example, the iron(II) spin crossover compounds which present the light induced excited spin state trapping (LIESST) at low temperature. Up to now, this group includes only finite homonuclear molecules and it has not yet been shown in polymetallic extended systems [15].
3. A light-sensitive ligand can be used as spacer between the paramagnetic metal centers.
4. The last group is based on a collective property of the bimetallic systems and the emergence of the metal-to-metal charge transfer band (MMCT) in the optical spectrum. This is possible when both metal centers have oxidation state flexibility with close redox potentials. Thus, by light irradiation in this band, an internal photo-redox process may occur involving an electron transfer and a change in both metal spin states.

An example of photomagnetic behaviour related to the last case can be found in Chapter 3.5.

Chapter 2

Experimental methods

2.1 Magnetometry

All the magnetic measurements were performed using a Quantum Design Magnetic Property Measurement System 5XL, which is the most commonly used SQUID magnetometer in the world. In this section, the general idea behind the method will be given along with a description of our system and chosen technical specifications. The additional options like Fiberoptic Sample Holder (FOSH) used for photomagnetic measurements and Horizontal Sample Rotator (HSR) used for angle - dependent measurements will be described in more detail as they were also used while gathering the data for this Thesis.

2.1.1 SQUID magnetometry - the idea

The Josephson tunneling effect

The tunneling effect through an insulating barrier between superconductors was discovered by B. D. Josephson in 1962 [16], for which he was awarded a Nobel Prize in 1973 [17].

A Josephson junction (fig. 2.1) is a thin layer of an insulator between two superconductors. Cooper pairs in a superconductor can tunnel through an insulating barrier. The total current through a Josephson junction depends largely on the phase difference between the superconductors on both sides [8]

$$\delta = \vartheta_1 - \vartheta_2.$$

The phases ϑ_1 and ϑ_2 are arbitrary but fixed, hence δ is also fixed. The Josephson current is then given by

$$J(\delta) = J_0 \sin(\delta).$$

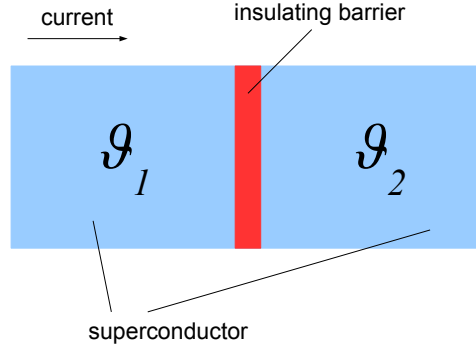


Figure 2.1: A scheme of a Josephson junction.

If there is an electrical time-dependent potential across the Josephson junction, δ will also be time-dependent:

$$\delta(t) = \delta_0 + \frac{1}{\phi_0} \int_0^t V(t') dt',$$

where $\phi_0 = h/2e$ is the flux quantum and $V(t)$ is the difference of potentials on two sides of the junction. If $V(t) = 0$, a current $J(\delta_0)$ can pass the barrier without resistance (DC Josephson effect). If the current surpasses the critical current J_C , the junction will have a measurable resistance.

If $V(t) = V_0 = \text{const}$, the DC current will disappear. The voltage drop will generate an alternating supercurrent at a frequency $\omega = V_0/\phi_0$ (AC Josephson effect).

The Josephson effect was first observed by P. W. Anderson and J. M. Rowell in 1963 [18].

SQUID

The abbreviation SQUID stands for Superconducting QUantum Interference Device. A DC SQUID [8] is a superconducting ring with two Josephson junctions (fig. 2.2)

It uses quantum interference between the two paths that enclose an area with a magnetic flux within the ring. For the two paths through the device the phase difference is:

$$\Delta\vartheta = \delta_{\text{I/II}} + \frac{1}{\phi_0} \int_{\text{I/II}} \vec{A}(\vec{s}) d\vec{s},$$

where I/II indicates which Josephson junction the current is passing and $\vec{A}(\vec{s})$ is the vector potential along a path \vec{s} .

The gauge invariance demands that the total phase difference is zero or $n \cdot 2\pi$.

The induced flux in the ring by the external field is $\phi_{\text{ext}} = \oint \vec{A}(\vec{s}) d\vec{s}$. The critical current through the DC SQUID is then given by:

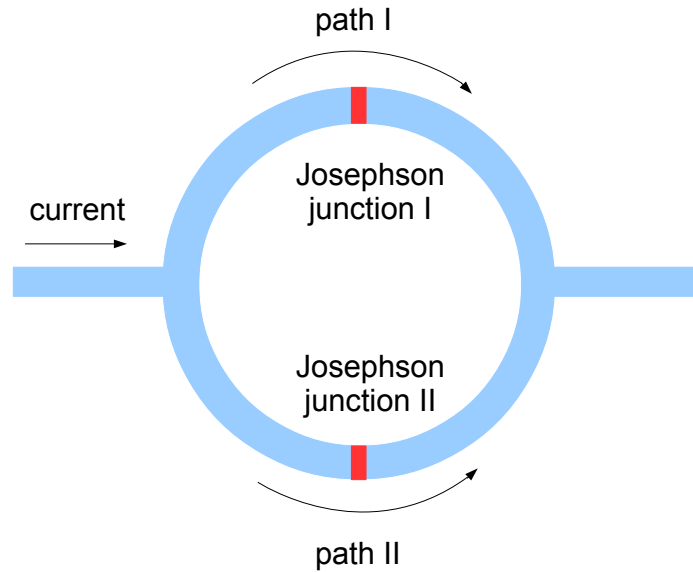


Figure 2.2: A scheme of a DC SQUID.

$$I_C = I_0 \left| \cos \frac{\pi \phi_{ext}}{\phi_0} \right|.$$

The critical current is modulated by the magnetic flux flowing through the ring. I_C is maximum when ϕ_{ext} satisfies the quantization condition (is an integer multiple of ϕ_0). This allows a measurement of magnetic flux with great precision.

The first SQUID was constructed by R. Jaklevic, J. Lambe, A. Silver and J. Mercerau in 1964 [19].

Modern SQUID magnetometers

A simple idea of the construction of a SQUID magnetometer [8] is presented in fig. 2.3.

The sample travels through the detection coil which is connected to the input coil. It communicates with the SQUID ring by means of mutual inductance. The output of the SQUID is proportional to the critical current in the SQUID which is a periodic function of the flux. There is a second feedback coil which also communicates with the SQUID by their mutual inductance. The feedback system allows calculating the flux that passed through the SQUID ring and thus measuring the sample magnetization.

Modern SQUID magnetometers are equipped with superconducting magnets and precise temperature control systems which allow measurements in a large range of fields and ultra-low temperatures.

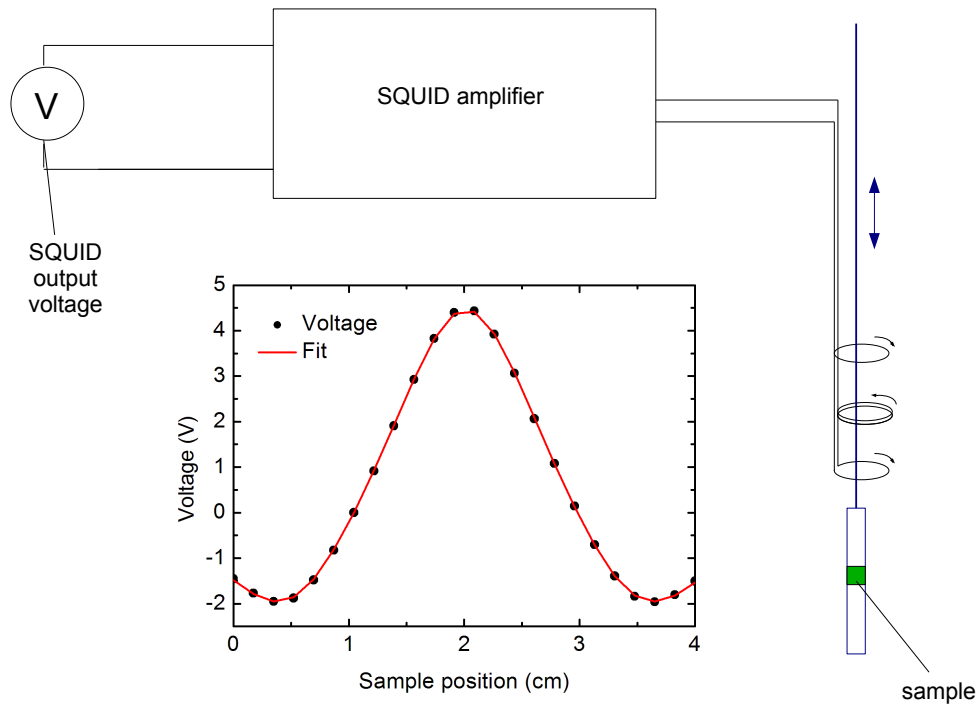


Figure 2.3: A scheme of a SQUID magnetometer

2.1.2 Quantum Design MPMS XL system

The system used in our laboratory is a Quantum Design MPMS 5XL. In addition to the classic DC and AC measurements, a more sensitive Reciprocating Sample Option is installed, improving the sensitivity to 10^{-8} emu. The system is equipped with a superconducting magnet and a precise temperature control system, allowing measurements in the temperature range 1.8 - 300 K and in fields 0 - 50 kOe.

DC measurements

In a basic DC measurement, the magnetic moment of the sample is measured by reading the output of the SQUID detector while the sample moves upward, from the initial position, through the SQUID pickup coils. This upward movement completes one vertical scan. Voltage readings that are taken as a function of the sample's position in the coils comprise the raw measurement data. At each position in the coils, the software typically reads the SQUID output voltage several times, and multiple scans are averaged together to improve the resolution [20]. These measurements have the typical accuracy of 0.1%.

The Reciprocating Sample Option measures the magnetic moment of the sample in an alternative way. Instead of moving the sample steadily through the SQUID pickup coils, like in the case of the basic DC measurement, and stopping the motor for each data reading, it moves the sample rapidly and sinusoidally through the coils. Lock-in techniques that use digital signal processor reduce the contribution of low-frequency noise to the measurement. RSO measurements have a sensitivity of approximately $5 \cdot 10^{-9}$ emu [21].

Most of the measurements of static magnetic susceptibility for this Thesis were done using this option, except for the signals of range larger than 10^{-1} emu, in case of which classic DC measurements were performed.

AC measurements

In AC magnetic measurements, a small AC drive magnetic field is applied to the sample, in addition to the DC field, causing a time-dependent moment in the sample. The field of the time-dependent moment induces a current in the pickup coils, allowing measurement without sample motion. The AC susceptibility (differential susceptibility) $\chi_{AC} = dM/dH$ obtained from these measurements has both real and imaginary components, χ' and χ'' :

$$\chi = \chi' + i\chi''.$$

Since the AC measurement is sensitive to the slope of $M(H)$ and not to the absolute value, small magnetic shifts can be detected even when the absolute moment is large.

In the limit of low frequency where AC measurement is most similar to a DC measurement, the real component χ' is just the slope of the $M(H)$ curve. The imaginary component, χ'' , indicates dissipative processes in the sample.

In conductive samples, the dissipation is due to eddy currents. Relaxation and irreversibility in spin-glasses give rise to a nonzero χ'' . In ferromagnets, a nonzero imaginary susceptibility can indicate irreversible domain wall movement. Also, both χ' and χ'' are very sensitive to thermodynamic phase changes, and are often used to measure transition temperatures [22], [23].

2.1.3 Horizontal Sample Rotator

The Horizontal Sample Rotator (HSR) allows samples to rotate around a horizontal axis. Samples are mounted on a small plate (rotor), which enables sample rotations of up to 360 degrees [24]. The photos of the HSR are shown in Fig. 2.4.

The sample is glued onto the rotor, which is a small frame caused to rotate by the movement of a thin copper wire, wound around the rotor pulley, one end fixed to the rotator motor placed on the top of the inset, the other end fixed to a spring. The rotation angle, related to the turns of the rotator motor, is set by

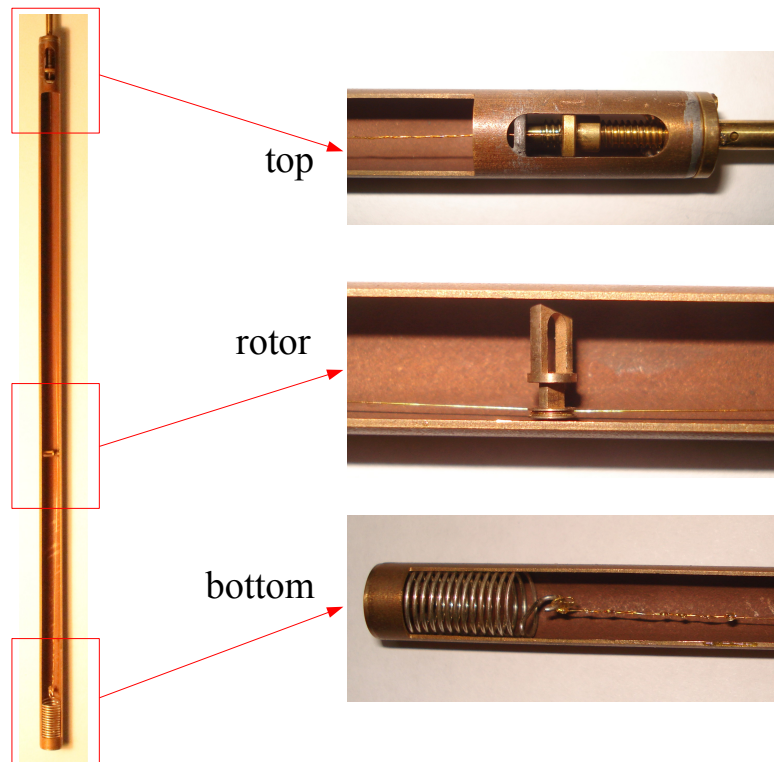


Figure 2.4: Photos of the Horizontal Sample Rotator for MPMS.

the MPMS software. As there are about three degrees of backlash in the rotator mechanism, the rotational position always ought to be approached from the same direction.

Tests were performed for the contribution to the magnetic signal of the Horizontal Rotator, results shown in fig. 2.5.

As can be seen, the signal from the HSR is very small (of order 10^{-6} emu). The zero-field measurements were done to check for the ferromagnetic contamination of the sample rotor. The measurement in 100 Oe allows estimating the diamagnetic signal from HSR. The signal is diamagnetic and temperature independent. Assuming that the signal is linear with field (Chapter 1.2.2), even in measurements in 10 kOe the range of the signal can rise up to 10^{-4} emu, which is still usually negligible compared to the magnetic moment of the samples measured.

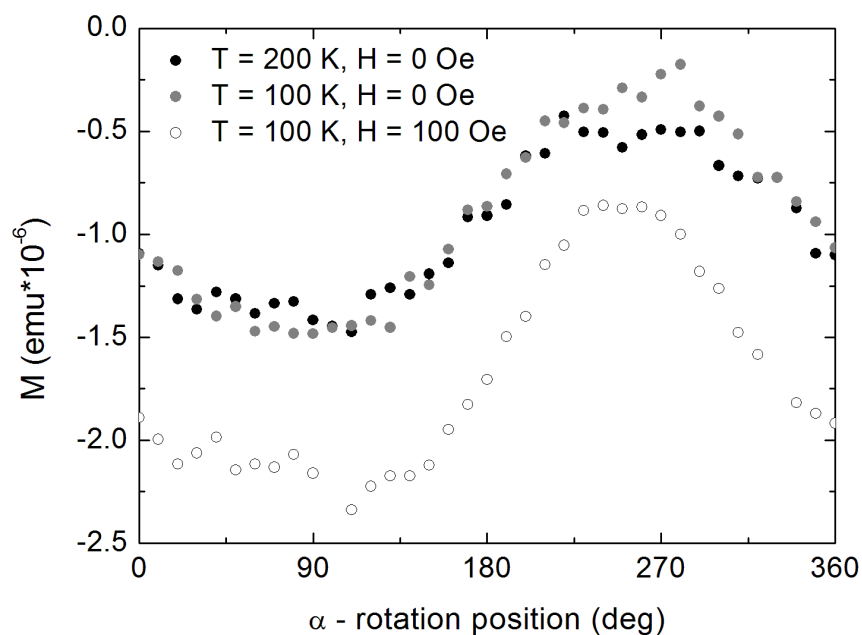


Figure 2.5: The magnetic signal from the Horizontal Sample Rotator versus rotation angle in chosen temperatures and fields.

2.1.4 Fiberoptic Sample Holder

The Fiberoptic Sample Holder (FOSH) is a sample illumination system for MPMS for photomagnetic measurements, where light is delivered to the sample through a quartz fiber optic rod that runs down the center of the metal sample support rod and extends down into a special sample holder. The top of the fiber optic rod is connected to a flexible fiber optic bundle, which can be used to connect the FOSH to a separate light source. A schematic drawing of FOSH is presented in fig. 2.6.

The heart of the sample holder is a spring-loaded slide assembly constructed of nested quartz tubes. It is enclosed by an outer quartz guide tube, mounted to the bottom of a sample rod. The sample itself is contained in a small quartz cup, held in place by a set of two short inner quartz tubes. The light travels through a flexible optic bundle to a fiber optic quartz rod 1.5 mm in diameter and then to the sample. A piece of the same quartz rod is added at the bottom to symmetrize the magnetic signal. A gentle upwards pressure is maintained by a beryllium copper spring mounted in a treaded cap on the bottom end of the guide tube.

The total geometrical light transmittance of the FOSH fiber optic rod is calculated by the producer to be 61%. Measurements performed at $\lambda = 532$ nm

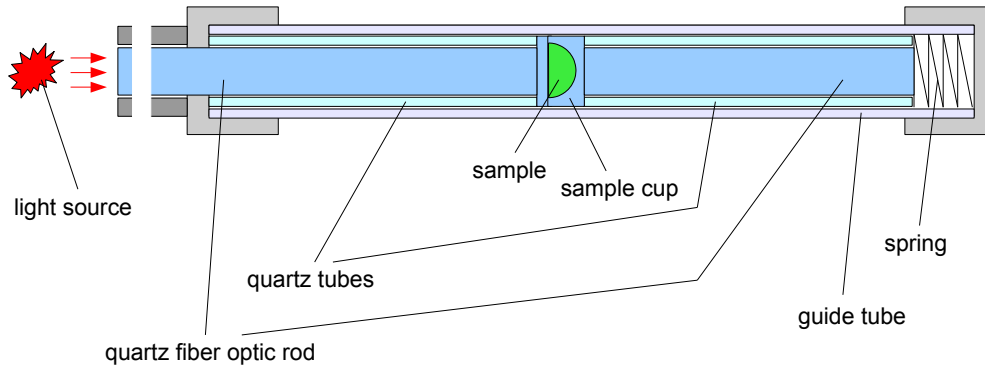


Figure 2.6: A scheme of the Fiberoptic Sample Holder (FOSH).

using a Thorlabs Digital Optical Power and Energy Meter provided the value of around 50% (light power measured at the source and at the end of the fiberoptic rod placed directly above the sample).

The diamagnetic contribution to the signal from the holder of approximately 10^{-3} emu at 50 kOe is reported by the producer [25].

The light sources used with the FOSH in our laboratory are a green 532 nm laser and a diode laser assembly with exchangeable diodes (405, 407, 450, 660 and 850 nm). The FOSH was tested for the maximum power available to use in different temperatures without losing the thermal stability in MPMS (the light power was measured at the exit of the light source before entering the fiberoptic bundle): in 5K the maximum power was 7 mW, in 10 K 30 mW, in higher temperatures no significant limit for the light source power was observed.

2.2 Heat capacity measurements

The heat capacity measurements were done using a Quantum Design Physical Property Measurement System Heat Capacity Option. In this section a brief overview of the method and the most important specifications of our system will be given.

2.2.1 Heat capacity measurements - the idea

The heat capacity depends on many variables, including temperature, pressure, volume and magnetic field. Most commonly, the heat capacity is measured at a constant pressure (as it is done in the PPMS):

$$C_p = \left(\frac{dQ}{dT} \right)_p.$$

In all the heat capacity measurement techniques, the amount of heat added to or removed from the sample is monitored while measuring the changes in temperature.

2.2.2 Quantum Design PPMS

The Quantum Design PPMS is equipped with a temperature control system and superconducting magnets, and allows measurements of heat capacity in the temperature range of 1.9 - 400 K and in fields up to 90 kOe. The minimal pressures reached in the system are approximately 0.01 mTorr, ensuring elimination of any alternate thermal links through residual gas.

The sample installment scheme in the PPMS Heat Capacity Option is presented in fig. 2.7. The sample is placed with a small amount of Apiezon grease (ensuring good thermal contact) on a metal platform, isolated from the thermal bath (which allows precise control of the heat transferred to the sample), but connected through metal wires to the sample puck, which itself is immersed in the thermal bath. A platform heater and a platform thermometer are attached to the bottom side of the platform. Small wires provide the electrical connection to the platform heater and platform thermometer, and at the same time provide the thermal connection to the puck frame and a structural support.

During the measurement, a known amount of heat is applied to the platform with the sample at a constant power for a fixed time, and then this heating period is followed by a cooling period of the same duration. After each measurement cycle the software fits the entire temperature response of the sample platform to a model that accounts for both the thermal relaxation of the sample platform to the bath temperature and the relaxation between the sample platform and the sample itself. The fitting technique assumes that the heat capacity is approximately constant over the range of temperatures covered by a single measurement cycle.

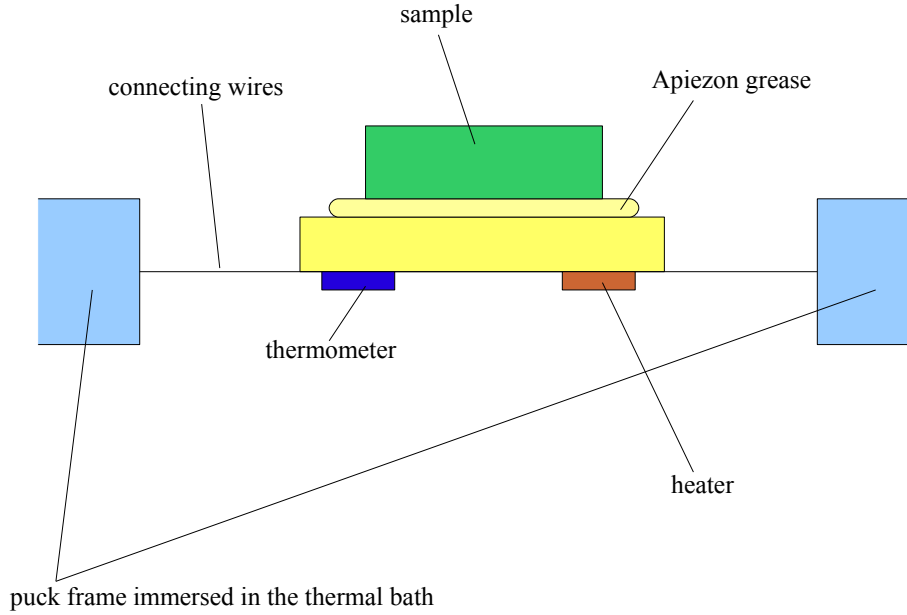


Figure 2.7: A scheme of a sample holder for heat capacity measurements in the PPMS system.

There are two fitting models used by the PPMS software describing the temperature response of the sample platform as a function of time used in the measurements.

The simple model assumes that the sample and the sample platform are in good thermal contact and are at the same temperature during the measurement. In this model, the temperature T of the platform as a function of time t obeys the equation:

$$C_{total} \frac{dT}{dt} = P(t) - K_W(T(t) - T_b),$$

where C_{total} is the total heat capacity of the sample and the sample platform, K_W is the thermal conductance of the supporting wires, T_b is the temperature of the thermal bath and $P(t)$ is the power applied by the heater ($= P_0$ during the heating period and $= 0$ during the cooling period). The solutions of this equation are exponential functions with a characteristic time constant $\tau = C_{total}/K_W$.

The two tau model is used when the thermal attachment of the sample to the platform is poor, and simulates the effect of the heat flowing between the sample platform and sample and the effect of heat flowing between the sample

platform and the puck. It obeys the equations:

$$C_p \frac{dT_p}{dt} = P(t) - K_W(T_p(t) - T_b) + K_g(T_s(t) - T_p(t)) \text{ and}$$

$$C_s \frac{dT_s}{dt} = -K_g(T_s(t) - T_p(t)),$$

where C_p is the heat capacity of the sample platform, C_s is the heat capacity of the sample and K_g is the thermal conductance between the two due to grease. $T_p(t)$ and $T_s(t)$ are the platform and the sample temperatures, respectively. In this case, the solutions are exponents with two characteristic time constants, $\tau_1 = 1/(\alpha - \beta)$ and $\tau_2 = 1/(\alpha + \beta)$, where:

$$\alpha = \frac{K_W}{2C_p} + \frac{K_g}{2C_p} + \frac{K_g}{2C_s},$$

$$\beta = \frac{\sqrt{K_g^2 C_s^2 + 2K_g^2 C_s C_p + K_g^2 C_p^2 + K_W^2 C_s^2 + 2K_W C_s^2 K_g - 2K_W C_s K_g C_p}}{2C_p C_s}.$$

Prior to the measurement of the sample, an addenda measurement (heat capacity of the platform with a small amount of Apiezon grease) is performed, using only the simple model. Next, a sample is placed on top of the grease and measured, this time fits performed according to both the fitting models. The heat capacity numbers derived from the two-tau model (assuming $C_p = C_{addenda}$ from the previous measurement) are used only if the fit deviation is smaller than in the case of the simple model [26].

Chapter 3

Results and analysis

3.1 A new chiral molecular magnet: 3D cyano-bridged $\text{Mn}_2^{\text{II}} - \text{Nb}^{\text{IV}}$

3.1.1 Structure

Chiral $[\text{Mn}^{\text{II}}(\text{urea})_2(\text{H}_2\text{O})]_2[\text{Nb}^{\text{IV}}(\text{CN})_8]_n$, where urea = $\text{CO}(\text{NH}_2)_2$ (from now on the compound is called $\text{Mn}_2^{\text{II}} - \text{Nb}^{\text{IV}}$ for simplicity) exhibits a 3-D coordination framework based on cyanide bridges linking Mn^{II} and Nb^{IV} centers.

The structure of the unit cell of $\text{Mn}_2^{\text{II}} - \text{Nb}^{\text{IV}}$ is tetragonal ($P4_1$ space group), with parameters $a \equiv b = 10.450(5)$ Å, $c = 22.736(5)$ Å, angles $\alpha = \beta = \gamma = 90.000(5)^\circ$.

Its 3-D coordination skeleton can be described as comprising two sets of infinite waved ladder-motifs running along a and b direction, respectively, and cross-linking at Nb^{IV} centers (Figure 3.1 a)). While Nb atoms link both ladders' sets together, giving raise to the 3D coordination network, Mn atoms belong exclusively to one of the sets. Coordination sphere of Nb^{IV} centers (Figure 3.1 b)) is dodecahedral and is composed of eight carbon atoms of eight CN- ligands. Six cyanido ligands act as molecular bridges forming $\text{Nb}^{\text{IV}}\text{-CN-Mn}^{\text{II}}$ linkages and the remaining two are terminal ones. Both Mn1 and Mn2 exhibit distorted octahedral geometry (fig. 3.2). The presence of six and three bridging cyanides per Nb^{IV} and Mn_2^{II} , respectively, causes each Mn atom to be connected to 3 neighbouring Nb ions and each Nb ion connects to 6 Mn neighbours through CN bridges (Figures 3.2 and 3.3) [27].

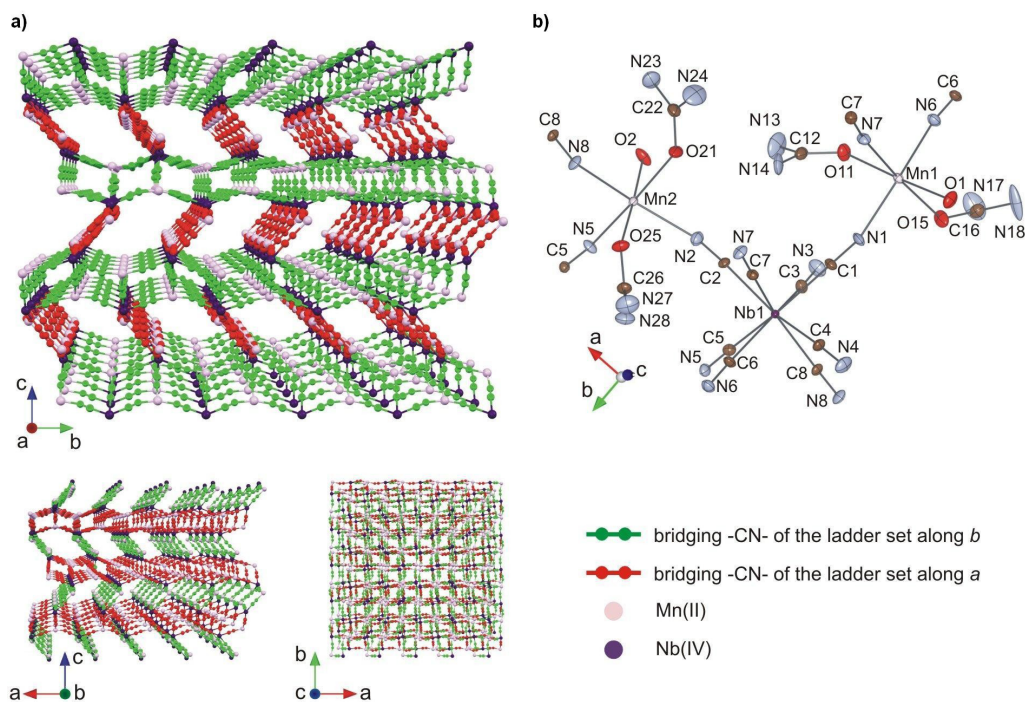


Figure 3.1: a) packing diagrams of $\text{Mn}^{\text{II}}-\text{Nb}^{\text{IV}}$ showing herringbone-like arrangement (urea, terminal cyanides and aqualigands omitted for clarity), b) "local" fragments of the structure.

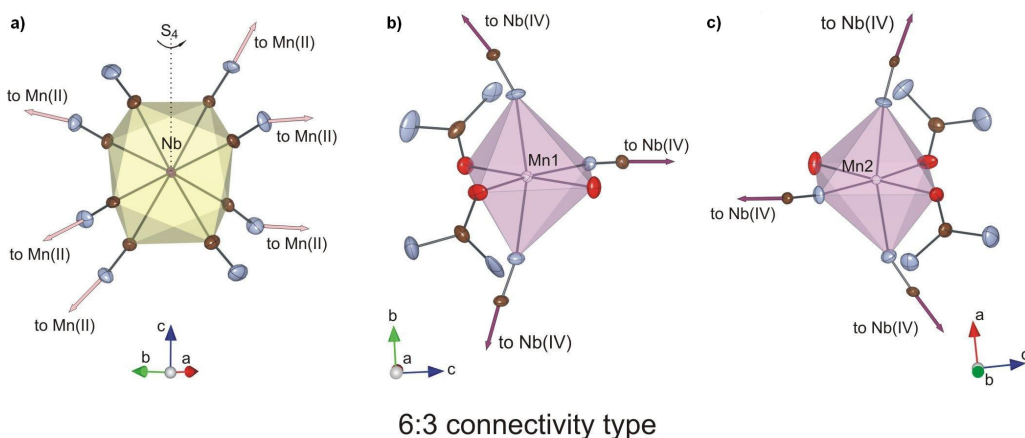


Figure 3.2: Fragments of structure of $\text{Mn}^{\text{II}}-\text{Nb}^{\text{IV}}$ showing coordination spheres of a) Nb, b) Mn1 and c) Mn2 and the 6:3 connectivity type with the presence of six and three bridging cyanides per Nb^{IV} and Mn^{II} , respectively

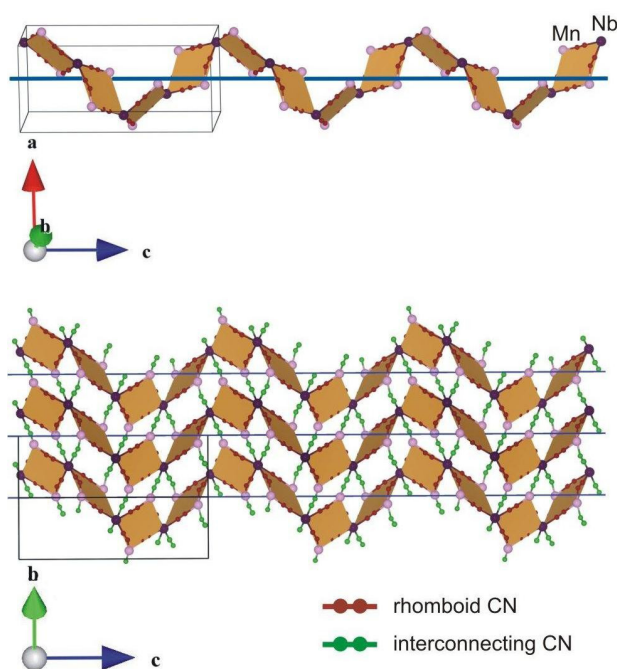


Figure 3.3: Fragments of structure of $Mn^{II} - Nb^{IV}$ showing the chirality of the compound along the *c* axis, viewed along *b* and *a* crystallographic axes.

3.1.2 Experimental

The samples were obtained by dr D. Pinkowicz. For magnetic measurements both powder and single crystal samples were used.

The powder sample's mass weighed on the laboratory scale was 20.8 mg. For the measurement it was pressed into a gelatine capsule, which is widely used for magnetic measurements. The magnetic properties of the capsule were investigated separately prior to the sample measurements and the results are presented in fig. 3.4 and 3.5. As can be seen in these graphs, in 10 kOe the signal is in the range of 10^{-4} emu and for the temperature dependence measurement in 1 kOe it is one order of magnitude lower. Thus, the diamagnetic contribution from the capsule to the magnetic signal can be usually neglected compared to the signal of the samples measured, in other cases, for example at high temperatures, the data can be corrected for the contribution from the capsule.

The single crystal sample's (Fig. 3.6) mass weighed on laboratory scale was 1.2 mg. Due to the lack of a more accurate scale, the mass had to be corrected with respect to the magnetic results of a much larger powder sample. Calculated according to the saturation magnetization value at low temperature, the single crystal's mass was found equal to 1.31 mg.

The crystallographic axes were determined and, with respect to those, the magnetic measurements along axes *a* ($\equiv b$) and *c* were performed. Fig. 3.7 shows

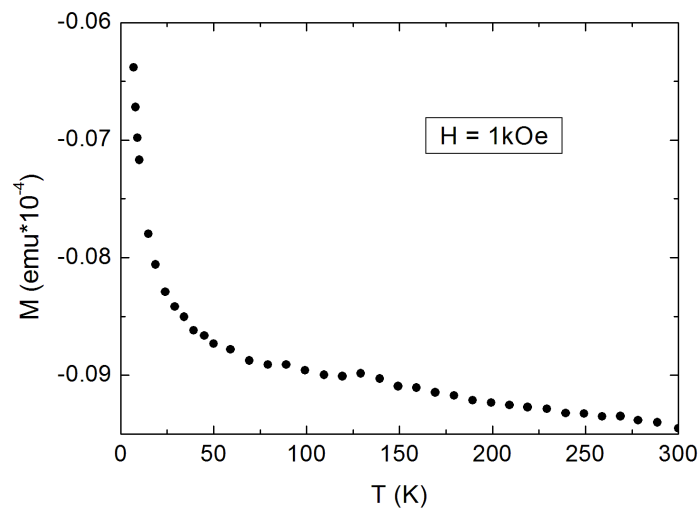


Figure 3.4: Temperature dependence of the magnetic contribution of a gelatine capsule used as a holder for the powder measurements. Measurement was taken at 1 kOe.

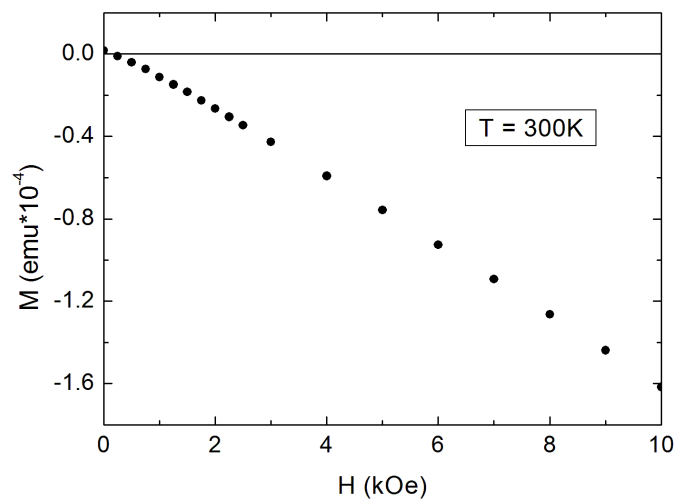


Figure 3.5: Field dependence of the magnetic contribution of a gelatine capsule used as a holder for the powder measurements. Measurement was taken at 300 K.

the method of placing the single crystal sample in the holder in case of both the measurements ($\vec{a} \parallel \vec{H}$ and $\vec{c} \parallel \vec{H}$ on left and right, respectively). The sample was glued with Varnish GE 7031 onto a square 5x5 mm piece of PE sheet and then glued inside the MPMS straw holder.



Figure 3.6: Photography of the top-cut pyramidal-shaped single crystal sample of $Mn_2^{II} - Nb^{IV}$ used for magnetic measurements. The size of the grid on which the crystal was photographed is 1mm.

The properties of Varnish GE 7031 are widely known to be ideal for magnetic measurements (the contribution to the magnetic signal is negligible). The glue was also tested not to dissolve the sample.

The PE sheet used as the holder for the crystal was tested for magnetic properties. A measurement for a piece of the PE sheet several times larger than the piece used as a holder for the single crystal sample was done at 300 K with respect to the field to check the contribution to the magnetic signal. The results are presented in the figure 3.8. As can be seen from the measurement, the range of the signal is approximately 10^{-4} emu which, compared to the signal even from the small crystal sample, is negligible.

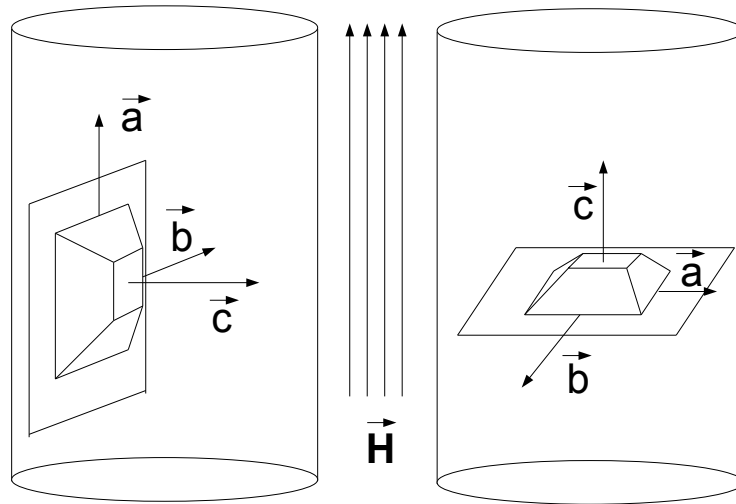


Figure 3.7: Method of placing the single crystal sample in the holder for MPMS measurements.

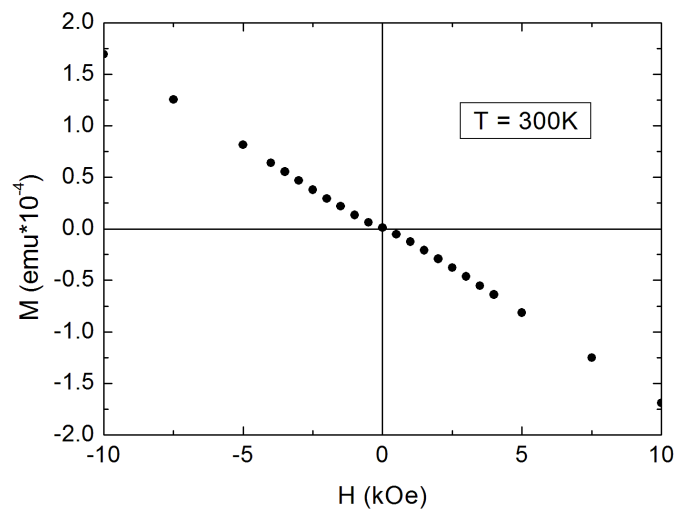


Figure 3.8: Magnetic signal in 300 K in emu versus field measured for a large piece of plastic used as a holder for the single crystal sample.

3.1.3 Magnetic studies of $Mn_2^{II} - Nb^{IV}$

Powder sample magnetic studies

From the structural characterization it is known that a formula unit of $Mn_2^{II} - Nb^{IV}$ contains two Mn_2^{II} of spin 5/2 and one Nb^{IV} of spin 1/2. The g-factors for both the magnetic centres are expected to be close to 2.00. They create a three dimensional magnetic lattice – each Nb^{IV} magnetic moment interacts with six Mn_2^{II} ions and each magnetic moment of Mn_2^{II} interacts with three Nb^{IV} ions through -CN- bridges.

Magnetic susceptibility vs. temperature at $H = 1$ kOe was measured. The data were carefully corrected for the diamagnetic contribution of the gelatine capsule (Fig. 3.4) and inverse magnetic susceptibility versus temperature curve was obtained which is presented in Fig. 3.9.

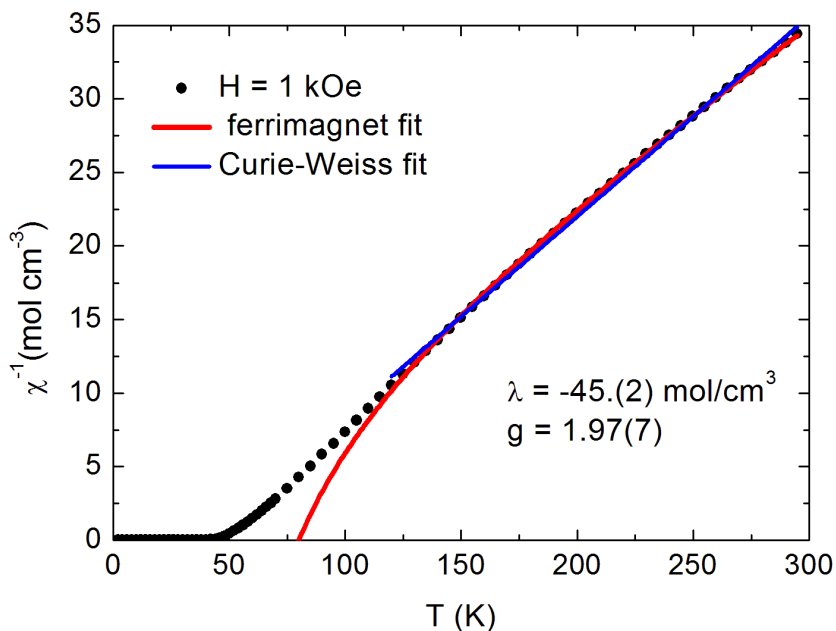


Figure 3.9: Inverse magnetic susceptibility of a powder sample of $Mn_2^{II} - Nb^{IV}$ measured at $H = 1$ kOe. The blue line represents a Curie-Weiss fit to the data above 120 K. The red line is a fit of a simple ferrimagnet model above 120 K (see text). The mass of the sample used was 20.8 mg.

Even after the correction for the diamagnetic contribution the data still deviates from the Curie-Weiss law (blue line in Fig. 3.9). The formula for the susceptibility of a simple ferrimagnet above T_C (equation (1.14) from Chapter 1.2.4) was used. It was assumed that the only interactions possible are those between

Mn and Nb (neglecting the interactions between the atoms of the same type). The formula for the inverse susceptibility for this compound is:

$$\frac{1}{\chi} = \frac{T^2 - 2\lambda^2 C_{5/2} C_{1/2}}{(2C_{5/2} + C_{1/2})T + 4\lambda C_{5/2} C_{1/2}}, \quad (3.1)$$

where C_S denotes the Curie constants for respective spins (5/2 for Mn, 1/2 for Nb) and $\lambda = 6J_{\text{Mn-Nb}}/(N_A g^2 \mu_B^2)$ is the molecular field constant. This model was found to agree with the data much better than the Curie-Weiss law. From the fit, the values of $g = 1.97(7)$ and $\lambda = -45.(2) \text{ mol/cm}^3$ were obtained. The g value is close to the expected 2.00. The negative value of λ indicates that the predominant interaction between Mn and Nb is antiferromagnetic.

Next, the zero-field cooling/field cooling dependence was measured at 10 Oe, which is presented in Fig. 3.10.

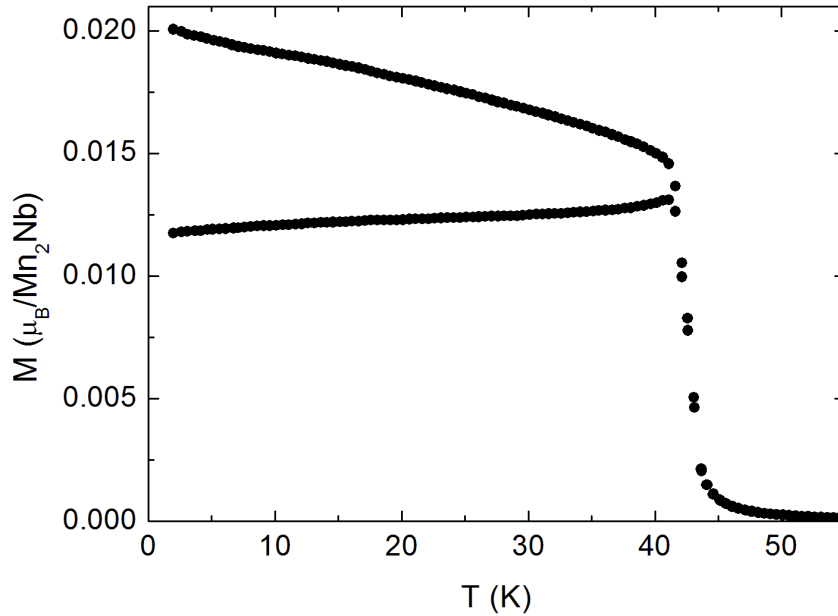


Figure 3.10: Zero-field cooling/field cooling curves of a powder sample of $\text{Mn}_2^{\text{II}} - \text{Nb}^{\text{IV}}$ measured at around 10 Oe.

The transition temperature is equal to $T_C = 42.6(4) \text{ K}$ (defined as the position of the maximum of $M(T)$ slope). The sharp increase in the magnetization below T_C is the onset of a ferromagnetic transition.

The AC measurement of the powder sample is presented in Fig. 3.11.

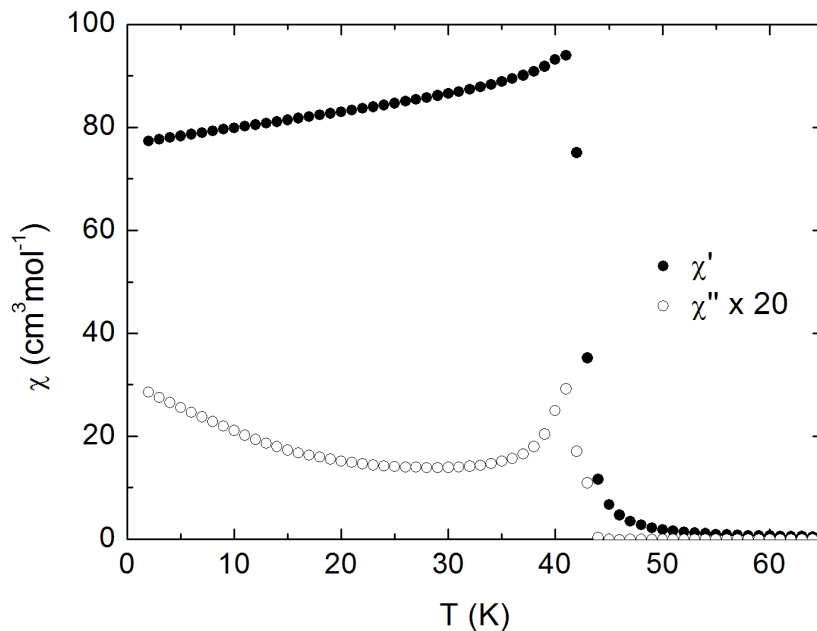


Figure 3.11: AC measurement of a powder sample of $Mn_2^{II} - Nb^{IV}$ measured at $H_{AC} = 3$ Oe.

The χ'' signal, multiplied by a factor of 20 for better visibility, is negligible. The peak in the susceptibility is approximately at 43 K.

Magnetization versus field dependence was measured, which is presented in Fig. 3.12.

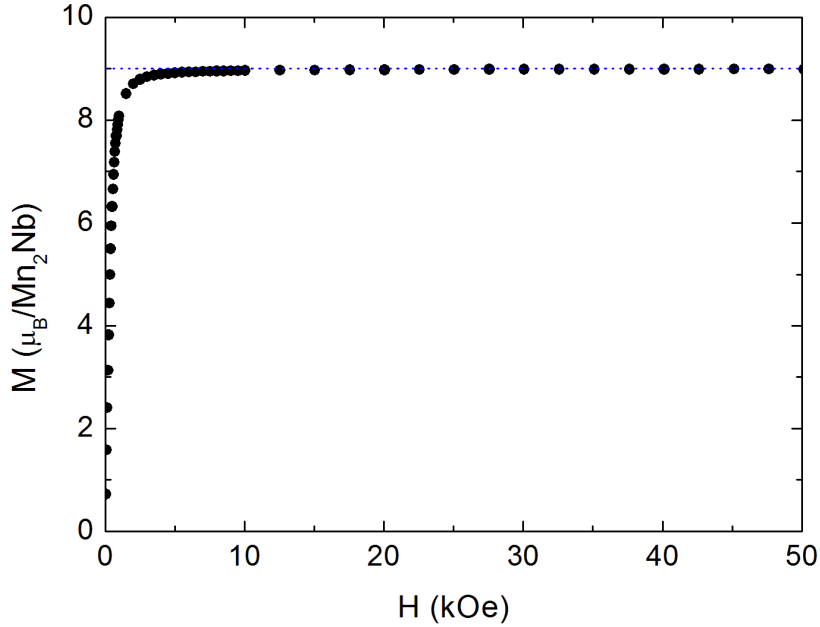


Figure 3.12: Magnetization field dependence of a powder sample of $\text{Mn}_2^{\text{II}} - \text{Nb}^{\text{IV}}$ measured at 2 K. The dashed line represents the level $M = 9\mu_B$.

The magnetization quickly saturates at the value $9\mu_B$ which suggests anti-ferromagnetic coupling of Mn^{II} and Nb^{IV} (two spins of $5/2$ against one spin of $1/2$). This is consistent with the measurement of susceptibility versus temperature (fig. 3.9). The perfectly constant $M(H)$ up to 50 kOe at 2 K agrees with the fact that the Nb spin-flip transition, simulated in the mean field model, takes place above 1200 kOe [27]. The sample shows no magnetic hysteresis.

Single crystal magnetic studies

As the single crystal sample used was very small and more prone to influence of contamination, prior to the measurements a test in 300 K was performed to check for ferromagnetic contaminants. The results are shown in fig. 3.13.

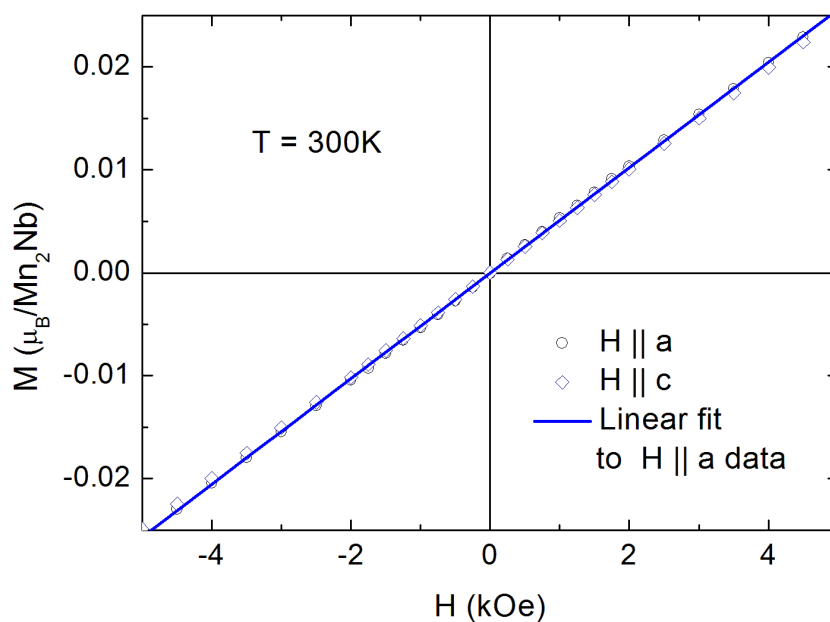


Figure 3.13: Magnetization field dependence of the single crystal sample of $Mn_2^{II} - Nb^{IV}$ measured at room temperature for field parallel to a and c crystallographic directions to test for ferromagnetic contamination. The straight line represents a linear fit to the data.

No measurable contamination was observed (no deviations from the straight line in fig. 3.13) which proves that the sample is uncontaminated and paramagnetic in 300 K, as presumed.

Next, a measurement of magnetization versus field parallel to directions a and c at low temperatures was done to determine if any magnetic anisotropy is present in the material. The measurement was taken at two temperatures: 2 and 30 K, of which results are shown in fig. 3.14.

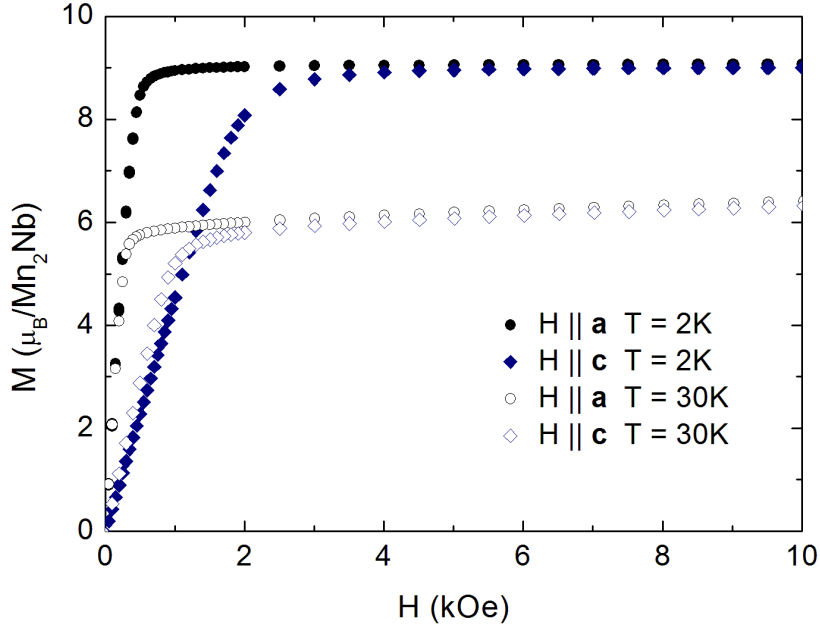


Figure 3.14: Magnetization field dependence of a single crystal sample of $\text{Mn}_2^{\text{II}} - \text{Nb}^{\text{IV}}$ measured at 2 and 30 K, for field parallel to a and c crystallographic directions.

It is clear that the sample is anisotropic and that the a crystallographic axis is the easy magnetization axis and c is the hard magnetization axis which is seen in both 2 K and 30 K.

To calculate the anisotropy field, the data had to be corrected for demagnetization (see Appendices). The data for $H \parallel a$ were corrected in such a way that the magnetization reaches saturation value instantly, from which the demagnetization factor along a $N_a = 1.05\pi$ was found. As $a \equiv b$, $N_a = N_b$, and from the condition $N_a + N_b + N_c = 4\pi$, $N_c = 1.9\pi$ was derived.

The anisotropy field (following the definition from Chapter 1.2.5 as the field needed to saturate the magnetization in the hard direction, in our case c) was calculated as $H_a = 1.2$ kOe, which is considered small.

The zero-field cooling/field cooling measurement along the crystallographic axes confirms what was learned from the magnetization curves about c being the hard magnetization axis. The results are presented in fig. 3.15.

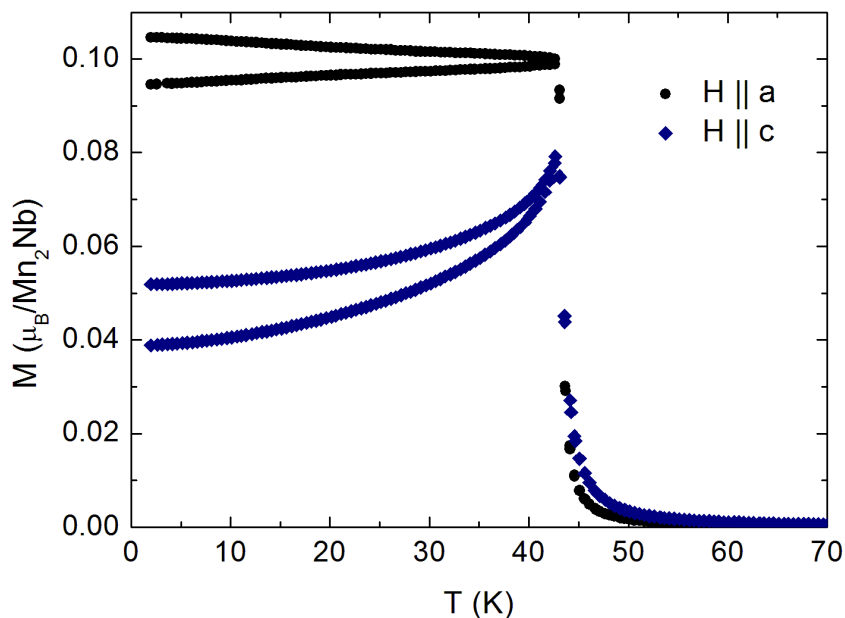


Figure 3.15: Zero-field cooling/field cooling magnetization versus temperature curves measured for a single crystal sample of $Mn_2^{II} - Nb^{IV}$ for field parallel to a and c crystallographic directions. $H = 10$ Oe.

Like in the powder sample, the single crystal shows a rise of spontaneous magnetization below T_C , which is considerably smaller in the case of $H \parallel c$. The irreversibility is consistent with existing ferromagnetic component, but it is small due to the lack of single ion anisotropy for Mn_2^{II} and Nb^{IV} . The signal below 43 K for $H \parallel a$ is cut by the demagnetization field.

Next, an AC measurement of magnetization versus temperature was taken with $H_{ac} = 3$ Oe parallel to both the axes investigated, data shown in fig. 3.16.

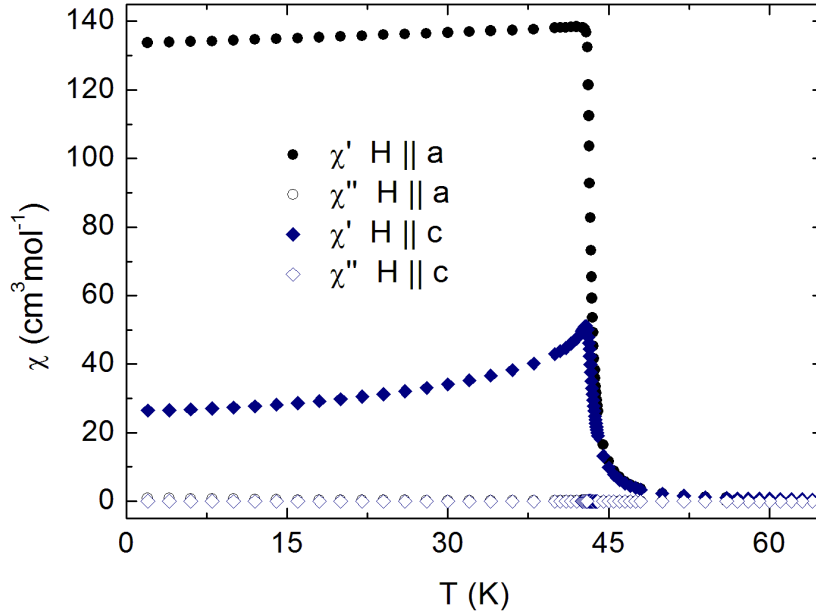


Figure 3.16: AC susceptibility versus temperature of a single crystal sample of $\text{Mn}_2^{\text{II}} - \text{Nb}^{\text{IV}}$ for field $H_{AC} = 3$ Oe parallel to a and c crystallographic directions. $f_{AC} = 10$ Hz.

Once again, the ordering of the magnetic moments proves harder along the c crystallographic axis, confirming what was derived from previous measurements. Also, the data from the powder measurement agree with the single crystal one - the AC curve for powder is an average of susceptibility along all crystallographic directions ($\chi_{\text{powder}} = \frac{1}{3}(\chi_a + \chi_b + \chi_c)$). In this case as well, like in the powder, the out-of-phase susceptibility is negligible, proving non-existence of any time-dependent relaxation processes.

Lastly, a measurement of magnetization was done at various fields along a and c axes. The results are presented in fig. 3.17.

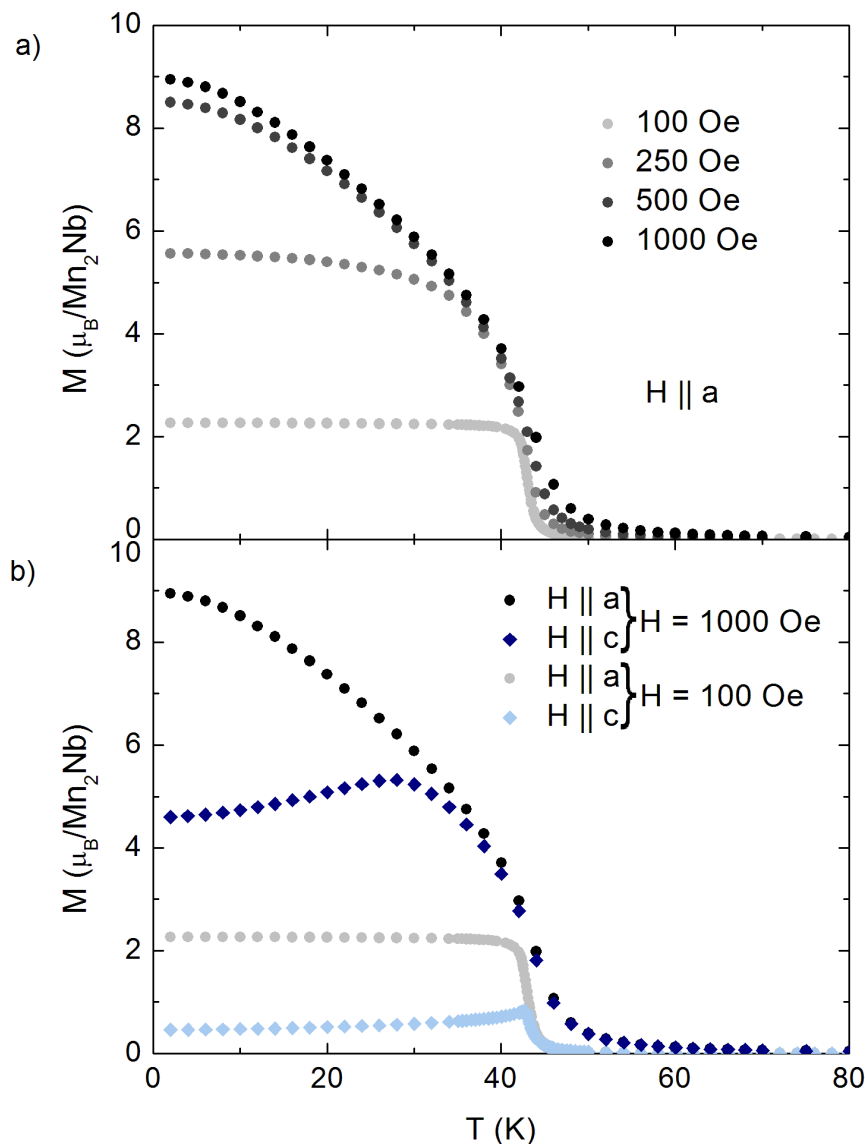


Figure 3.17: Magnetization versus temperature for a single crystal sample of $Mn^{II} - Nb^{IV}$, a) in four different external fields applied along a axis, b) in fields 100 Oe and 1000 Oe applied along a and c axes.

For all the applied fields, below T_C the magnetization rapidly increases, for 1000 Oe along a direction forming a single domain ($M = 9\mu_B$ at low temperatures). In smaller fields (fig. 3.17 a)), however, the signal is cut by the multi-domain effects

and demagnetization. Fig. 3.17 b) shows the difference between the magnetization versus temperature for the field applied along a and c axes.

3.1.4 Summary

Magnetic properties of $\text{Mn}_2^{\text{II}} - \text{Nb}^{\text{IV}}$ both in powder and single crystal form were investigated. All of the data point to $\text{Mn}_2^{\text{II}} - \text{Nb}^{\text{IV}}$ being a soft 3D ferrimagnet with critical temperature $T_C = 42.6(4)$ K. The ferrimagnetic nature of the compound was in particular confirmed by fitting a simplified molecular field ferrimagnet model to the reciprocal susceptibility versus temperature data and by the magnetization value in the ordered state. Small anisotropy was discovered during single crystal measurements, c crystallographic axis being the hard magnetization axis, whereas $a \equiv b$ being the easy axes. The lack of magnetic hysteresis, negligible χ'' , and only a small difference between ZFC and FC magnetization curves correspond with small anisotropy constant. Such behaviour is expected due to the lack of orbital moment for both Mn_2^{II} and Nb^{IV} ions.

The compound was further investigated by Tomohiro Nuida and Shin-ichi Ohkoshi from the University of Tokyo for non-linear optical functionality due to its noncentrosymmetric structure. Magnetization-induced second harmonic generation (MSHG) was observed by them with the largest MSHG/SGH signal ratio among molecule-based noncentrosymmetric magnets, which makes the compound significant in the field of magneto-optics and magnetic materials.

The MSHG data together with the magnetic characterization contained in this Chapter were published in reference [27].

3.2 Magnetic anisotropy of $\text{Co}_3^{\text{II}} - \text{W}_2^{\text{V}}$ ferromagnet

3.2.1 Structure

The crystal structure of $\text{Co}_3^{\text{II}}(2,2'\text{-bpdo})_4(\text{H}_2\text{O})_4[\text{W}^{\text{V}}(\text{CN})_8]_2 \cdot 8\text{H}_2\text{O}$, where bpdo = 4, 4'-bipyridyl-*N,N'*-dioxide (from now on the compound is called $\text{Co}_3^{\text{II}} - \text{W}_2^{\text{V}}$ for clarity) is presented in 3.18 and fig. 3.19.

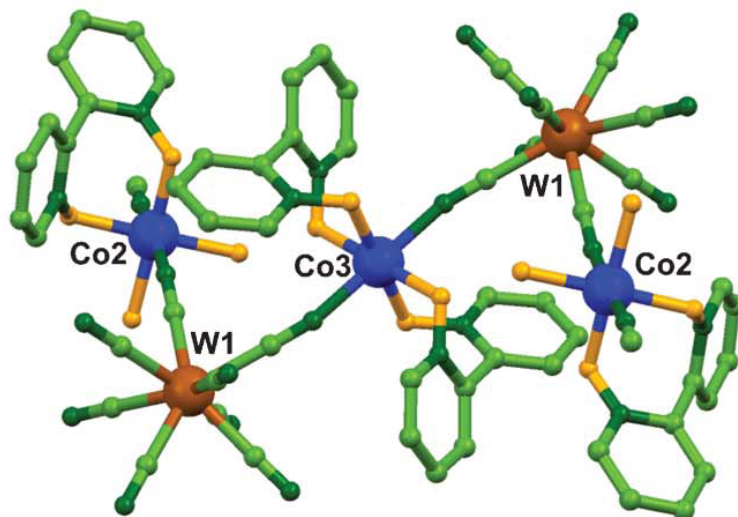


Figure 3.18: A formula unit of $\text{Co}_3^{\text{II}} - \text{W}_2^{\text{V}}$. colours: Co(II) (dark blue), W(V) (brown), C and N (green), O (yellow). Hydrogen atoms and crystallized water molecules are omitted for clarity.

It consists of CN-bridged undulating layers perpendicular to the *a* crystallographic axis, with crystallized water molecules in between. The layers form a brick wall topology and are composed of 36-atoms rings (marked with a red rectangle in fig. 3.19 b)) with alternate Co^{II} and W^{V} centers interlinked with CN-bridges. The geometry of these rings is close to a deformed rectangle with dimensions $19.1 \times 10.3 \text{ \AA}^2$.

Each $[\text{W}(\text{CN})_8]^{3-}$ is linked to three Co^{II} sites of distorted octahedral geometry: two Co(2) along the *b* direction and one Co(3) along the *c* direction.

The W-C-N and Co-N-C angles in the bridging linkages are close to 180° except for one Co-N-C where the angle is equal to 154.4° . Co-W distances within the layer are 5.30, 5.36 and 5.44 \AA , while the shortest distance between metallic centers of neighbouring layers (W1-Co3) is 9.5 \AA [28].

The symmetry of the unit cell is monoclinic (space group $P2_1/c$) with parameters $a = 10.45700(10) \text{ \AA}$, $b = 19.0970(2) \text{ \AA}$, and $c = 17.7070(2) \text{ \AA}$, and angles $\alpha = \gamma = 90^\circ$, $\beta = 91.2120(10)^\circ$.

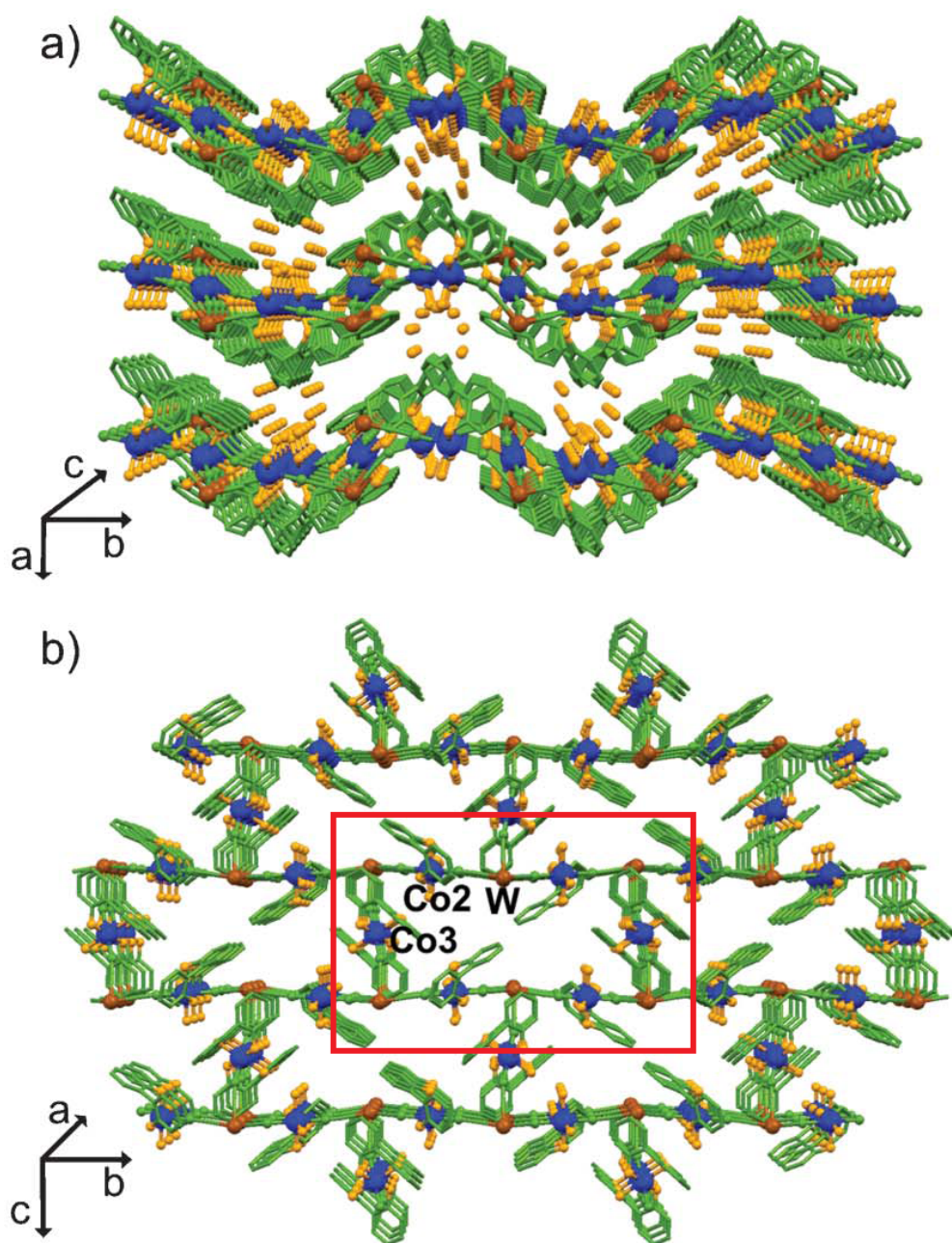


Figure 3.19: The crystal structure of $\text{Co}_3^{\text{II}} - \text{W}_2^{\text{V}}$ along a) c crystallographic axis and b) a crystallographic axis. Colours: Co(II) (dark blue), W(V) (brown), C and N (green), O (yellow). Hydrogen atoms (a) and b)) and crystallized water molecules (b)) are omitted for clarity.

3.2.2 Experimental

The samples were obtained by Szymon Chorąży. For magnetic measurements both powder and single crystal samples were used.

The powder sample's mass weighed on the laboratory scale was 24.0 mg. Similarly to the case in chapter 3.1, it was pressed into a gelatine capsule, of which the magnetic properties were investigated previously (fig. 3.4 and 3.5).

The single crystals were in the shape of rectangular cuboids and of green colour. The largest crystal was selected for the measurements, was however too small to be weighed on our laboratory scale (mass smaller than 1mg), was therefore weighed on a more accurate scale (courtesy of dr hab. Z. Tomkiewicz). The mass of the crystal sample used for the measurements was 0.61 mg.

The crystallographic axes were determined and with respect to those the magnetic measurements along axes a , b and c were performed. Fig. 3.20 shows the method of placing the single crystal sample in the holder in case of all the three measurement series. As in chapter 3.1 the sample was glued with Varnish GE 7031 onto a square 5×5 mm piece of PE sheet and then glued inside the MPMS straw holder (measurements of the PE sheet's magnetic properties in fig. 3.8). Varnish was carefully tested not to dissolve the sample.

The single crystal measurements were supplemented by using a Horizontal Sample Rotator insert for MPMS, which allows measurements at desired angle between the sample's orientation (sample rotated around chosen axis) with the external field. A schematic representation of placing the sample in the holder for a measurement versus rotation angle (rotation around the b crystallographic axis) is presented in fig. 3.21.

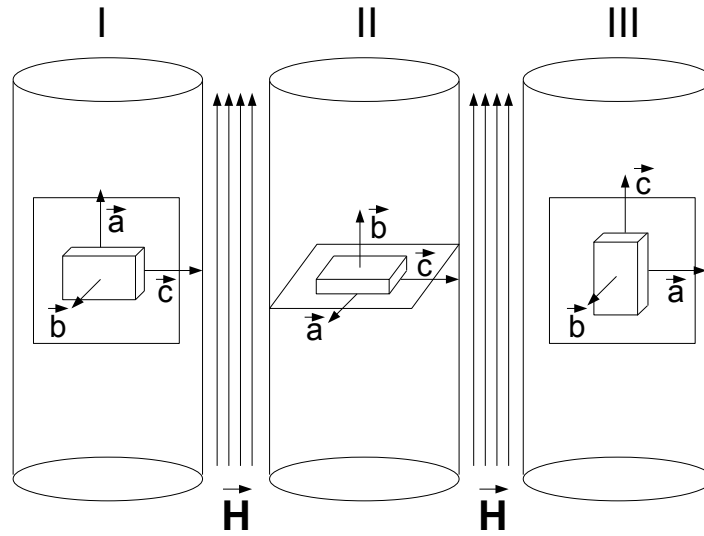


Figure 3.20: The method of placing the cuboidal $\text{Co}_3^{\text{II}} - \text{W}_2^{\text{V}}$ monocrystal inside the straw used for magnetic measurements with magnetic field along a , b and c crystallographic axes (situation I, II and III, respectively)

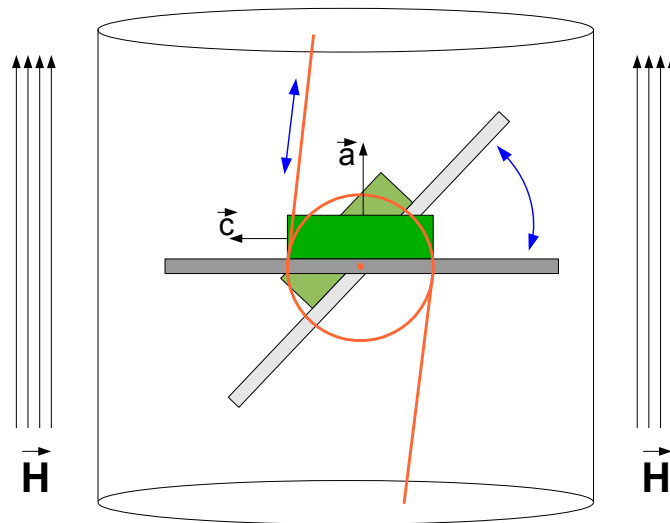


Figure 3.21: A scheme of placing the cuboidal $\text{Co}_3^{\text{II}} - \text{W}_2^{\text{V}}$ monocrystal inside the Horizontal Sample Rotator used for measurements of magnetization versus angle between external field and a (or c) crystallographic axis. Vertical movement (blue) of a thin wire (orange) wound around the rod (transparent for better visibility), on which the sample holder rests, causes angular movement of the sample (green).

3.2.3 Magnetic studies of $\text{Co}_3^{\text{II}} - \text{W}_2^{\text{V}}$

Powder sample measurements

From the structure of the compound it is learned that one formula unit contains two atoms of W^{V} of spin $S_{\text{W}} = 1/2$ and g -factor $g_{\text{W}} = 1.97$ (taken from [29]) and three Co^{II} atoms, for which the situation with the spin and g factor is more complicated, due to the strong orbital contribution to the magnetic moment and thus to a strong magnetic anisotropy (a detailed theoretical approach may be found in [30]).

A measurement was done at field 1 kOe versus temperature. The data was carefully corrected for the diamagnetic contribution of the gelatine capsule (fig. 3.4) and then reciprocal susceptibility versus temperature was computed (fig. 3.22).

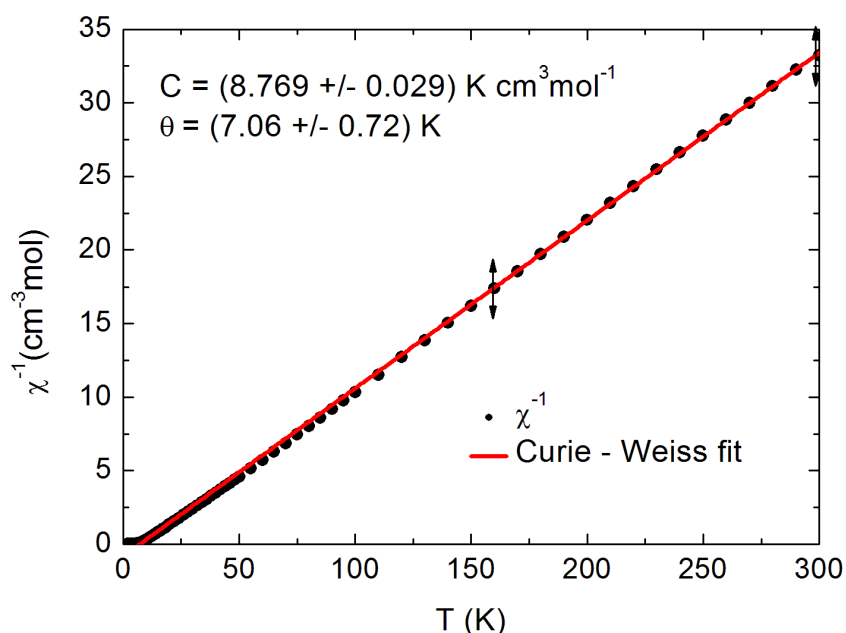


Figure 3.22: Inverse susceptibility of the powder sample of $\text{Co}_3^{\text{II}} - \text{W}_2^{\text{V}}$ versus temperature together with a fit of the Curie-Weiss law (red line) in the range of temperatures 150-300 K.

The Curie-Weiss law fits well with the data at high temperatures (150-300 K), from which the Curie constant $C = 8.77(3) \text{ Kcm}^3/\text{mol}$ and the Weiss temperature $\theta = 7.1(7) \text{ K}$ were obtained. The theoretical calculation of the Curie constant for this system (assuming the $S_{\text{W}} = 1/2$ and $g_{\text{W}} = 1.97$ and applying the range for χT value for a single Co^{II} ion in an octahedral environment of $2.7 - 3.4 \text{ Kcm}^3/\text{mol}$ [30]) gives the range $C_{\text{theor}} = 8.83 - 10.93 \text{ Kcm}^3/\text{mol}$. The value from the fit is

very close to the lower limit of the anticipated range. The positive value of θ indicates predominant ferromagnetic coupling.

Zero-field cooling - field cooling measurement was done next, presented in fig. 3.23.

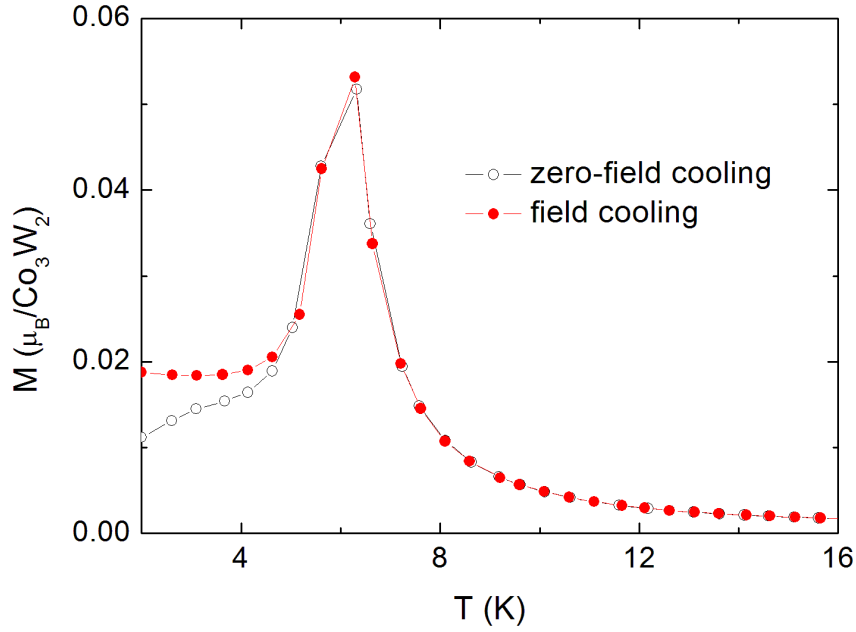


Figure 3.23: Zero-field cooling - field cooling magnetization of the powder sample of $\text{Co}_3^{\text{II}} - \text{W}_2^{\text{V}}$ versus temperature. $H = 10$ Oe. The solid lines are to guide the eye.

The magnetization in zero field reveals a sharp peak around 6K and drops by 60% below 5K. That might indicate an antiferromagnetic order in low fields.

AC measurement of the powder sample was performed at frequency $f_{AC} = 10$ Hz and $H_{AC} = 3$ Oe, results can be found in fig. 3.24.

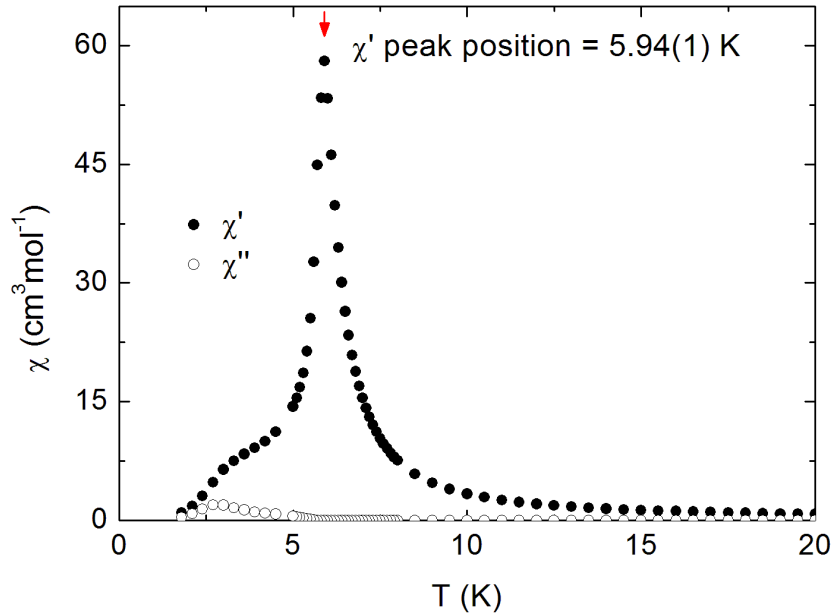


Figure 3.24: AC measurement of the powder sample of $\text{Co}_3^{\text{II}} - \text{W}_2^{\text{V}}$ versus temperature. $f_{AC} = 10$ Hz and $H_{AC} = 3$ Oe.

The real part of the susceptibility reveals a sharp peak at the critical temperature $T_C = 5.94(1)$ K, and confirms the ordering below it, which again appears to be antiferromagnetic at low fields. The imaginary part is mainly negligible, rises slightly around 3 K, which implies dissipation of energy in the system, which will also be investigated further in the single crystal.

Magnetization versus field was measured at $T = 2$ K. The data are presented in fig. 3.25.

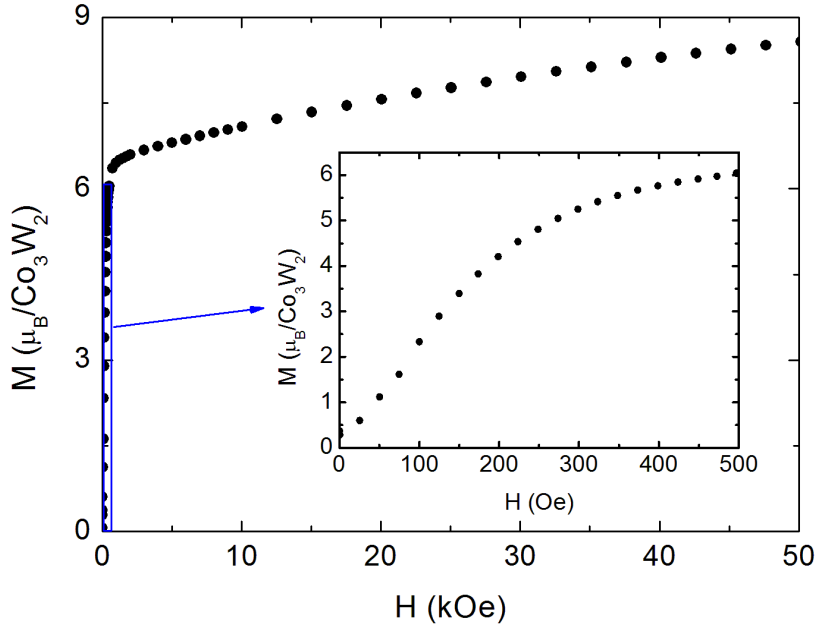


Figure 3.25: Magnetization of the powder sample of $\text{Co}_3^{\text{II}} - \text{W}_2^{\text{V}}$ versus applied field in 2 K. Inset: magnification of the data in the 0-500 Oe range.

The magnetization increases rapidly with the field, reaching the value of $6.35\mu_B$ at around 700 Oe, after which it increases steadily up to the value $8.57\mu_B$ at 50 kOe but does not saturate. The inset in fig. 3.25, which is an enlargement of the magnetization between 0 and 500 Oe, reveals a slight bending around 100 Oe which might imply existence of a spin-flip transition. That will be investigated further in the monocrystalline sample measurements.

To investigate the nature of the ordering of $\text{Co}_3^{\text{II}} - \text{W}_2^{\text{V}}$ further, a measurement versus temperature in various fields was done, results presented in fig. 3.26.

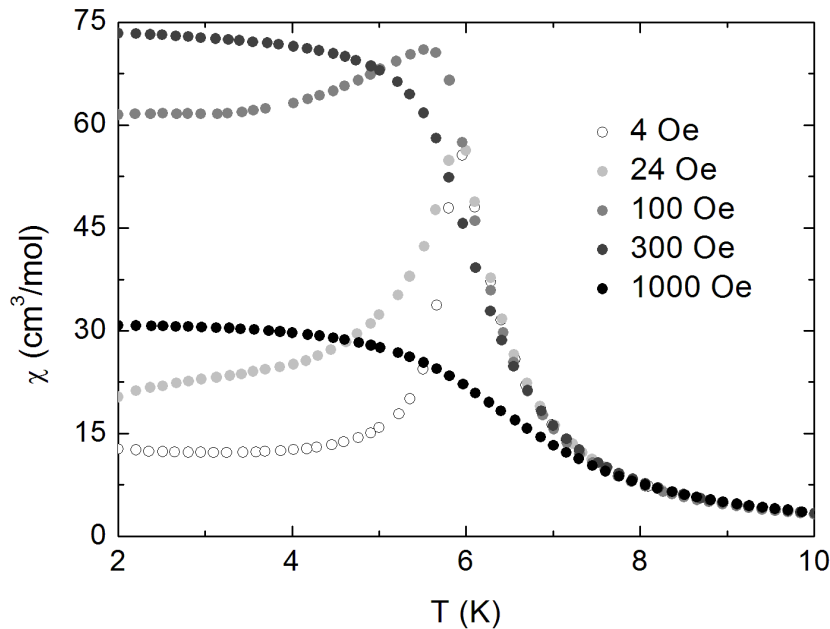


Figure 3.26: Magnetic susceptibility of the powder sample of $\text{Co}_3^{\text{II}} - \text{W}_2^{\text{V}}$ versus temperature in various fields: 4, 24, 100, 300 and 1000 Oe.

Where it was necessary, the low field values were corrected for the remnant field which amounts to approximately 6 Oe. At fields 4 and 24 Oe the susceptibility reveals a sharp peak, implicating antiferromagnetic ordering. At 100 Oe the peak loses its sharpness, to disappear completely at 300 and 1000 Oe, showing ferromagnetic ordering in these fields. The switching appears to happen around the bending in the magnetization versus field curve (fig. 3.25) which again suggests a spin-flip transition there.

Single crystal sample measurements

A measurement of magnetization versus field at $T = 2$ K was taken along a , b and c crystallographic axes (fig. 3.27).

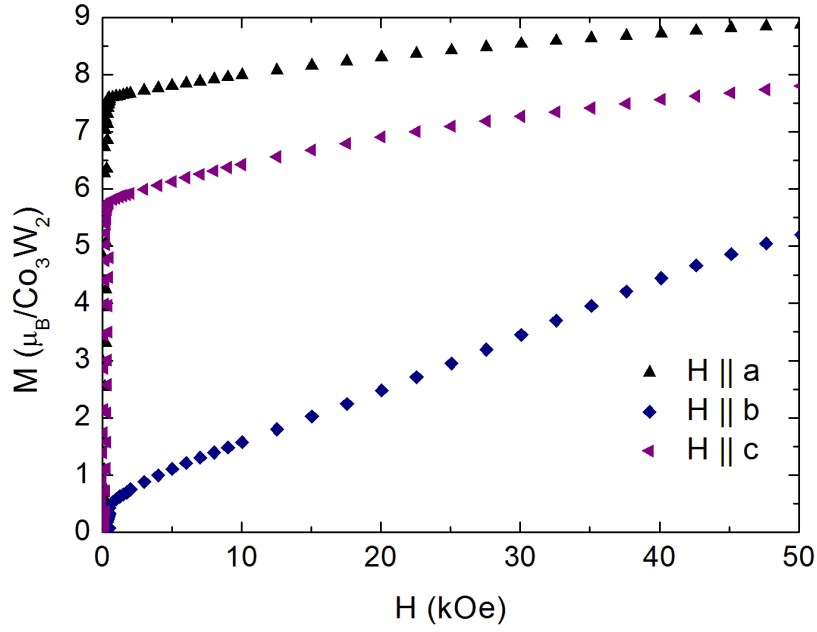


Figure 3.27: Magnetization of a single crystal sample of $\text{Co}_3^{\text{II}} - \text{W}_2^{\text{V}}$ versus field at 2 K along a , b , and c crystallographic axes.

The first conclusion from these data is that b is most likely the hard magnetization axis. However, the magnetization does not reach saturation along neither a nor c , they are therefore unlikely to be the easy magnetization axes. It is only possible to postulate that there is an easy axis in the ac crystallographic plane and that a lies closer to it than c .

A more precise measurement of magnetization in the smaller fields reveals a clear hysteresis with a spin-flip transition around 150 Oe for a and 250 Oe for c crystallographic directions, invisible for b (fig. 3.28). Wherever the spin-flip transition occurs, there is also a small coercive field present.

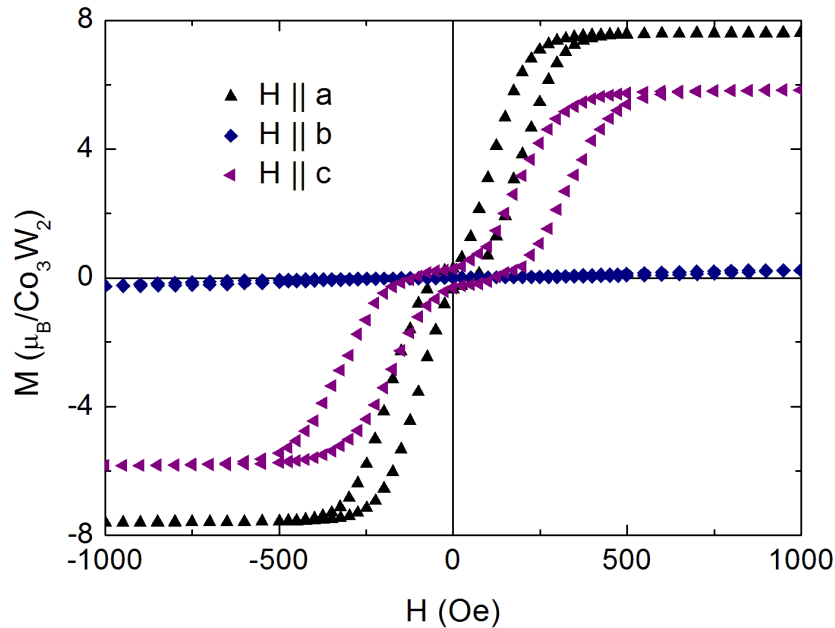


Figure 3.28: Magnetization of a single crystal sample of $\text{Co}_3^{\text{II}} - \text{W}_2^{\text{V}}$ versus field at 2K along a , b and c crystallographic axes in the field range between -1000 and 1000 Oe.

Next, an AC measurement versus temperature was taken along three crystallographic directions with $H_{AC} = 3$ Oe and $f_{AC} = 10$ Hz (data presented in fig. 3.29).

Like in the powder measurement (fig. 3.24), there is a sharp peak in the real part of the susceptibility for a and c directions, for b barely visible, suggesting antiferromagnetic ordering in all the directions below T_C . There is a slight (0.2 K) difference between the positions of the peak for a and c directions. The imaginary parts of susceptibility for all the directions are negligible.

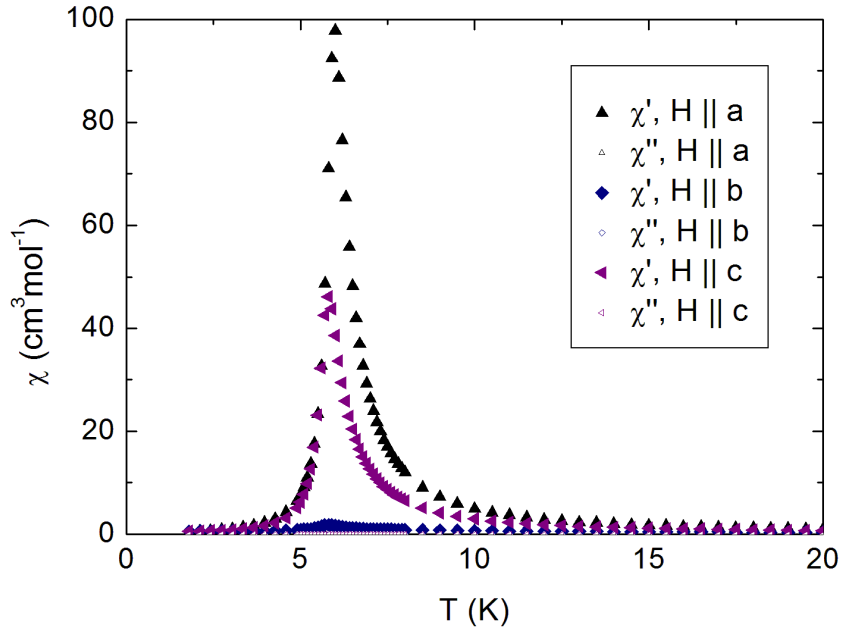


Figure 3.29: AC susceptibility of a single crystal sample of $\text{Co}_3^{\text{II}} - \text{W}_2^{\text{V}}$ versus temperature along a , b and c crystallographic axes. $H_{AC} = 3$ Oe, $f_{AC} = 10$ Hz.

Another measurement in different fields (around 10, 30, 100, 300 and 1000 Oe) was taken along all the crystallographic directions, presented in fig. 3.30. The field values were corrected for the remnant field.

The switching from antiferromagnetic to ferromagnetic ordering is clearly visible for all the crystallographic directions (vanishing of the peak in magnetic susceptibility). However, the field around which it happens differs from one direction to another (100 Oe for a , above 1000 Oe for b and 300 Oe for c), which agrees well with the magnetization versus field measurements (fig. 3.28). A small ferromagnetic impurity is visible for $H \parallel b$ data because the scale is two orders smaller.

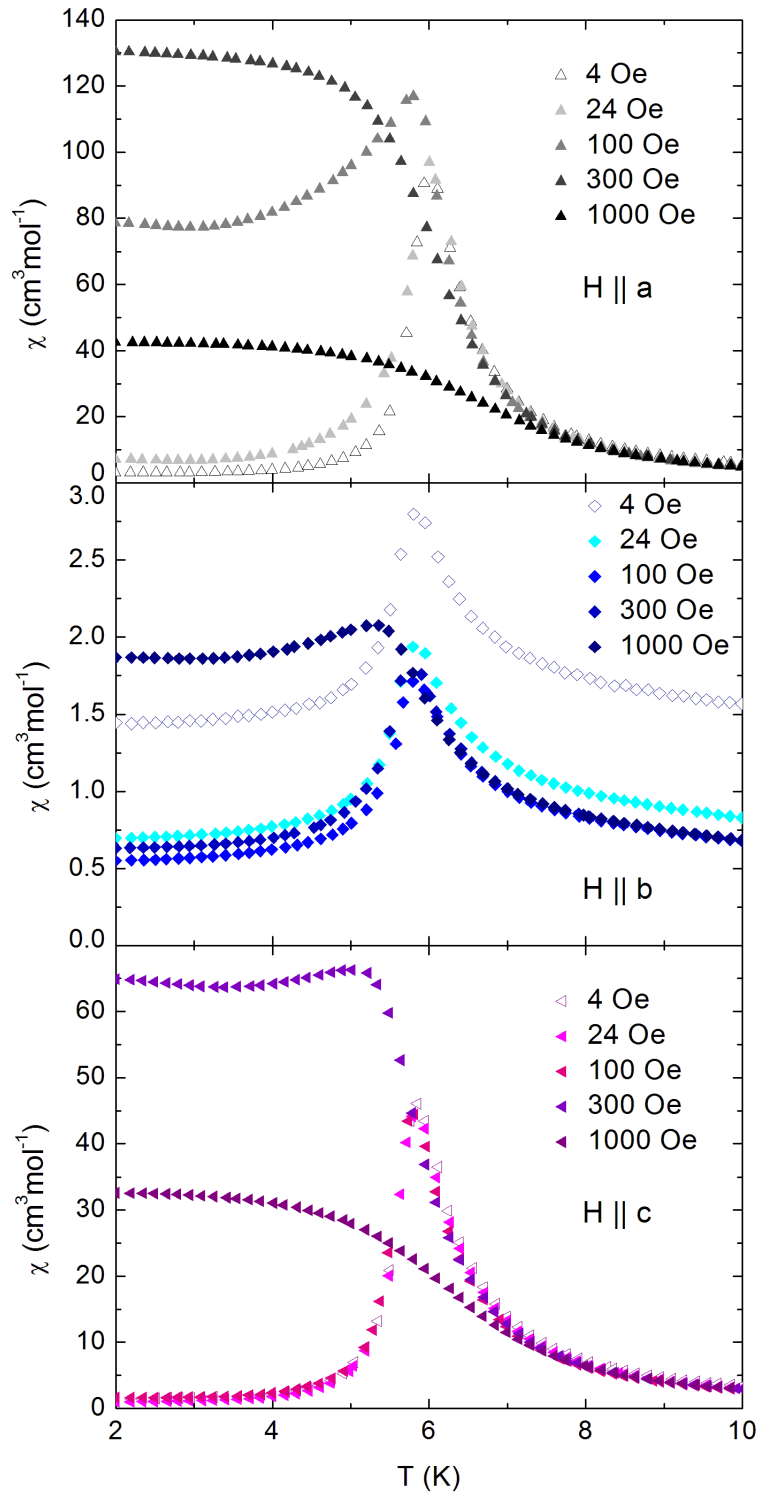


Figure 3.30: Magnetic susceptibility of a single crystal sample of $\text{Co}_3^{\text{II}} - \text{W}_2^{\text{V}}$ versus temperature measured at fields of 10, 30, 100, 300 and 1000 Oe, along a (top), b (middle) and c (bottom) crystallographic directions. The data for $H \parallel b$ are shifted due to a small ferromagnetic impurity visible in this scale.

In order to find the position of the easy axis in the ac crystallographic plane, a measurement using the Horizontal Sample Rotator was undertaken, the sample fixed in such a way that measurement of magnetic signal versus angle of rotation around the b axis was possible (for experimental details, see section 3.2.2).

First, a measurement of magnetization versus angle at $H = 1$ kOe was done (fig. 3.31).

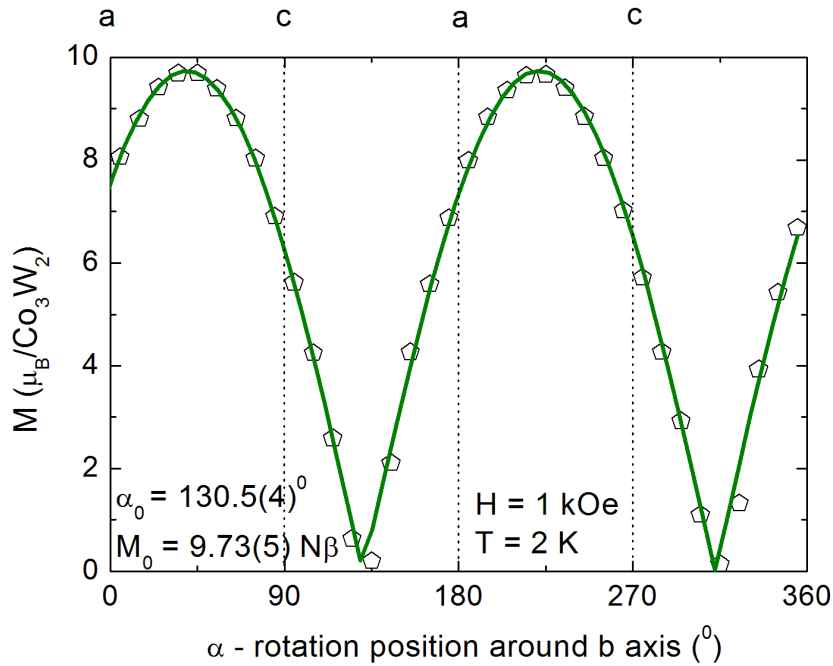


Figure 3.31: Magnetization of a single crystal sample of $\text{Co}_3^{\text{II}} - \text{W}_2^{\text{V}}$ versus angle of rotation around the b crystallographic axis taken at $H = 1$ kOe. Line: fit of $M = M_0 |\sin(\alpha - \alpha_0)|$ to the data.

The magnetization versus angle shows clearly a sine module-like behaviour with magnetization reaching $9.73(5)\mu_B$ in its maximum (showing the position of the easy magnetization axis in the ac plane), and dropping to zero in the minima (where the hard magnetization axis in the ac plane is found). A function $M = M_0 \cdot |\sin(\alpha - \alpha_0)|$ was fitted to the data, finding the position of the hard axis $\alpha_0 = 130.5(4)^\circ$. The easy axis from the fit is therefore $\alpha_0 - 90^\circ = 40.5(4)^\circ$. The scale of the angles was also checked by aligning the sample along the hard axis before extracting it from the magnetometer and measuring the angle by hand. By doing so, the angle between the a axis and the easy magnetization axis was found to be $39(1)^\circ$, and that is the value assumed correct as all the measurements of the angle were influenced by the same error (the starting position of the Sample

Rotator was also aligned by hand).

Despite the small angle hysteresis introduced during rotating the sample in the opposite directions, it was possible to align the monocrystal precisely along the hard and easy direction while the sample was still inside the magnetometer, and therefore measurements of magnetization versus field along the easy and hard axes in 2 K were possible (fig. 3.32).

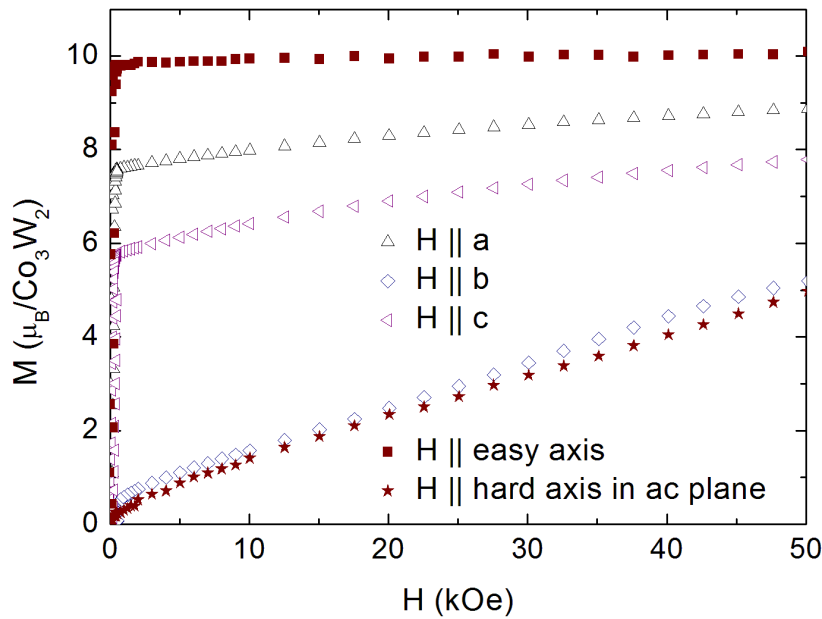


Figure 3.32: Magnetization of a single crystal sample of $\text{Co}_3^{\text{II}} - \text{W}_2^{\text{V}}$ in 2 K versus field measured along easy and hard magnetization axes found by the means of Horizontal Sample Rotator. Magnetization along a , b and c crystallographic directions added for reference (empty points).

Two conclusions can be drawn from this measurement.

One: the signal along the b crystallographic direction and the hard magnetization axis in the ac plane are almost identical, therefore the assumption that b is also very close to a hard magnetization axis was correct. However, the $M(H)$ data for the $H \parallel b$ and for the $H \parallel$ hard axis in the ac plane are slightly deviated from a linear drop to zero, for which there might be several explanations:

- the crystal used was not a perfect monocrystal and/or
- the crystal was not glued perfectly straight to the substrate and/or
- the hard axis does not lie exactly in the ac plane.

Unfortunately, we did not check this for other crystals.

The second observation is that the magnetization quickly reaches saturation at $10\mu_B$ along the easy magnetization axis. It also confirms that the field of 1 kOe was well chosen for the measurement of magnetization versus angle (fig. 3.31) - it was enough to saturate the magnetic moments along the easy axis but the signal along the hard axis was still near zero; hence, it was well described by $|\sin\alpha|$.

A more precise measurement was taken at lower fields, presented in fig. 3.33. The spin-flip transition occurs around 100 Oe along the easy magnetization axis,

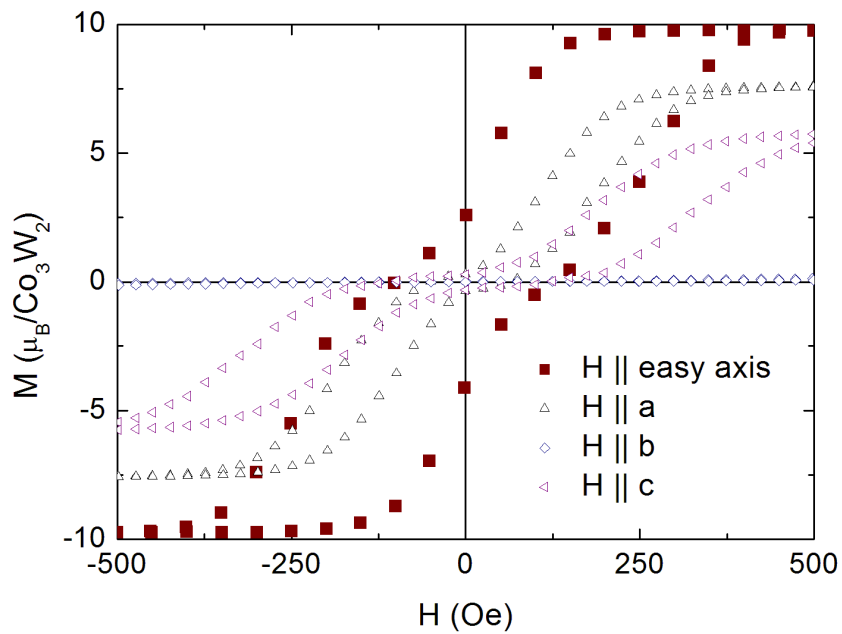


Figure 3.33: Magnetization of a single crystal sample of $\text{Co}_3^{\text{II}} - \text{W}_2^{\text{V}}$ in 2 K versus field along the easy magnetization axis in the field range -500 to 500 Oe. Magnetization along a , b and c crystallographic directions added for reference (empty points).

with a small coercive field. From the reference of similar curves along the crystallographic directions it is possible to conclude that the further from the easy axis, at the higher field the transition occurs (with smaller coercivity), to disappear completely along the hard magnetization direction.

Magnetic structure simulation

The magnetic structure for this compound was modelled using the molecular field approach.

The energy of a Co_6W_4 elementary cell

$$E = - \sum_i \vec{m}_i \cdot \vec{h}_i$$

was minimized (where the summation is over all the metal centers in the cell, \vec{m}_i denotes the individual magnetic moment and \vec{h}_i is the molecular field acting on the metal center i). After taking into account all the atoms in the Co_6W_4 cell (two different orientations of Co3 ions, and two different orientations of Co2 ions in the elementary cell):

$$E = -2\vec{m}_{\text{W}} \cdot \vec{h}_{\text{W}} - 2\vec{m}_{\text{W}'} \cdot \vec{h}_{\text{W}'} - 2\vec{m}_{\text{Co}2} \cdot \vec{h}_{\text{Co}2} - 2\vec{m}_{\text{Co}2'} \cdot \vec{h}_{\text{Co}2'} - 2\vec{m}_{\text{Co}3} \cdot \vec{h}_{\text{Co}3} - 2\vec{m}_{\text{Co}3'} \cdot \vec{h}_{\text{Co}3'}.$$

The molecular field was calculated, assuming the same coupling constants λ between all Co - W pairs, as $\vec{h}_i = \lambda \sum_j \vec{m}_j$ where the sum is over the nearest interacting neighbours of the metal center i :

$$\vec{h}_{\text{W}} = \lambda(\vec{m}_{\text{Co}2} + \vec{m}_{\text{Co}2'} + \vec{m}_{\text{Co}3'}),$$

$$\vec{h}_{\text{W}'} = \lambda(\vec{m}_{\text{Co}2} + \vec{m}_{\text{Co}2'} + \vec{m}_{\text{Co}3}),$$

$$\vec{h}_{\text{Co}2} = h_{\text{Co}2'} = \lambda(\vec{m}_{\text{W}} + \vec{m}_{\text{W}'}),$$

$$\vec{h}_{\text{Co}3} = 2\lambda\vec{m}_{\text{W}'},$$

$$\vec{h}_{\text{Co}3'} = 2\lambda\vec{m}_{\text{W}}.$$

Two sublattices for W ions are taken into account, because of their Co3 or Co3' neighbourhood.

Magnetic moments in the saturation limit (ground state at $T = 0$) are

$$\vec{m}_{\text{W}} = \frac{1}{2} 2 \frac{\vec{h}_{\text{W}}}{h_{\text{W}}} \quad (\text{analogical for W}'),$$

$$\vec{m}_{\text{Co}3} = \frac{1}{2} \hat{R}_{\text{Co}3} \hat{g}_{\text{Co}3} (\hat{R}_{\text{Co}3})^{-1} \frac{\vec{h}_{\text{Co}3}}{h_{\text{Co}3}} \quad (\text{analogical for other Co atoms}),$$

where \hat{R} are rotation matrices of local axes of Co g -tensors. Isotropic g -tensors for W ions with $g = 2.0$ were used. From *ab initio* calculations [28]:

$$\hat{R}_{\text{Co}2} = \begin{pmatrix} 0.488 & 0.310 & -0.805 \\ -0.853 & -0.031 & -0.540 \\ -0.187 & 0.950 & 0.245 \end{pmatrix} \quad \hat{R}_{\text{Co}3} = \begin{pmatrix} -0.330 & -0.447 & 0.824 \\ 0.912 & 0.077 & 0.423 \\ -0.245 & 0.891 & 0.377 \end{pmatrix},$$

and $\hat{g}_{\text{Co}2} = (2.061, 2.950, 7.301)$, $\hat{g}_{\text{Co}3} = (5.396, 4.819, 2.283)$. \hat{R} for Co2 and Co3' are reflected in ac plane.

The equations were solved using *Mathematica* software after parametrization

$$\frac{\vec{h}_W}{h_W} = (\cos\phi_W \sin\theta_W, \sin\phi_W \sin\theta_W, \cos\theta_W) \quad (\text{analogical for } W'),$$

where ϕ_W , $\phi_{W'}$, θ_W and $\theta_{W'}$ are four free parameters. The resulting values and orientations of magnetic moments do not depend on the λ molecular field constant; during simulation $\lambda = 1$ was used. The magnetization energy has the minimum for $\phi_W = 0.073$, $\phi_{W'} = -0.073$, and $\theta_W = 1.118$, and $\theta_{W'} = 1.118$. The total calculated magnetic moments versus the external field direction is presented in are presented in Table 3.1.

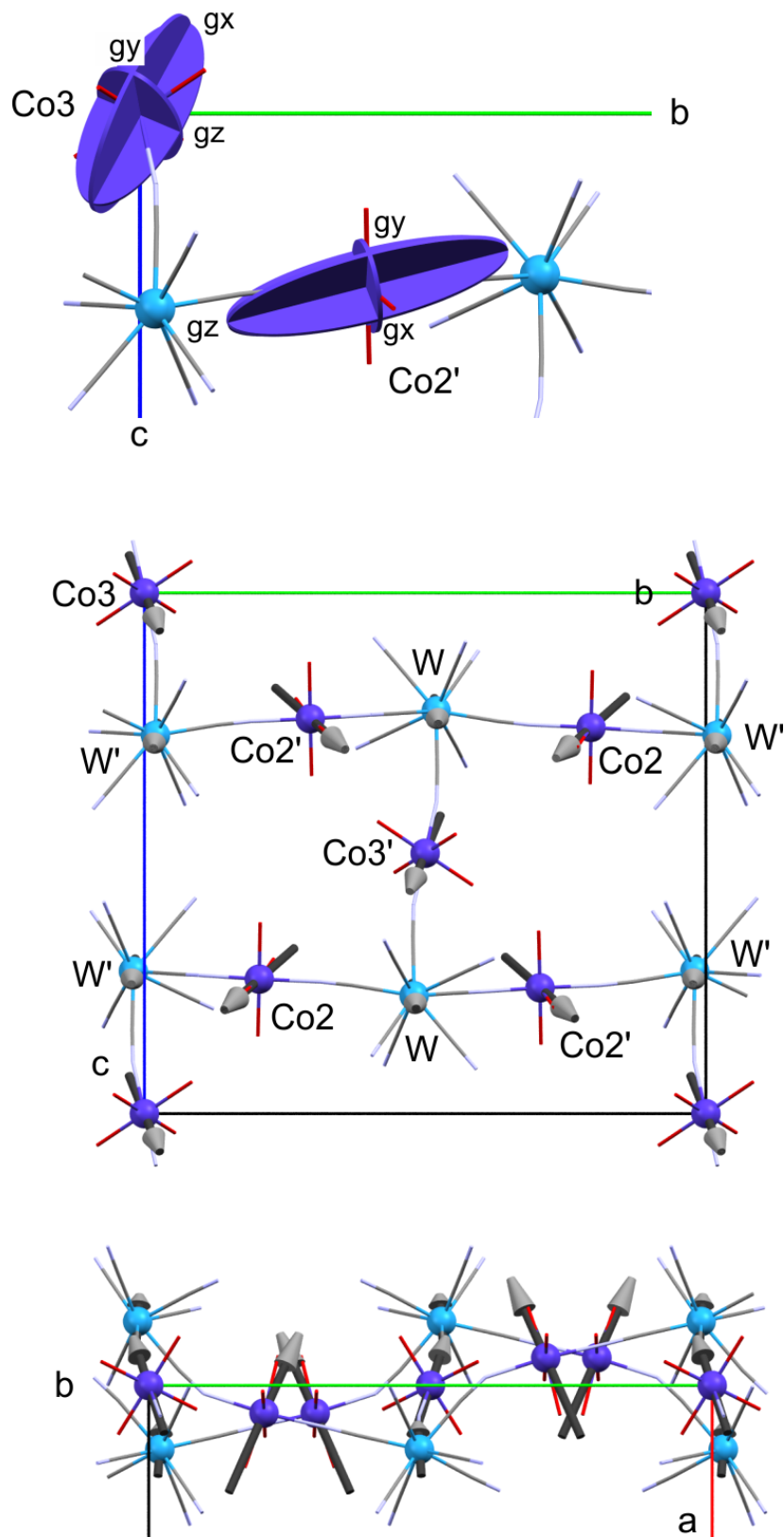
	M_x (μ_B)	M_y (μ_B)	M_z (μ_B)
W	-0.90	-0.07	0.43
W'	-0.90	0.07	0.43
Co3	-1.61	0.52	1.30
Co3'	-1.61	-0.52	1.30
Co2	-2.68	-1.19	1.05
Co2'	-2.68	1.19	1.05
Total/Co ₃ W ₂	-8.76	0.0	4.28

Table 3.1: Calculated magnetic moments of Co₃^{II} – W₂^V along a , b^* and c crystallographic directions.

Following conclusions can be drawn for these calculations:

- The total magnetic moment for a Co₃W₂ unit is $M_a = -8.76\mu_B$, $M_{b^*} = 0$ and $M_c = 4.28\mu_B$.
- The magnetization cancels out along the $b^* = b$ direction, which was found to be the hard magnetization axis from the experimental data.
- It should be stressed that this result was obtained without imposing the crystal glide plane symmetry on the solution (e.g. independent variables for θ_W and $-\theta_{W'}$ were used in minimization of energy).
- The spontaneous magnetization calculated was $9.75\mu_B$, within the ac plane, creating an angle 26° with the a axis, which roughly agrees with the values $9.73(5)\mu_B$ and 39° found by experiment.

The magnetic structure is depicted in fig. 3.34.

Figure 3.34: The magnetic structure of $\text{Co}_3^{\text{II}} - \text{W}_2^{\text{V}}$.

3.2.4 Heat capacity measurement of $\text{Co}_3^{\text{II}} - \text{W}_2^{\text{V}}$

Experimental

The sample chosen for the heat capacity measurements was a number of single crystals which altogether were of mass 3.3 mg. The measurements were done using a Physical Properties Measurements System from Quantum Design (see Chapter 2.2). A measurement of addenda together with a drop of Apiezon N was done before placing the sample onto the platform (for background subtraction). Fig. 3.35 shows the method of placing the crystals on the platform. The crystals

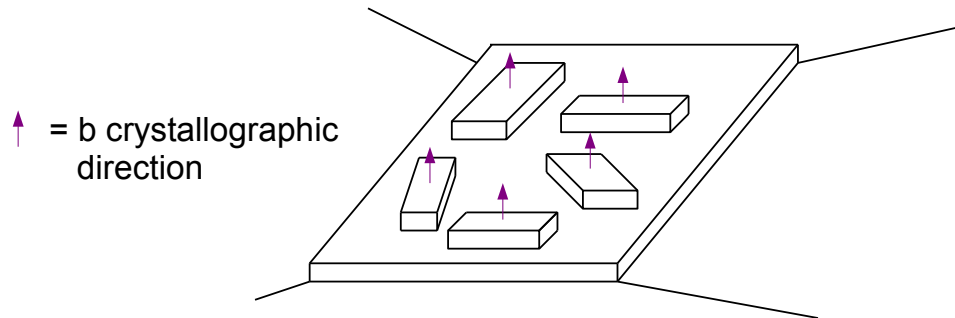


Figure 3.35: The placing of the polycrystalline sample of $\text{Co}_3^{\text{II}} - \text{W}_2^{\text{V}}$ on the sample platform.

were pressed into Apiezon N in a way maximizing the surface contact with the platform, thus ensuring good heat transfer.

Heat capacity results of $\text{Co}_3^{\text{II}} - \text{W}_2^{\text{V}}$ and analysis

The heat capacity was measured in the range 2 - 200 K, in various fields, results shown in fig. 3.36. In zero field a λ - shaped peak is observed, diminishing with the rising field.

The zero-field heat capacity was then fitted with Debye model in order to calculate the phonon heat capacity (fig. 3.37 a)).

The fit was done in the range 26-40 K, resulting in Debye temperature $\theta_D = 151(4)$ K. The phonon background was then subtracted to calculate the magnetic contribution to the heat capacity. A plot of the magnetic heat capacity over temperature versus temperature was done to calculate the magnetic entropy gain (fig. 3.37 b)). The fitting range of the Debye model had an impact on the resulting magnetic heat capacity.

The position of the peak is 5.7 K, agreeing with the magnetic ordering temperature. The plot in fig. 3.37 b) was then integrated over the range 2-25 K,

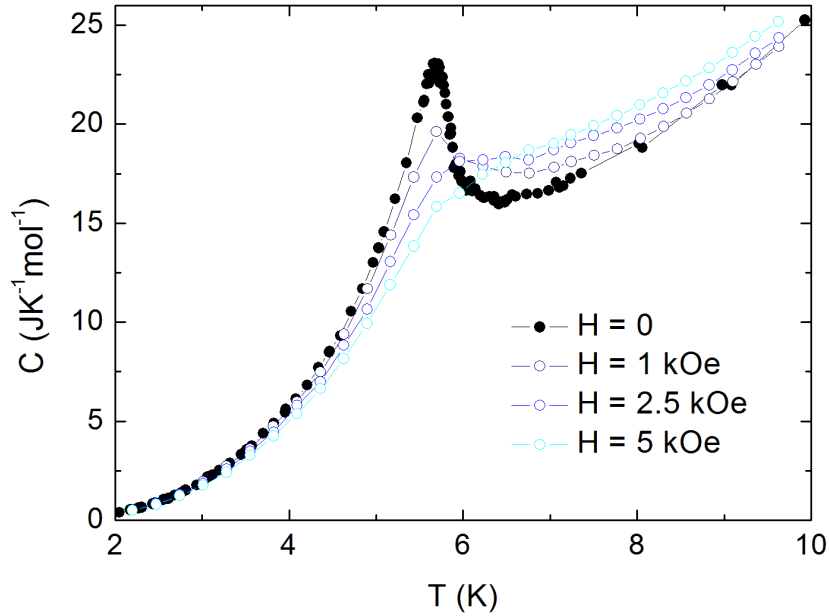


Figure 3.36: Molar heat capacity of a polycrystal sample of $\text{Co}_3^{\text{II}} - \text{W}_2^{\text{V}}$ in different magnetic fields. The solid lines are to guide the eye.

giving the entropy gain $S_{mag} = \int \frac{C_{mag}}{T} dT = 26.5 \text{ JK}^{-1}\text{mol}^{-1}$. Assuming the spin of Co^{II} to be equal to $S_{\text{Co}} = 1/2$ in low temperatures [30], theoretical entropy gain was calculated $S_{th} = \sum_i R \ln(2S_i + 1) = 3R \ln 2 = 28.8 \text{ JK}^{-1}\text{mol}^{-1}$. The value obtained from the measurement agrees well with the calculated one. It can be seen that the most of the entropy is gained above the transition temperature which is characteristic for 2D ferromagnets [31].

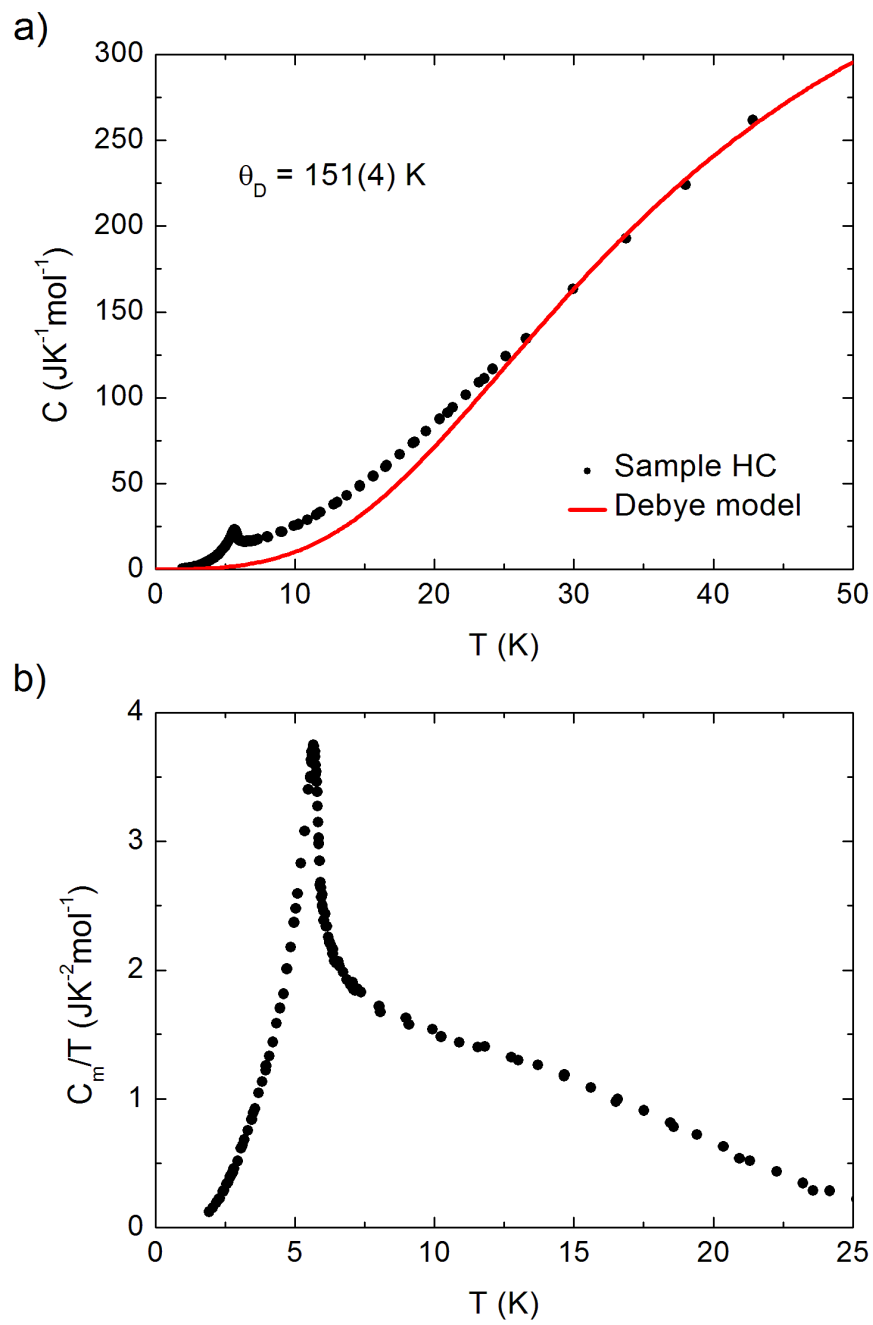


Figure 3.37: Molar heat capacity of a polycrystalline sample of $\text{Co}_3^{\text{II}} - \text{W}_2^{\text{V}}$ in zero magnetic field with Debye fit in the range 26-40 K.

3.2.5 Summary

$\text{Co}_3^{\text{II}} - \text{W}_2^{\text{V}}$ was found to be a strongly anisotropic layered molecular magnet with a soft ferromagnetic phase below 5.94(1) K. The ferromagnetic ordering was confirmed by a Curie-Weiss law fit to the powder sample data, producing a positive θ value. The anisotropy of the compound was thoroughly investigated by experiment and found confirmation in the results of numerical calculations. $\text{Co}_3^{\text{II}} - \text{W}_2^{\text{V}}$ exhibits strong uniaxial anisotropy and the easy magnetization axis was found to lie in the ac crystallographic plane, creating an angle 39° with the a axis (the simulated value being 26°). b crystallographic direction was found to be the hard magnetization direction, which was again confirmed by simulation, magnetization cancelling out along it. In low fields the predominant coupling between the noncolinear ferromagnetic layers is antiferromagnetic, a spin-flip transition to ferromagnetic phase occurs around 100 Oe when the field is applied along the easy direction. The coercivity along the easy axis is approximately 100 Oe, which disappears along the hard magnetization direction. The heat capacity measurements confirmed magnetic ordering below T_C , exhibiting a λ - shaped peak anomaly at 5.7 K.

The findings contained in this Chapter were published in [28].

3.3 $\text{Ni}_2^{\text{II}} - \text{Nb}^{\text{IV}}$ - a water sensitive ferromagnetic network

3.3.1 Structure

The compound investigated is $[\text{Ni}^{\text{II}}(\text{cyclam})]_2[\text{Nb}^{\text{IV}}(\text{CN})_8]$, where cyclam = 1,4,8,11-tetraazacyclotetradecane, from now on $\text{Ni}_2^{\text{II}} - \text{Nb}^{\text{IV}}$ for short. It belongs to a family of compounds which show reversible changes in structure and magnetization when absorbing guest agents from the environment they are placed in [32], [33].

In the case of $\text{Ni}_2^{\text{II}} - \text{Nb}^{\text{IV}}$ determination of the structure was not possible because it was impossible to obtain crystals. However, based on the same formula and the comparison of powder XRD spectra of an analogous compound, containing W instead of Nb, it can be assumed that this compound has a 3D diamond-like structure characterised by a net of intersecting channels. The structure can be modified by partly reversible dehydration [34].

3.3.2 Experimental

The samples were produced by dr Beata Nowicka. The series of samples for magnetic measurements consisted of powder samples subjected to repeated de- and rehydration, which were labelled as:

- 1: As synthesized, immersed in water (mass after drying 6.0 mg)
- 2: 1 dehydrated (8.3 mg)
- 3: 2 rehydrated, immersed in water (mass after drying 4.4 mg)
- 4: 3 dehydrated (6.4 mg)
- 5: 4 rehydrated, immersed in water (mass after drying 3.3 mg)

It should be noted that the samples above were not one and the same sample subjected to de- and rehydration processes, but different samples.

The method of placing the sample inside MPMS system differed from sample to sample:

- Samples **1**, **3** and **5** had to stay immersed in water, were therefore placed in a glass capillary closed on bottom end, then carefully sealed at the top end. A glass tube of the sample diameter was placed below the sample holder to minimize the glass influence on the SQUID signal (fig. 3.38 left)
- Sample **2** was pressed together in a gelatine capsule (see 3.1.2)
- Sample **4** was brought for measurement in a teflon container which was then fitted into the MPMS straw for measurement (fig. 3.38 right)

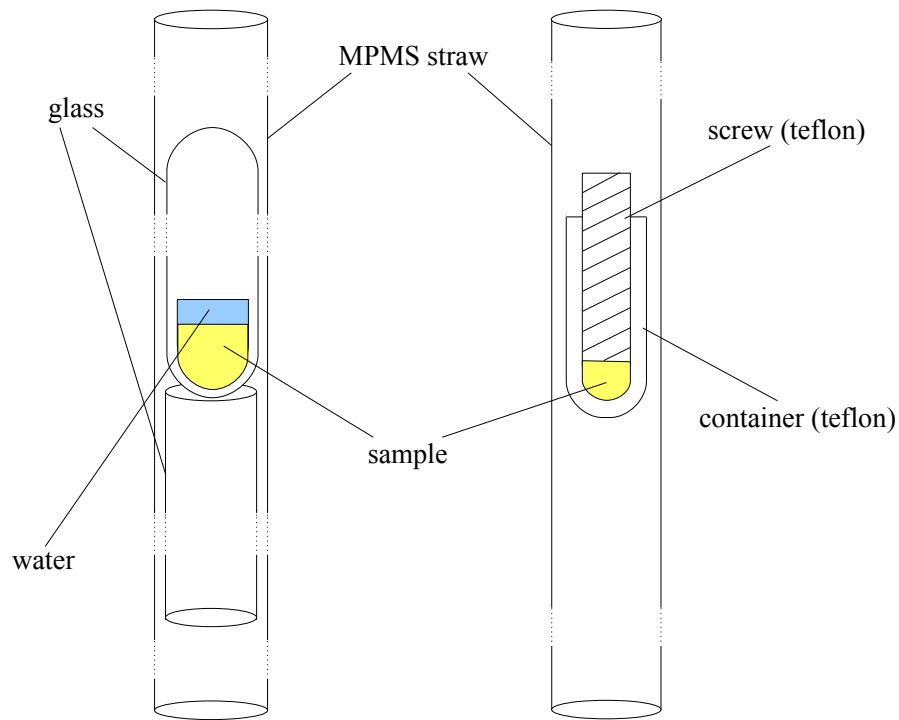


Figure 3.38: Method of placing $\text{Ni}_2^{\text{II}} - \text{Nb}^{\text{IV}}$ powder samples inside an MPMS holder.

3.3.3 Magnetic properties of $\text{Ni}_2^{\text{II}} - \text{Nb}^{\text{IV}}$

Zero-field cooling/field cooling curves for the whole series of samples are presented in fig. 3.39.

Samples **1**, **3** and **5** all reveal a magnetic transition below 12 K, sample **5** showing a probable emergence of a second phase with a peak around 7 K. For dehydrated samples **2** and **4** the magnetic transition is pushed down below 4 K, is however visible in parting of the zero-field cooling and field-cooling curves. The shape of the zfc/fc curves for **2** and **4** reminds of spin glass-like behaviour.

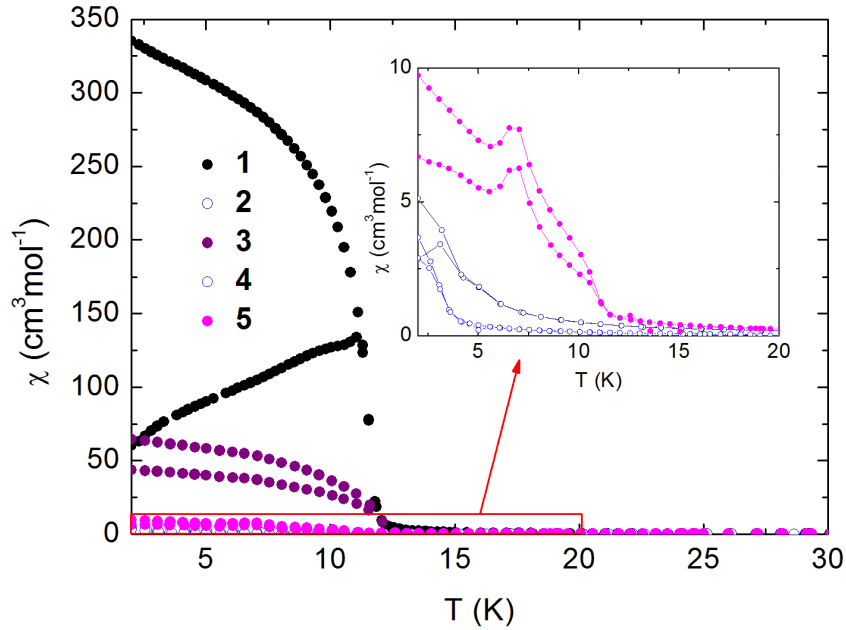


Figure 3.39: Zero-field cooling/field cooling magnetic susceptibility of samples **1-5** versus temperature. Inset: magnification of the data for samples **2**, **4** and **5**. $H = 20$ Oe. The solid lines are to guide the eye.

AC measurements versus temperature were done for samples **1**, **3**, **4** and **5**, results shown in fig. 3.40. For sample **1**, there is only one large, very sharp peak in χ' visible around 12 K, while for the rehydrated samples **3** and **5** two peaks (at 12 K and 7 K) are visible, confirming the existence of two phases. For the dehydrated sample **4** a small peak appears around 3 K.

The χ'' signal is very large for sample **1**, implying the existence of relaxation processes below the ordering temperature. There is a sharp peak at 12 K and a bending around 7 K. For samples **3** and **5**, two rises in χ'' are visible around 12 and below 7 K (for **5** the peak around 12 K is split in two, which may mean a complex relaxation), however the signal is two orders weaker than for the primary sample. For **4** a small peak in χ'' appears below 3 K, suggesting existence of weak relaxation below 3 K, which, together with the peak in χ' , again suggests spin glass-like behaviour.

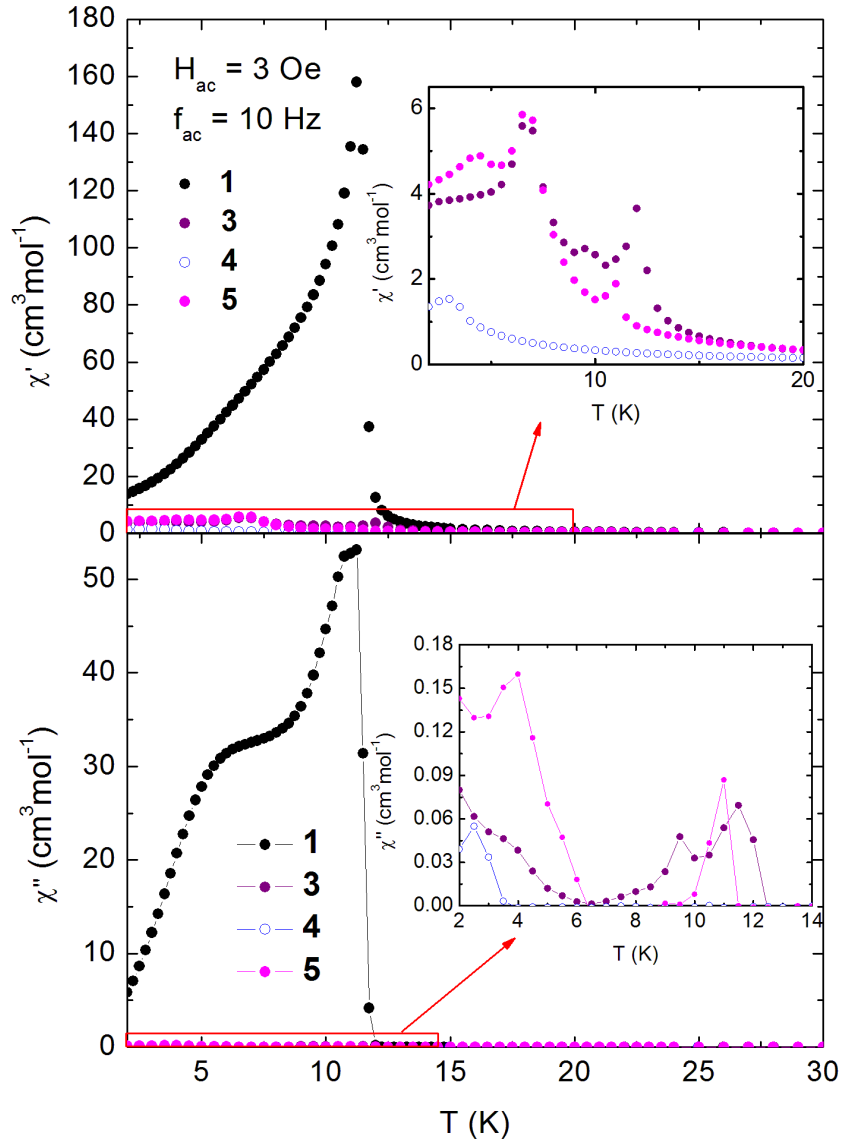


Figure 3.40: Top: AC in-phase susceptibility of samples **1**, **3**, **4** and **5** versus temperature. Inset: magnification of the data for samples **3**, **4** and **5**. Bottom: AC out-of-phase susceptibility of samples **1**, **3**, **4** and **5** versus temperature. Inset: magnification of the data for samples **3**, **4** and **5**. The solid lines are to guide the eye.

All the samples were then measured in the field 1 kOe. $d\chi/dT$ was calculated and fitted with a combination of Lorentzian functions to find the exact critical temperatures for all the phases (fig. 3.41).

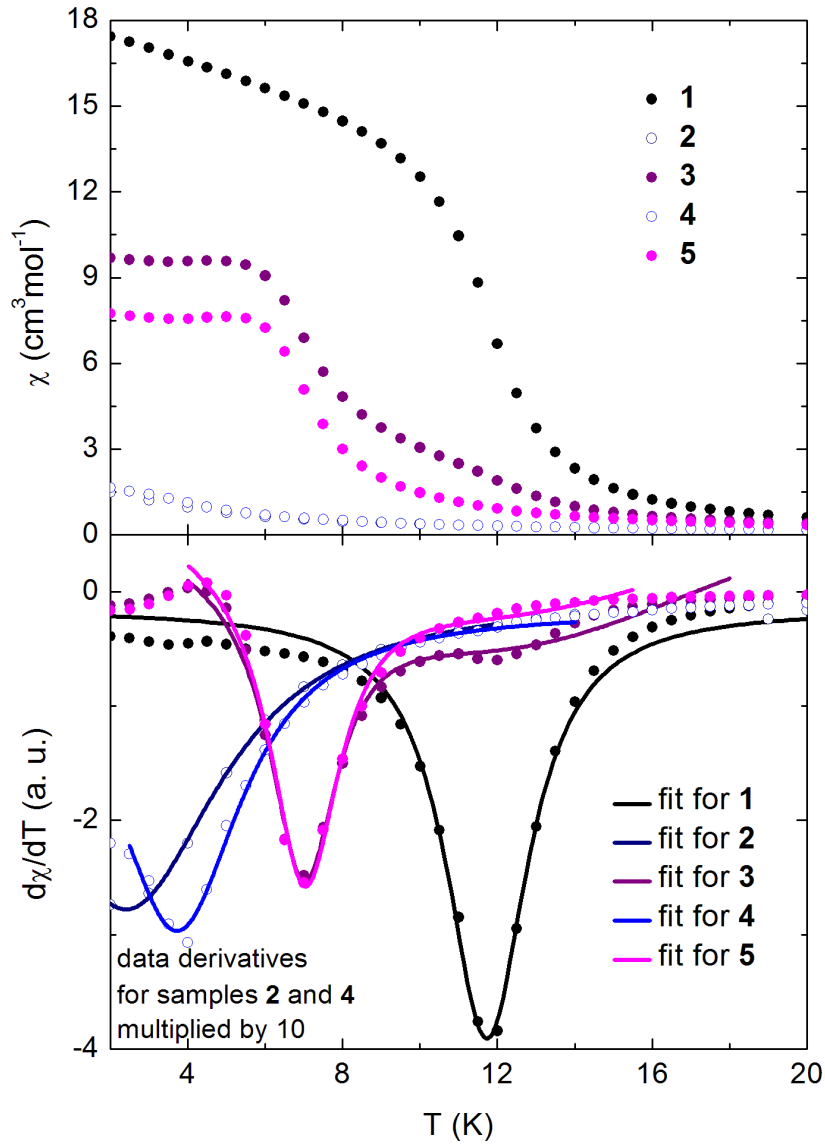


Figure 3.41: Magnetic susceptibility in 1 kOe versus temperature for samples **1-5** (top) with derivatives of the susceptibility along with Lorentzian fits (bottom). $d\chi/dT$ was multiplied by a factor of 10 for samples **2** and **4** for better visibility.

The details of critical temperatures are presented in Table 3.2.

For sample **1** only one phase is present, ordering around 12 K. For the re-hydrated samples **3** and **5** this phase is still present, but a new phase emerges

Sample	Phase 1	Phase 2	Phase 3
1	11.72(4) K	X	X
2	X	X	2.41(5) K
3	12.1(6) K	6.99(4) K	X
4	X	X	3.72(3) K
5	12.1(9) K	7.02(3) K	X

Table 3.2: Critical temperatures in samples **1-5** with the probable distinction of phases.

with ordering temperature around 7 K. For the dehydrated samples **2** and **4** there is only one phase present, with critical temperature below 4 K. This suggests destroying of the original phase completely by the dehydration process, which is then partially restored by rehydration, and simultaneously a new phase is created.

The data are also presented as $\chi \cdot T$ versus temperature in fig. 3.42.

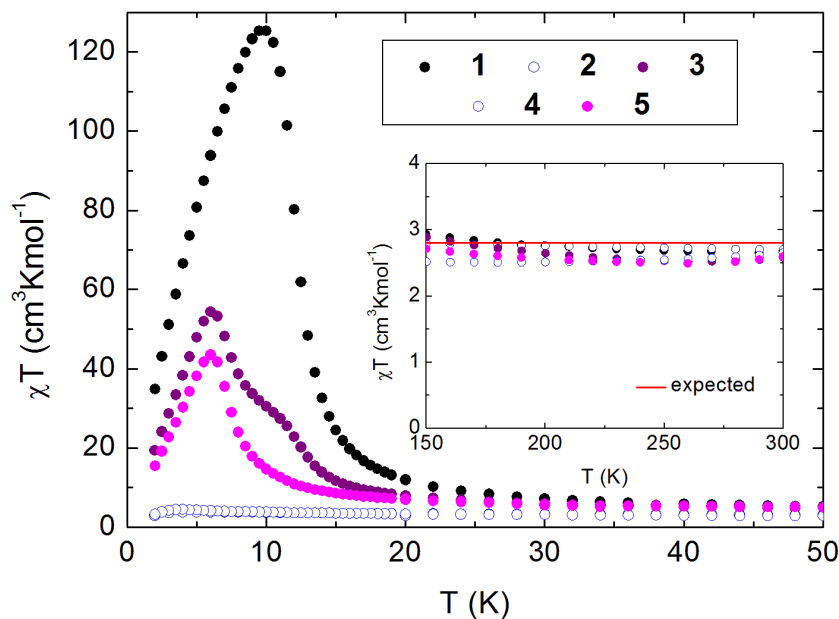


Figure 3.42: Magnetic susceptibility times temperature versus temperature for samples **1-5**. Inset: high temperature data with the expected value (red line).

As it was impossible to measure the diamagnetic contribution prior to the actual measurement because of the differing amount of water in samples **1**, **3** and **5**, it was taken into account while performing the fits of the data in high temperatures (150 - 300 K) with the Curie-Weiss law (not shown). That permitted

to estimate the diamagnetic contribution as the third parameter in the fit. The results are presented in Table 3.3.

Sample	θ (K)	C ($\text{cm}^3\text{Kmol}^{-1}$)	M_D (emu)
1	26.1(7)	2.43(1)	$-2.94 \cdot 10^{-4}$
2	3.7(5)	2.78(1)	$-2.69 \cdot 10^{-5}$
3	28(1)	2.43(2)	$-2.11 \cdot 10^{-4}$
4	3.0(9)	2.56(2)	$-2.56 \cdot 10^{-5}$
5	24(2)	2.22(3)	$2.05 \cdot 10^{-4}$

Table 3.3: Curie-Weiss temperatures, Curie constants and probable diamagnetic contributions of samples **1-5**.

A formula unit of $\text{Ni}_2^{\text{II}} - \text{Nb}^{\text{IV}}$ consists of two Ni^{II} ions with expected $S_{\text{Ni}} = 1$ and $g_{\text{Ni}} = 2.2$ and one Nb^{IV} ion with expected $S_{\text{Nb}} = 1/2$ and $g_{\text{Nb}} = 2.0$. All the Curie constants are close to the expected $2.8 \text{ cm}^3\text{Kmol}^{-1}$ for this spin configuration. The Curie-Weiss temperatures are all positive, indicating predominant ferromagnetic interactions, for the dehydrated samples **2** and **4**, however, severely decreased.

The diamagnetic contribution M_D for samples **1-4** agrees with the expectations: for the samples immersed in water it is one order of magnitude larger than for the dried ones. However, the impurity for sample **5** is positive, which may be caused by the misalignment of the glass tube placed below the sample.

A measurement of magnetization versus field in $T = 2$ K was performed (fig. 3.43). The maximum value of magnetization for this compound is $5.4\mu_B$ per formula unit. That value is not reached by any of the samples. However, none of them saturate in 50 kOe. Sample **1** reaches a value of $5.1\mu_B$, rehydrated samples **3** and **5** $4.5\mu_B$ and dehydrated samples **2** and **4** $4.0\mu_B$. This would suggest that dehydration damages the interaction between metal centers, and rehydration restores it only to a certain extent. A sum of respective Brillouin functions for spins of two Ni^{II} and one Nb^{IV} was added for reference (red line in fig. 3.43).

The measurement also revealed interesting hysteretic behaviour (fig. 3.44). The primary sample **1** reveals a classic hysteresis with a small coercive field 100 Oe. Hysteretic loop shrinks and distorts significantly for dehydrated samples **2** and **4**, with coercive fields 20 and 40 Oe, respectively. The shape of the hysteresis for the dehydrated samples suggests spin glass-like behaviour. For the rehydrated ones **3** and **5** hysteresis is restored in a more complex form, which may suggest development of a multi-phase system. One phase seems to be ferromagnetically ordered (possibly the same phase as in **1**), the other can be an antiferromagnetic system with a spin-flip transition around 700 Oe.

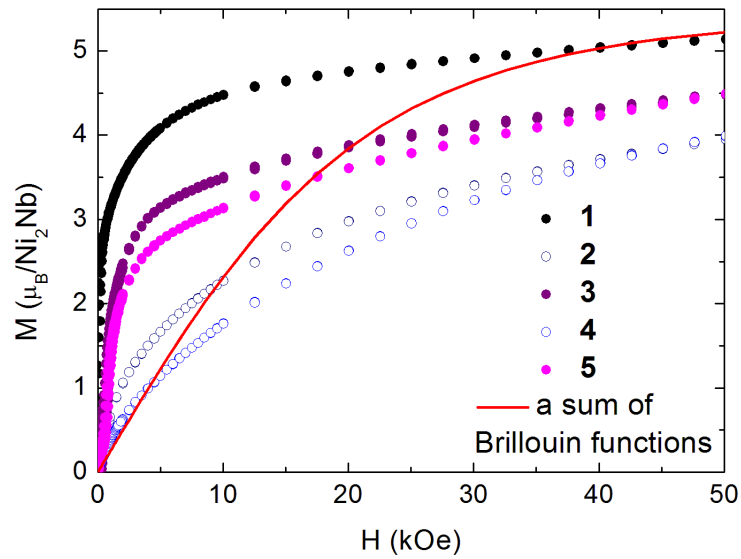


Figure 3.43: Magnetization of samples **1-5** versus field in $T = 2$ K. Sum of Brillouin functions for this spin configuration added for reference (red line).

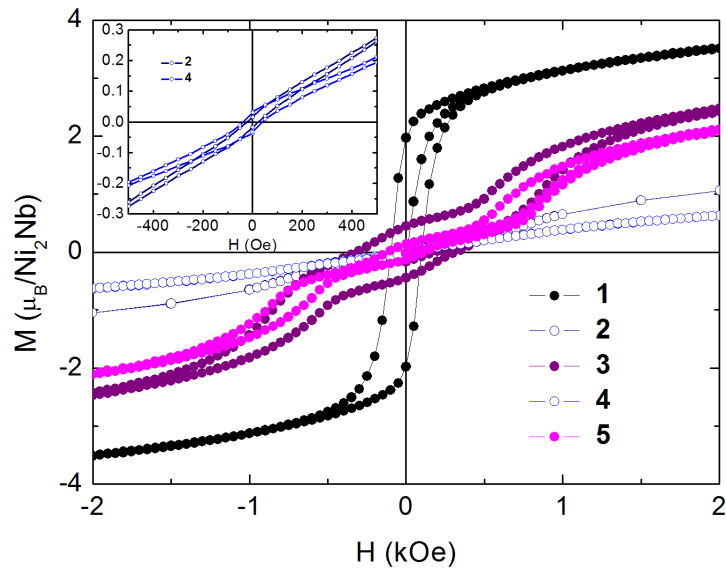


Figure 3.44: Magnetization of samples **1-5** versus field in $T = 2$ K (magnified in the range -2 to 2 kOe). The solid lines are to guide the eye. Inset: magnification of the data for samples **2** and **4**.

3.3.4 Summary

The compound $\text{Ni}_2^{\text{II}} - \text{Nb}^{\text{IV}}$ was proven to be a soft ferromagnet with $T_C = 11.7$ K, with water-sensitive magnetic properties. Dehydration destroys the phase ordered in 12 K, pushing the critical temperature below 4 K and creating a spin glass-like phase, which is suggested by the zfc/fc curves for samples **2** and **4**, the AC behaviour and the existence of a distorted hysteresis in low temperatures. Rehydration of the sample causes a partial restoring of the 12 K phase and creation of a new phase, ordered in 7 K, which shows in restoring the hysteresis in a distorted form and is visible both in AC and DC measurements. The $\text{Ni}_2^{\text{II}} - \text{Nb}^{\text{IV}}$ system was not completely repeatable, the impurities differing from one production series to another. The magnitude of magnetization and coercive fields differed slightly for samples from different series, the shape of the data was however similar. The data presented in this Chapter were chosen from a series of eight samples as the most representative.

The magnetic characterization of this compound was published in [34].

3.4 $\text{Cu}^{\text{II}} - \text{Mo}^{\text{V}}$ and $\text{Cu}^{\text{II}} - \text{W}^{\text{V}}$ with incorporated guanidinium ions: double-layers magnetic system

3.4.1 Structure

$(\text{Hgua})_2\text{Cu}_2^{\text{II}}[\text{Mo}^{\text{V}}(\text{CN})_8]_2$ and $(\text{Hgua})_2\text{Cu}_2^{\text{II}}[\text{W}^{\text{V}}(\text{CN})_8]_2$, where Hgua is a guanidinium ion $\text{H}_2\text{N}=\text{C}(\text{NH}_2)_2$ H-bond in the structure (from now on called $\text{Cu}^{\text{II}} - \text{Mo}^{\text{V}}$ and $\text{Cu}^{\text{II}} - \text{W}^{\text{V}}$, respectively), are isomorphous, differing only in the central atom type in octacyanidometallate building block. The crystal structure consists of cyano-bridged $\{\text{Cu}_2^{\text{II}}[\text{M}^{\text{V}}(\text{CN})_8]_2\}_n$ ($\text{M} = \text{Mo}, \text{W}$) double layers with guanidinium ions between them, as shown in fig. 3.45 [35].

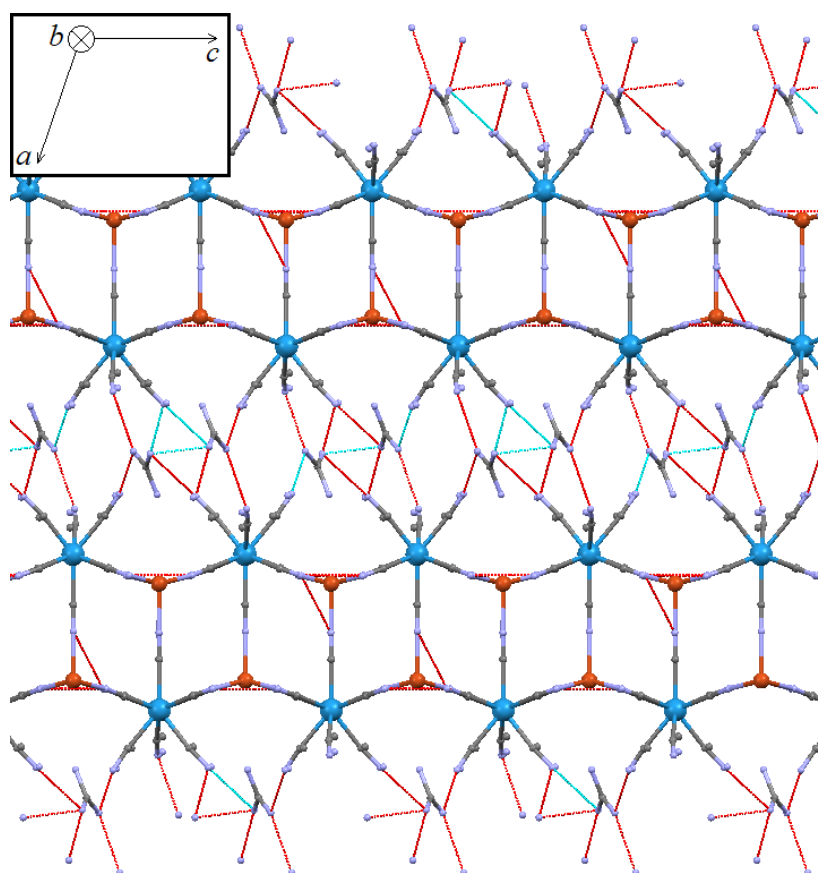


Figure 3.45: The structure of $\text{Cu}^{\text{II}} - \text{Mo}^{\text{V}}$ and $\text{Cu}^{\text{II}} - \text{W}^{\text{V}}$ (viewed along b). Colours: Cu^{II} ions - orange, M^{V} ($= \text{W}^{\text{V}}$ or Mo^{V}) - blue.

The unit cell of $\text{Cu}^{\text{II}} - \text{M}^{\text{V}}$ is monoclinic, space group $C2/c$, and the dimensions are as follows: $a = 33.1260(5) \text{ \AA}$, $b = 7.0000(2) \text{ \AA}$, $c = 14.8090(11)$, $\alpha = \gamma = 90^\circ$, $\beta = 109.283(2)^\circ$.

3.4.2 Experimental

The samples were produced by Olaf Stefańczyk.

Both the samples were in powder form, measured in gelatine capsules described in detail in chapter 3.1.2. During the measurements, however, it was learned that a field of 1 kOe is sufficient to turn the grains of the sample and therefore falsify the results, which will be demonstrated in the following section of this Chapter. To overcome this problem, the measurements were repeated with samples pressed more tightly in the capsule and with samples flooded with Varnish GE 7031 (chapter 3.1.2) inside the capsule.

The samples also contained an irremovable ferromagnetic contaminant. Therefore, it was impossible to fit the Curie Weiss law accurately to the data directly. To eliminate this problem, the measurements were done in 3 and 5 kOe to subtract the saturated ferromagnetic component.

3.4.3 Magnetic properties of $\text{Cu}^{\text{II}} - \text{Mo}^{\text{V}}$ and $\text{Cu}^{\text{II}} - \text{W}^{\text{V}}$

A measurement of magnetic signal in 1 kOe versus temperature was performed in order to gain the data for a Curie-Weiss law fit. However, it was found that both the samples include a ferromagnetic contaminant independent of handling the sample. Therefore, measurements were done in 3 kOe and 5 kOe to saturate the contamination, with the intention of fitting the Curie-Weiss law to the subtracted data in high temperatures and therefore solving the problem. The reciprocal susceptibilities from all the measurements, after a careful correction for the diamagnetic contribution, are presented in fig. 3.46 to give the idea about the size of the contamination.

From these data we can calculate the ferromagnetic contamination to be of the range $10^{-3} \text{ cm}^3\text{mol}^{-1}$, which is around 35% of the signal in the room temperatures for $\text{Cu}^{\text{II}} - \text{Mo}^{\text{V}}$ and around 20% for $\text{Cu}^{\text{II}} - \text{W}^{\text{V}}$.

The Curie-Weiss law was fitted to the subtracted data as can be seen in fig. 3.47. The Curie constants found from the fit are $C_{\text{Cu-Mo}} = 0.828(2) \text{ cm}^3\text{Kmol}^{-1}$ and $C_{\text{Cu-W}} = 0.824(1) \text{ cm}^3\text{Kmol}^{-1}$ which are both in perfect agreement with the expected value of $C_{\text{calc}} = 0.829 \text{ cm}^3\text{Kmol}^{-1}$ for these systems (assuming the isotropic Landé factor $g_{\text{M}} = 2.0$ for both Mo^{V} and W^{V} and $g_{\text{Cu}^{\text{II}}} = 2.2$). The Weiss temperatures were found as $\theta_{\text{Cu-Mo}} = 55.1(6) \text{ K}$ and $\theta_{\text{Cu-W}} = 63.5(2) \text{ K}$. These suggest a predominant ferromagnetic interaction in both compounds.

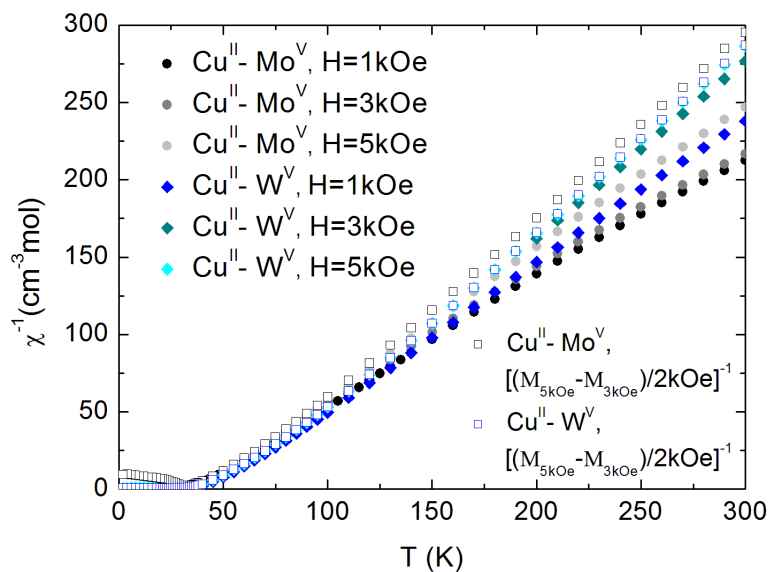


Figure 3.46: Comparison of reciprocal susceptibilities versus temperature for samples $\text{Cu}^{\text{II}} - \text{Mo}^{\text{V}}$ and $\text{Cu}^{\text{II}} - \text{W}^{\text{V}}$ measured at fields 1, 3 and 5 kOe. Inverse of the subtracted susceptibility of 5 and 3 kOe added for comparison (empty symbols).

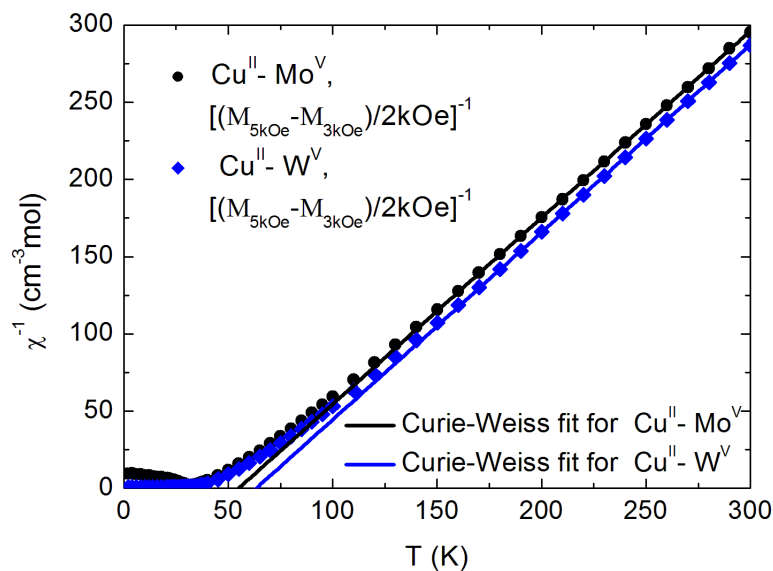


Figure 3.47: Reciprocal subtracted susceptibilities versus temperature for samples $\text{Cu}^{\text{II}} - \text{Mo}^{\text{V}}$ and $\text{Cu}^{\text{II}} - \text{W}^{\text{V}}$ with the fits of the Curie-Weiss law in the range 200-300 K.

Zero-field cooling - field cooling measurements are presented in fig. 3.48.

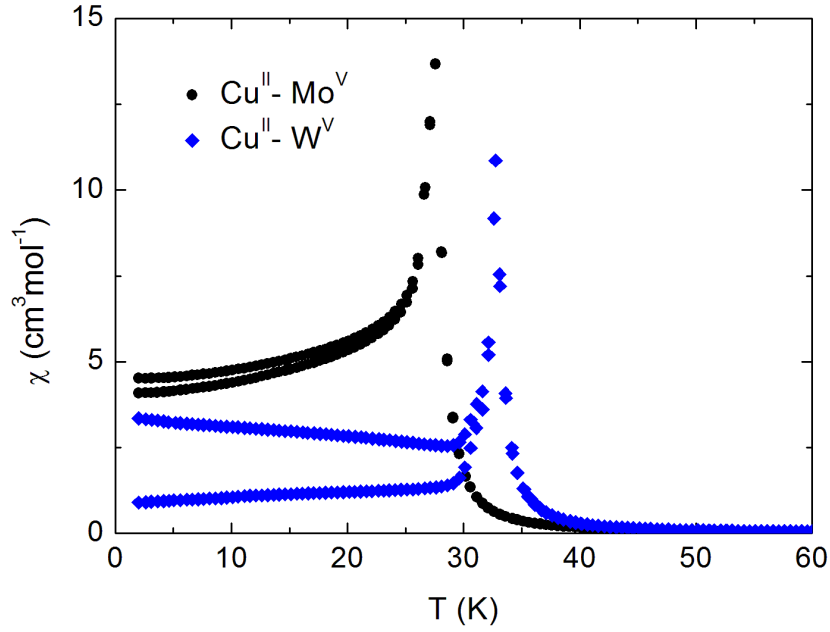


Figure 3.48: Magnetic zero-field cooling/field-cooling susceptibility for samples $\text{Cu}^{\text{II}} - \text{Mo}^{\text{V}}$ and $\text{Cu}^{\text{II}} - \text{W}^{\text{V}}$. $H = 20$ Oe.

For both the samples ZFC/FC curves show a very sharp peak and small irreversibility which suggest antiferromagnetic ordering in low fields (measurement was done at $H = 20$ Oe). The critical temperatures were found to be $T_C^{\text{Cu-Mo}} = 27.5$ K and $T_C^{\text{Cu-W}} = 32.8$ K.

AC measurements were performed for both of the samples at $H_{AC} = 3$ Oe and $f_{AC} = 10$ Hz. Data are shown in fig. 3.49.

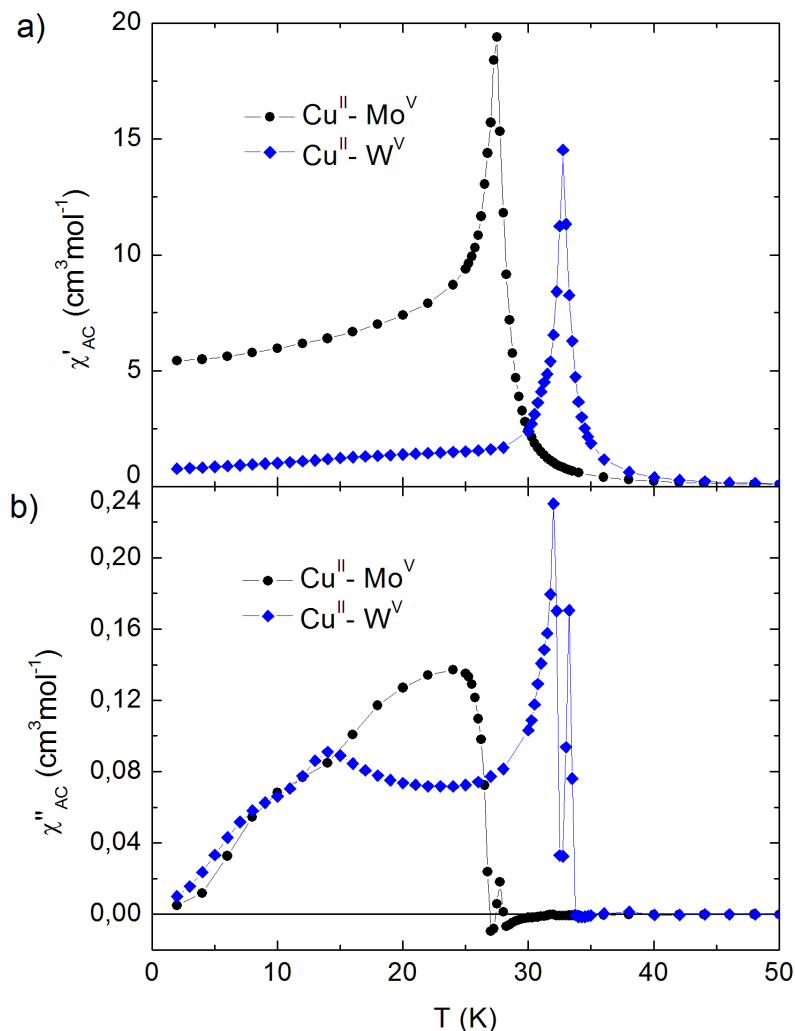


Figure 3.49: AC magnetic susceptibility versus temperature for samples $\text{Cu}^{\text{II}} - \text{Mo}^{\text{V}}$ and $\text{Cu}^{\text{II}} - \text{W}^{\text{V}}$: a) in-phase susceptibility, b) out-of-phase susceptibility. $H_{AC} = 3$ Oe and $f_{AC} = 10$ Hz.

The in-phase AC susceptibilities for both the samples display sharp maxima, confirming antiferromagnetic ordering below T_C at low fields (fig. 3.49 a)). The out-of-phase susceptibility is much smaller, but present below the ordering temperatures. χ'' for both of the compounds displays an unusual double-peak behaviour around the T_C . That suggests two relaxation processes.

A measurement of magnetization versus field in 2 K was performed. The data revealed a problem with the samples which were not pressed tightly enough within the capsules, so the measurement was repeated for samples pressed tightly in the capsules and with a set flooded with glue and dried inside the capsule to prevent movement of the grains. The differences are gathered in fig. 3.50 a).

It can be seen that for the loosely pressed sample a field of around 1 kOe is enough to produce a magnetic moment large enough to turn the grains of the powder and hence falsify the magnetic signal as larger than in an immobile sample. The results for samples pressed tightly in the capsule and the samples immersed in glue are similar.

A measurement of magnetization of the 'glued' sample was chosen as the best representation of the powder sample (fig. 3.50 b)). Also, the samples displayed a hysteresis, which can be found enlarged in the inset in fig. 3.50 b).

The magnetization of the samples quickly reaches the value of $1.5\mu_B$ and $1.0\mu_B$, for $\text{Cu}^{\text{II}} - \text{Mo}^{\text{V}}$ and $\text{Cu}^{\text{II}} - \text{W}^{\text{V}}$, respectively and then rises slowly to reach $1.9\mu_B$ and $1.8\mu_B$ but does not saturate for either of the samples. The expected value of maximum magnetization is the same for both compounds and equal to $2.1\mu_B$.

From the enlarged hysteretic loops it is clearly visible that a spin-flip transition occurs for $\text{Cu}^{\text{II}} - \text{W}^{\text{V}}$ around 140 Oe. For $\text{Cu}^{\text{II}} - \text{Mo}^{\text{V}}$ the same might occur but from this measurement alone it is impossible to state that definitely. Further measurements were performed to prove that in $\text{Cu}^{\text{II}} - \text{Mo}^{\text{V}}$ a spin-flip transition also occurs. Coercive fields are equal to 50 and 300 Oe for $\text{Cu}^{\text{II}} - \text{Mo}^{\text{V}}$ and $\text{Cu}^{\text{II}} - \text{W}^{\text{V}}$, respectively.

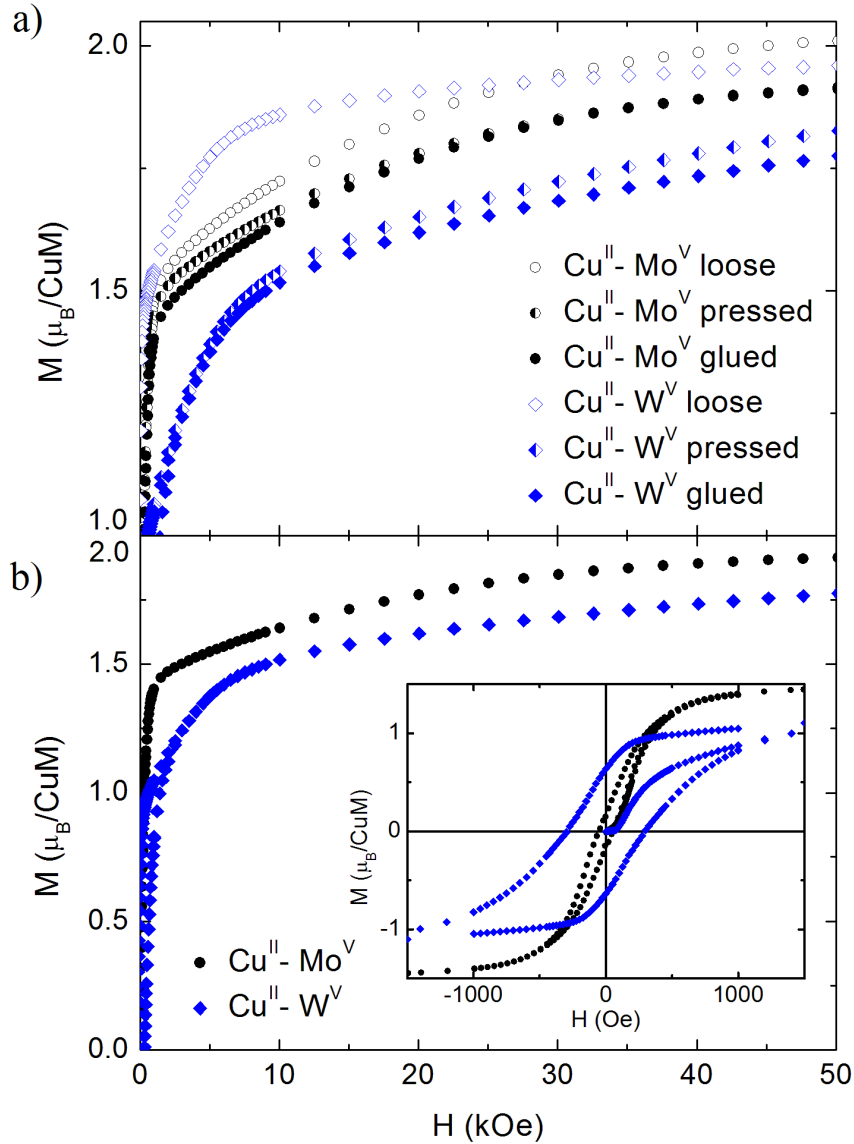


Figure 3.50: a) The magnetization in $T = 2$ K versus field of $\text{Cu}^{\text{II}} - \text{Mo}^{\text{V}}$ and $\text{Cu}^{\text{II}} - \text{W}^{\text{V}}$ for different types of fixing the samples within the gelatine capsule. Loose - pressed loosely within the capsule, pressed: pressed tightly in the capsule, glued: flooded with glue and dried inside the capsule. b) The magnetization versus field of $\text{Cu}^{\text{II}} - \text{Mo}^{\text{V}}$ and $\text{Cu}^{\text{II}} - \text{W}^{\text{V}}$. Inset: hysteresis loops magnified for both the samples.

To determine the existence of the spin-flip transition in $\text{Cu}^{\text{II}} - \text{Mo}^{\text{V}}$ and to investigate it further in both samples, a measurement of magnetization versus field in various temperatures was done for $\text{Cu}^{\text{II}} - \text{Mo}^{\text{V}}$ and $\text{Cu}^{\text{II}} - \text{W}^{\text{V}}$, results presented in fig. 3.51.

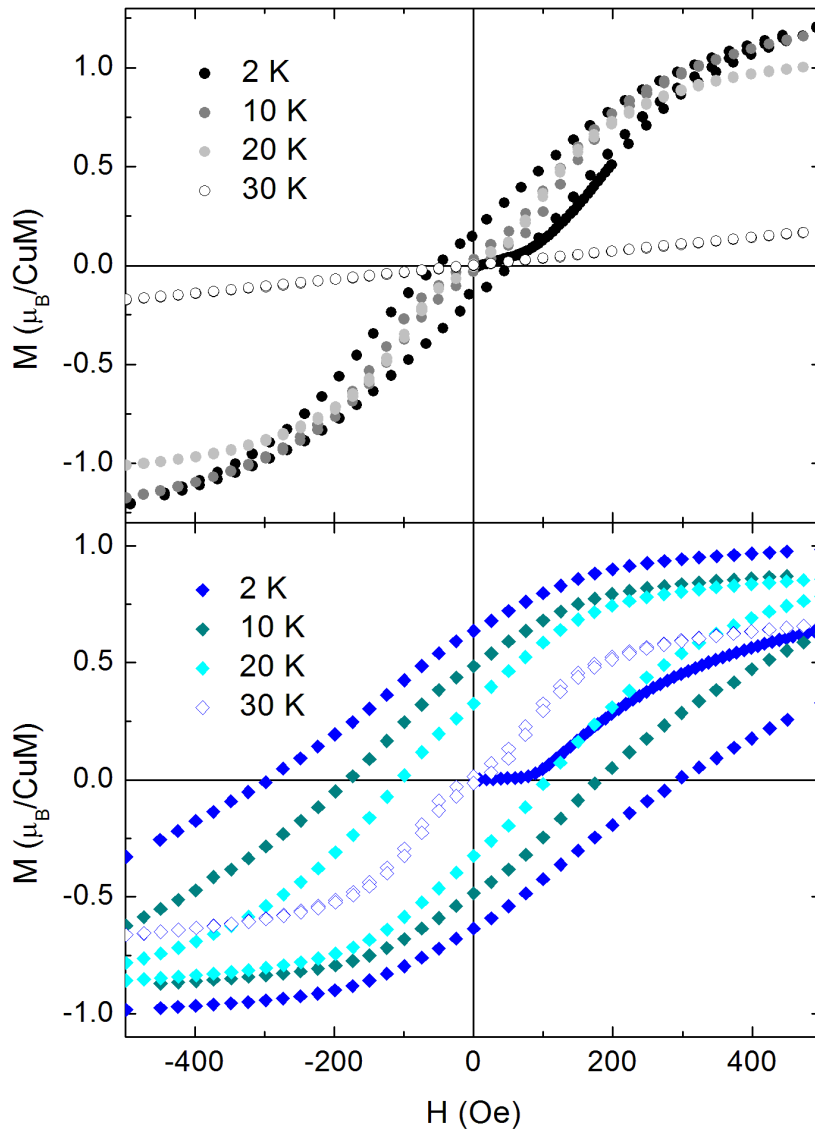


Figure 3.51: Hysteresis measured in temperatures 2, 10, 20 and 30 K for samples $\text{Cu}^{\text{II}} - \text{Mo}^{\text{V}}$ (top) and $\text{Cu}^{\text{II}} - \text{W}^{\text{V}}$ (bottom).

In these temperatures the coercive field is lower, and the spin-flip transition is more visible. Table 3.4 shows the values of the spin-flip field.

T	$H_{\text{sf}}^{\text{Cu-Mo}}$	$H_{\text{sf}}^{\text{Cu-W}}$
10 K	110 Oe	120 Oe
20 K	90 Oe	100 Oe
30 K	—	80 Oe

Table 3.4: The values of the spin-flip field in 10, 20 and 30 K for $\text{Cu}^{\text{II}} - \text{Mo}^{\text{V}}$ and $\text{Cu}^{\text{II}} - \text{W}^{\text{V}}$.

Taking into account that H_{sf} changes with temperature as the saturation magnetisation, the extrapolated to 2 K values of H_{sf} for both compounds are around 120 Oe. For comparison, the value estimated for $\text{Cu}^{\text{II}} - \text{W}^{\text{V}}$ from the $M(H)$ virgin curve at 2 K is 140 Oe.

The spin-flip transition in $\text{Cu}^{\text{II}} - \text{Mo}^{\text{V}}$ was also further investigated using AC technique with various DC fields. The data are shown in fig. 3.52.

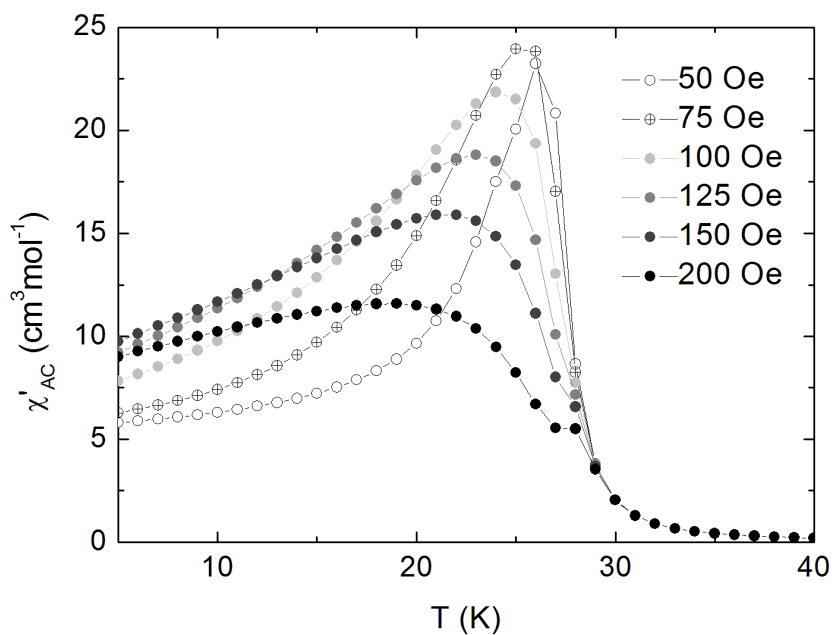


Figure 3.52: AC magnetic susceptibility versus temperature for $\text{Cu}^{\text{II}} - \text{Mo}^{\text{V}}$ in various DC fields. $H_{\text{AC}} = 3$ Oe, $f_{\text{AC}} = 10$ Hz.

The peak in χ' gradually loses its sharpness with the rising DC field value, confirming the existence of the spin-flip transition around 120 Oe.

Further DC measurements in fields below and above the spin-flip transition for both samples were performed, the data presented in fig. 3.53.

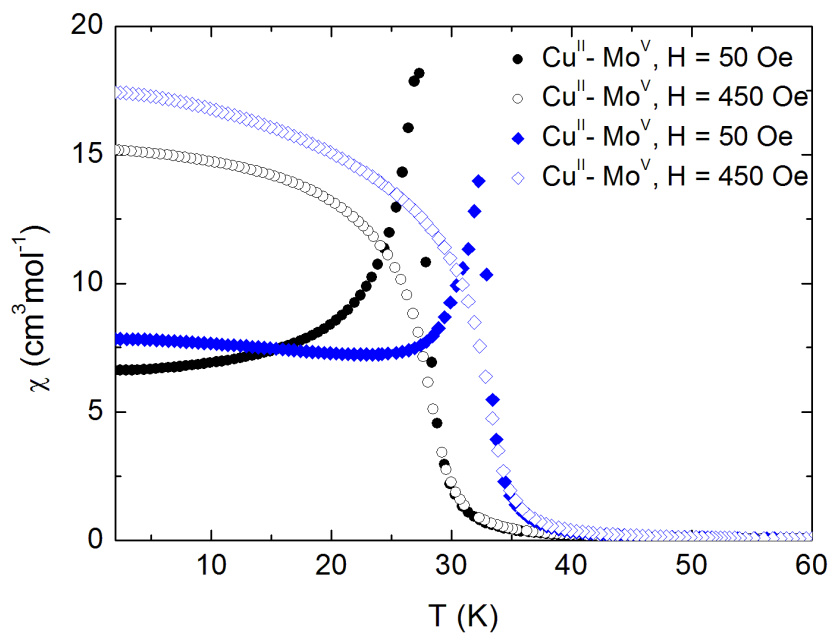


Figure 3.53: DC magnetic susceptibility versus temperature for $\text{Cu}^{\text{II}} - \text{Mo}^{\text{V}}$ and $\text{Cu}^{\text{II}} - \text{W}^{\text{V}}$ in fields below (50 Oe, filled symbols) and above (450 Oe, empty symbols) the spin-flip transition.

The data in 50 Oe show a sharp antiferromagnetic peak, while in 450 Oe it disappears completely for both samples $\text{Cu}^{\text{II}} - \text{Mo}^{\text{V}}$ and $\text{Cu}^{\text{II}} - \text{W}^{\text{V}}$.

3.4.4 Heat capacity measurement for $\text{Cu}^{\text{II}} - \text{Mo}^{\text{V}}$

Experimental

The heat capacity measurement was done in a similar way as in Chapter 3.2.4. Prior to the measurement, the sample was pressed into a small pellet (5 mm in diameter). Unfortunately, it was not possible to produce a strong enough pellet (during several attempts it fell apart into a few grains). Therefore, a grain of suitable size and shape was chosen. The mass of the grain weighed on the laboratory scale was 5.8 mg.

Heat capacity results of $\text{Cu}^{\text{II}} - \text{Mo}^{\text{V}}$ and analysis

The heat capacity was measured in the range 2-150 K in various DC fields. The unprocessed data of molar heat capacity in fields 0, 10, 30 and 90 kOe are presented in fig. 3.54

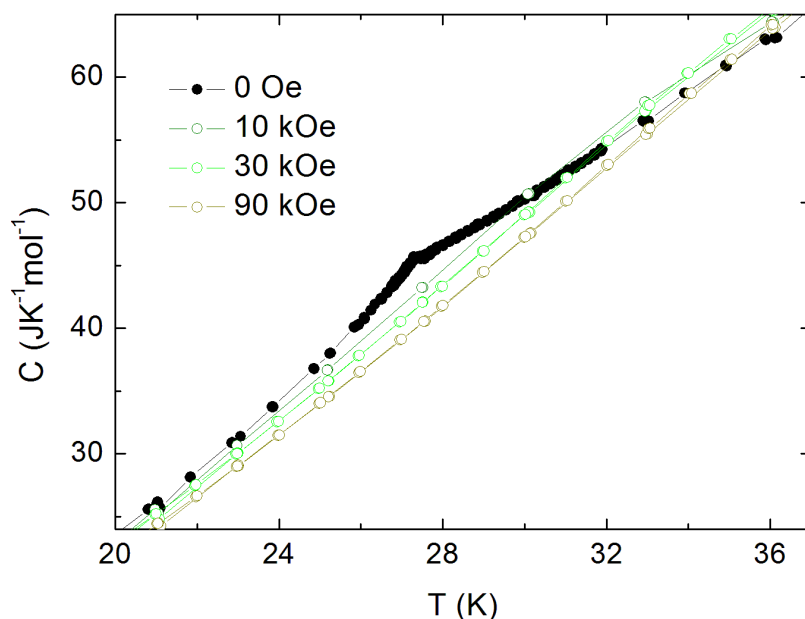


Figure 3.54: Molar heat capacity of $\text{Cu}^{\text{II}} - \text{Mo}^{\text{V}}$ in external fields of 0, 10, 30 and 90 kOe.

An anomaly is visible in 27.4 K in zero field, disappearing completely in the lowest applied field. The position of the anomaly is in agreement with the magnetic ordering of $\text{Cu}^{\text{II}} - \text{Mo}^{\text{V}}$ below 27.5 K.

Debye model was fitted to the data as in chapter 3.2.4 to subtract the phonon heat capacity. The fitting range was 38 - 74 K. The calculated Debye temperature was

206(2) K. The phonon background was subtracted and a plot of the magnetic heat capacity over temperature versus temperature was done to calculate the magnetic entropy gain (fig. 3.55).

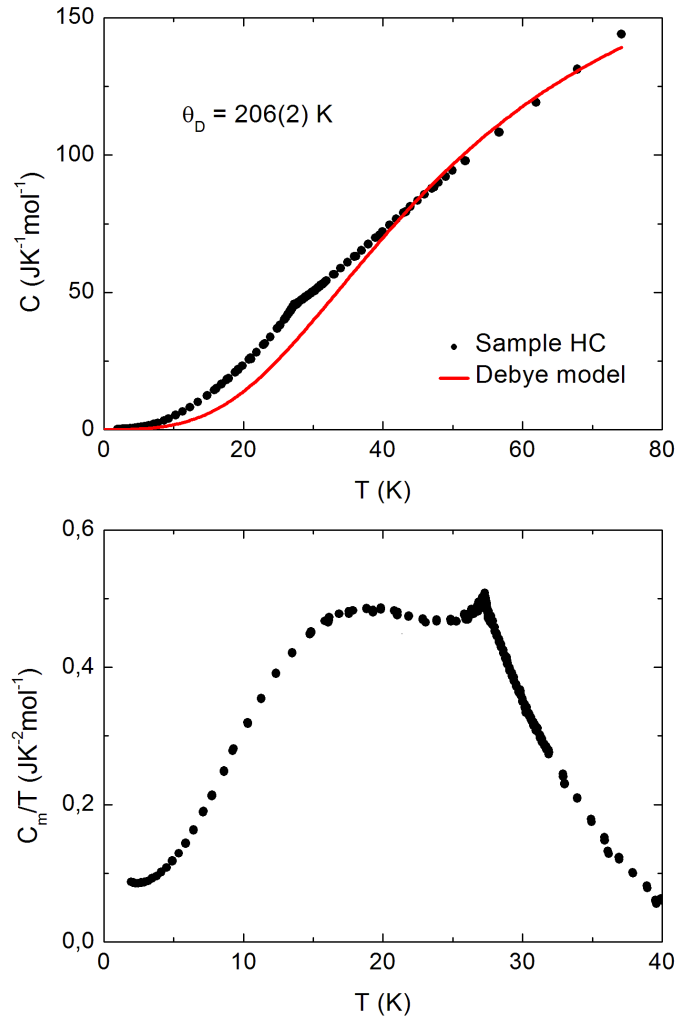


Figure 3.55: Top: molar heat capacity of $\text{Cu}^{\text{II}} - \text{Mo}^{\text{V}}$ in zero magnetic field together with a Debye model fit to the data. Bottom: magnetic heat capacity of $\text{Cu}^{\text{II}} - \text{Mo}^{\text{V}}$ over temperature versus temperature.

The calculated entropy gain (integration of magnetic heat capacity over temperature versus temperature in the range 2-40 K) was $S_{mag} = 12 \text{ JK}^{-1}\text{mol}^{-1}$, which agrees with the expected value $S_{th} = 11.53 \text{ JK}^{-1}\text{mol}^{-1}$. It should be noted that the choice of the fitting range for the Debye model had an impact on the calculated magnetic entropy gain.

3.4.5 Summary

$\text{Cu}^{\text{II}} - \text{M}^{\text{V}}$ assembly with $\text{M} = \text{Mo}, \text{W}$ is a magnetically ordering, double-layer system. The crystal structure suggests strong ferromagnetic interactions within the layers, proven by large and positive Weiss temperatures, while the interactions between separate layers are much weaker and most probably of dipolar character. The zero-field structure reveals 3D antiferromagnetic ordering below T_C , most probably coming from interaction between the layers, which is overcome by low magnetic fields (spin-flip transition around 120 Oe in both compounds). Both the compounds reveal hysteresis loops with coercive fields of values 50 Oe and 300 Oe in 2 K for $\text{Cu}^{\text{II}} - \text{Mo}^{\text{V}}$ and $\text{Cu}^{\text{II}} - \text{W}^{\text{V}}$, respectively. Critical temperatures below which long-range order emerges were found to be $T_C^{\text{CuMo}} = 27.5$ K and $T_C^{\text{CuW}} = 32.8$ K. The heat capacity measurement for $\text{Cu}^{\text{II}} - \text{Mo}^{\text{V}}$ confirms the long-range magnetic ordering, the magnetic heat capacity displaying a λ -shaped peak at 27.4 K.

The results described in this Chapter were published in [35].

3.5 $\text{Cu}_2^{\text{II}} - \text{Mo}^{\text{IV}}$ - a photosensitive magnetic network

3.5.1 Structure

The structure of $[\text{Cu}^{\text{II}}(\text{bapa})]_2[\text{Mo}^{\text{IV}}(\text{CN})_8] \cdot 4\text{H}_2\text{O}$, where bapa is bis-(3-amino-propyl)amine of molecular formula $\text{C}_6\text{H}_{17}\text{N}_3$, a ligand which is an example of linear aliphatic poliamine with three N-donors amine groups separated by two propylen chains. From now on the compound will be called $\text{Cu}_2^{\text{II}} - \text{Mo}^{\text{IV}}$ for short. Its structure is presented in fig. 3.56.

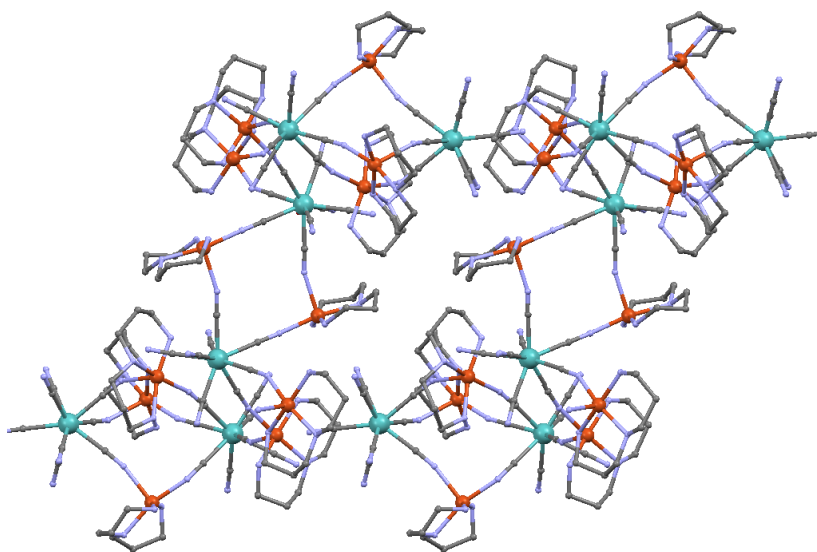


Figure 3.56: The crystal structure of $\text{Cu}_2^{\text{II}} - \text{Mo}^{\text{IV}}$ viewed along crystallographic a axis. colours: Cu - orange, Mo - blue.

Each Mo atom is connected with four Cu atoms, and each Cu atom connects with two Mo atoms. The connections are made through CN bridges. The distances between Cu and Mo centres are between 5.1 and 5.3 Å, while the dimensions of the triclinic unit cell are $a = 15.6$ Å, $b = 16.9$ Å and $c = 24.9$ Å, with angles $\alpha = 102.4^\circ$, $\beta = 91.3^\circ$ and $\gamma = 115.5^\circ$.

3.5.2 Experimental

The sample was obtained by Olaf Stefańczyk.

First, a large powder sample was measured ($m = 43.4$ mg), pressed in a gelatine capsule (Chapter 3.1.2).

The powder samples installed in the FOSH were too small to be weighed on the laboratory scale. Therefore, their mass for each measurement was estimated by comparison of the data before irradiation with the large powder sample data in 2 K and 50 kOe.

3.5.3 Light absorption measurements

Ultraviolet-visible spectroscopy measurements were performed by Olaf Stefańczyk in the Chemistry Department of Jagiellonian University. The absorption curve obtained is presented in fig. 3.57.

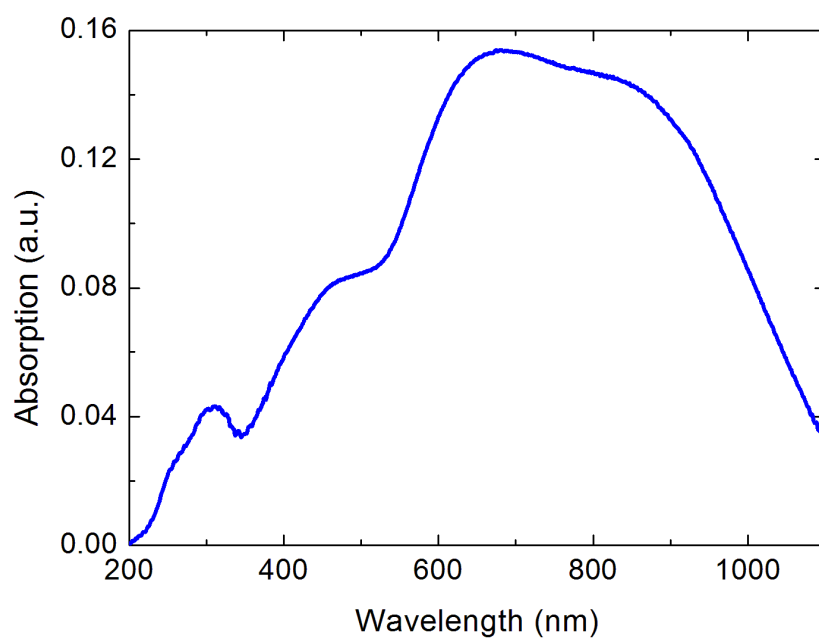


Figure 3.57: UV - visible absorption spectrum for $\text{Cu}_2^{\text{II}} - \text{Mo}^{\text{IV}}$ (courtesy of O. Stefańczyk)

The absorption bands exist around 310, 460, 680 and possibly at 840 nm, which gives an indication which wavelengths can be used during photomagnetic measurements.

3.5.4 Magnetic properties and photomagnetism of $\text{Cu}_2^{\text{II}} - \text{Mo}^{\text{IV}}$

Prior to photomagnetic measurements, magnetization versus temperature in 1 kOe and versus field in 2 K was measured for a powder sample (fig. 3.58). The data from the measurement in 1 kOe were corrected for the capsule contribution.

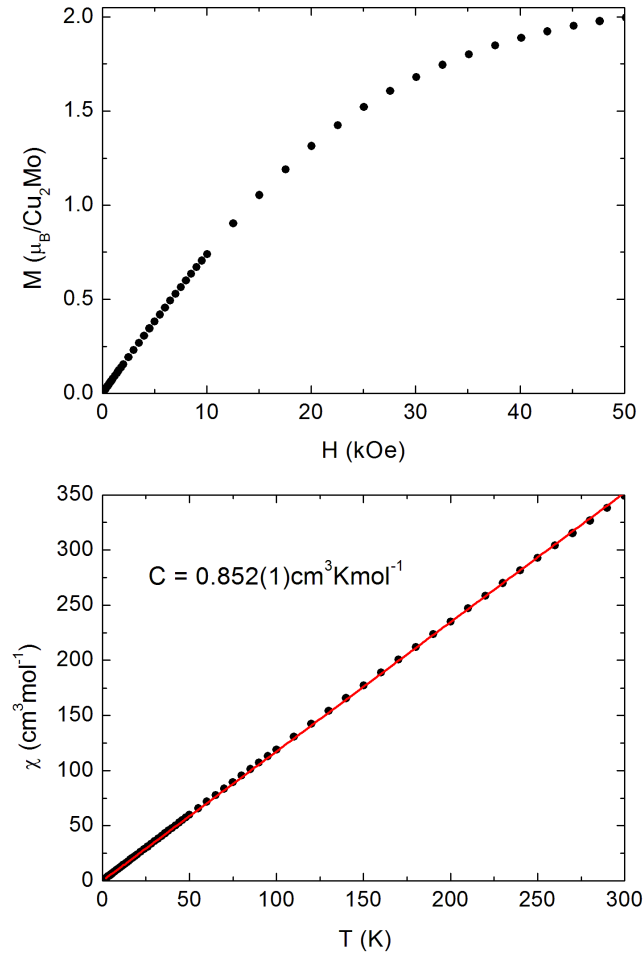


Figure 3.58: Top: magnetization of $\text{Cu}_2^{\text{II}} - \text{Mo}^{\text{IV}}$ versus field in $T = 2$ K. Bottom: reciprocal susceptibility of $\text{Cu}_2^{\text{II}} - \text{Mo}^{\text{IV}}$ in $H = 1$ kOe with a Curie law fit (red line)

As can be clearly seen, $\text{Cu}_2^{\text{II}} - \text{Mo}^{\text{IV}}$ is paramagnetic. If a spin $S_{\text{Cu}^{\text{II}}} = 1/2$ and an isotropic Landé factor $g_{\text{Cu}^{\text{II}}} = 2.2$ is assumed, the predicted Curie constant is $C_{\text{pred}} = 0.825 \text{ cm}^3 \text{ K mol}^{-1}$. It should be noted that Mo^{IV} is non-magnetic ($S_{\text{Mo}^{\text{IV}}} = 0$). The value from the fit $C = 0.852(1) \text{ cm}^3 \text{ K mol}^{-1}$ is slightly larger, but very close to the value reported in [14] for a similar photomagnetic compound. The value of magnetization in 50 kOe and 2 K, $2.0\mu_B$ is lower than the expected

value of $2.2\mu_B$ per mole, but in 50 kOe the saturation value is not reached.

The sample was then placed in the FOSH and preliminary photomagnetic measurements were taken (short time irradiation) to check if any photomagnetic effect takes place for a given wavelength of irradiation. The results of the preliminary tests are presented in fig. 3.59. The drop in the signal is correlated with the beginning of irradiation, the sharp rise - the end of irradiation; when the sample is irradiated, its temperature increases slightly, hence the drop in the magnetization (from these data it can be estimated that the temperature increases by around 2 K).

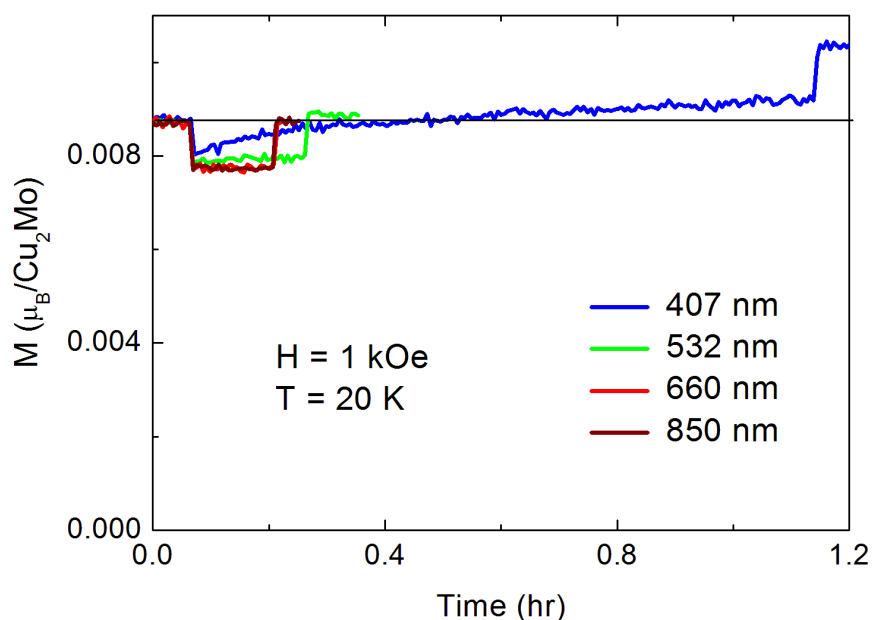


Figure 3.59: Magnetization of $\text{Cu}_2^{\text{II}} - \text{Mo}^{\text{IV}}$ while irradiated with different wavelengths (all measurements taken at 1 kOe and 20K).

From these preliminary irradiations it can be seen that a photomagnetic effect is observed for wavelengths 407 and 532 nm (the latter giving a very small rise of 2% after 12 minutes of irradiation). Therefore, wavelengths of 405, 407, 450 and 532 nm were chosen for further tests with longer irradiation times. The results of all the photomagnetic measurements are gathered in Table 3.5

λ (nm)	H (kOe)	T (K)	t (h)	P (mW)	ΔM (%)
Preliminary irradiations					
407	1	20	1	5	15
532	1	20	0.2	11	2
660	1	20	0.15	10	0
850	1	20	0.15	5	0
Specific measurements					
405	5	15	20	5	20
407	1	20	16	5*	31
450	5	15	12	5	30
532	5	15	5	5	14

Table 3.5: Results of photomagnetic measurements for $\text{Cu}_2^{\text{II}} - \text{Mo}^{\text{IV}}$. P means the estimated power of the light irradiating the sample. ΔM means the rise of the magnetic signal after the irradiation compared with the initial value before the irradiation (highest obtained values in bold). * - lost temperature control of the diode, power may have fluctuated.

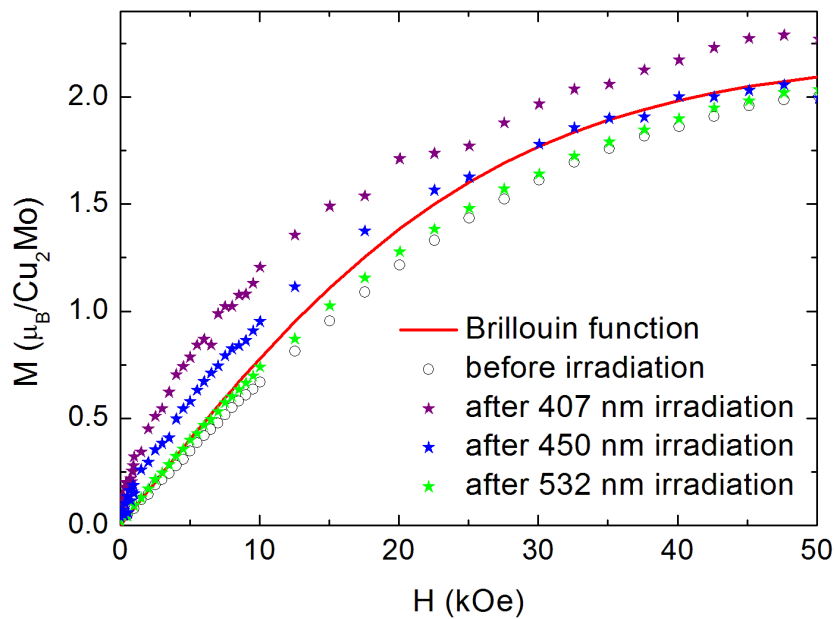


Figure 3.60: Magnetization versus field of $\text{Cu}_2^{\text{II}} - \text{Mo}^{\text{IV}}$ measured in 2 K before and after irradiation with different wavelengths. Brillouin function was added for reference (red line).

Magnetization versus temperature was measured before and after the irradiation (each time the light being turned off during the measurement to avoid the temperature rise). The results are compared in fig. 3.60. Brillouin function for the spin and g factor of Cu^{II} was added for reference.

It is visible that, despite the comparable ΔM for 407 and 450 nm, the largest effect occurs after the irradiation with 407nm, intermediate in the case of 450nm, while for 532nm is almost indistinguishable from the primal curve (fig. 3.60). Despite the large noise in the data, it is visible that the value in 50 kOe does not change significantly, the change is visible rather in the shapes of magnetization curves. Only in the case of 407 nm irradiation, the magnetization after the irradiation reaches the saturation value of $2.2\mu_B$.

The possible explanation for the photomagnetic effect in the case of this compound is Metal-to-metal charge transfer (MMCT) [14] - a photooxidation of Mo^{IV} ($S = 0$) to Mo^{V} ($S = 1/2$) by a transfer of an electron from one of the neighbouring Cu^{II} ($S = 1/2$), reducing it to Cu^{I} , which is diamagnetic ($S = 0$). Therefore, this mechanism does not create extra spins, but a different localization of the magnetic centres. The interactions between Mo^{V} and the remaining Cu^{II} are postulated to be ferromagnetic, not leading to a 3D order because the diamagnetic Cu^{I} atoms are cutting off the interaction paths and/or the irradiation impact is not sufficient to influence all the $\text{Cu}^{\text{II}} - \text{Mo}^{\text{IV}}$ pairs [36]. This finds confirmation in comparison of the $M(H)$ data in 2 K after the irradiation with 407 and 450 nm with the Brillouin function for the paramagnetic Cu^{II} .

The photo-induced magnetization was stable in low temperatures, it was however lost after warming the sample up to room temperature and cooling down again.

3.5.5 Summary

The magnetic and photomagnetic measurements of $\text{Cu}_2^{\text{II}} - \text{Mo}^{\text{IV}}$ revealed a prominent rise in magnetization when irradiated with violet and blue light, the effect decreasing with increasing wavelength. The effect most likely corresponds to the 460 nm absorption band.

The mechanism responsible for this effect is metal-to-metal charge transfer, leading not to creation of any new spins but altering the magnetic structure of the compound and modifying the interactions between the metal centers. The photo-induced magnetization is stable in low temperatures, but the effect is cancelled by heating the sample.

The data presented in this Chapter are largely preliminary and the matter will be investigated further.

Chapter 4

Summary

In this Thesis, magnetic properties of several new molecular transition metals compounds were investigated by means of bulk and single crystal magnetic and heat capacity measurements.

Chiral $\text{Mn}_2^{\text{II}} - \text{Nb}^{\text{IV}}$ was found to be a weakly anisotropic, soft 3D ferrimagnet with ordering temperature of 43 K. During single crystal measurements along three crystallographic directions, $a \equiv b$ were found to be the easy directions for the magnetization, while c is the hard magnetization direction.

$\text{Co}_3^{\text{II}} - \text{W}_2^{\text{V}}$ is a strongly anisotropic, layered molecular magnet with an ordered phase below 6 K. The zero-field structure reveals antiferromagnetic coupling between noncolinear ferromagnetic layers. The compound was found to have one easy magnetization direction, lying in the ac crystallographic plane, forming an angle of 39° with the a crystallographic axis. The b crystallographic axis is the hard magnetization direction. The compound exhibits a spin-flip transition at around 100 Oe applied along the easy direction, the H_{sf} rising further from the easy axis. The magnetic structure of $\text{Co}_3^{\text{II}} - \text{W}_2^{\text{V}}$ was simulated, confirming the experimental findings: noncolinear magnetic structure, magnetization cancelling along b , and the easy axis in the ac plane at the angle 26° with a . The compound was also investigated by heat capacity measurements.

$\text{Ni}_2^{\text{II}} - \text{Nb}^{\text{IV}}$ is a soft ferromagnet, primarily with one single phase ordering below 12 K. This phase is destroyed by dehydration, creating a spin glass-like phase below 4 K. Rehydration restores the primary phase partially and gives rise to an additional phase ordering in 7 K.

$\text{Cu}^{\text{II}} - \text{Mo}^{\text{V}}$ and $\text{Cu}^{\text{II}} - \text{W}^{\text{V}}$ were found to be double-layer systems with ordering temperatures 27.5 and 32.8 K, respectively (for $\text{Cu}^{\text{II}} - \text{Mo}^{\text{V}}$ additionally confirmed by heat capacity measurements). The coercive field is equal to 50 and 300 Oe, respectively. Both of the compounds exhibit a spin-flip transition from

Sample	T_C	Ordering	Coercivity	Spin-flip	Heat capacity	Anisotropy	Special features
$\text{Mn}_2^{\text{II}} - \text{Nb}^{\text{IV}}$	42.6(4) K	ferrimagnetic	-	-	-	weak, $a \equiv b$ easy axes, c hard	MSHG
$\text{Co}_3^{\text{II}} - \text{W}_2^{\text{V}}$	5.94(1) K	ferromagnetic layers antifer- romagnetically coupled	100 Oe along easy axis	around 100 Oe	peak 5.7 K in	strong, easy axis in ac plane, b - hard axis	strong anisotropy
$\text{Ni}_2^{\text{II}} - \text{Nb}^{\text{IV}}$ 1	11.7 K	ferromagnetic	100 Oe	-	-	-	water sensitivity
$\text{Ni}_2^{\text{II}} - \text{Nb}^{\text{IV}}$ 2	< 4 K	spin glass-like	-	-	-	-	water sensitivity
$\text{Ni}_2^{\text{II}} - \text{Nb}^{\text{IV}}$ 3	12 K & 7 K	multi-phase	320 Oe	-	-	-	water sensitivity
$\text{Ni}_2^{\text{II}} - \text{Nb}^{\text{IV}}$ 4	< 4 K	spin glass-like	-	-	-	-	water sensitivity
$\text{Ni}_2^{\text{II}} - \text{Nb}^{\text{IV}}$ 5	12 K & 7 K	multi-phase	110 Oe	-	-	-	water sensitivity
$\text{Cu}^{\text{II}} - \text{Mo}^{\text{V}}$	27.5 K	ferromagnetic layers antifer- romagnetically coupled	50 Oe	around 120 Oe	peak 27.4 K in	-	-
$\text{Cu}^{\text{II}} - \text{W}^{\text{V}}$	32.8 K	ferromagnetic layers antifer- romagnetically coupled	300 Oe	around 120 Oe	-	-	-
$\text{Cu}_2^{\text{II}} - \text{Mo}^{\text{IV}}$	-	paramagnetic	-	-	-	-	photomagnetism

Table 4.1: A brief summary of magnetic properties of all the molecular magnets researched in this work.

antiferro- to ferromagnetic ordering in 120 Oe in 2 K.

$\text{Cu}_2^{\text{II}} - \text{Mo}^{\text{IV}}$, a paramagnetic molecular compound, showed noticeable photo-magnetic effect upon violet and blue light irradiation. The photo-induced magnetization is stable in low temperatures, but the effect is cancelled by heating the sample. Metal-to-metal charge transfer leads to the change in magnetization.

The magnetic properties of all the compounds investigated are gathered in Table 4.1 for comparison.

This Thesis is intended as a set of examples of modern molecular magnets, chosen from over a hundred samples measured by the author, demonstrating the variety of their possible magnetic behaviour and additional means to control the magnetization. It gives an outline on molecular magnets and is a detailed record of experimental approach used in magnetic measurements and can hopefully serve as a help in the interpretation of other magnetic measurements results.

Appendices

Units in Magnetism

There are two systems of units used in magnetism: CGS (centimetre - gram - second), the older units system is more natural for magnetism, and therefore more popular within the magnetism community, and is also used throughout this entire work. However, both systems are widely used, it is therefore important to understand the difference and know the conversion between one and the other.

The basic difference comes from the relation connecting the flux density B , field strength H and magnetization M . In the SI system

$$\vec{B} = \mu_0(\vec{H} + \vec{M}), \quad \mu_0 = 4\pi \cdot 10^{-7} \frac{\text{T} \cdot \text{m}}{\text{A}},$$

so there are different units for B and for H (T (tesla) and A/m, respectively). In CGS:

$$\vec{B} = \vec{H} + 4\pi\vec{M}.$$

The unit for B is G (gauss) and for H is Oe (oersted), but they are dimensionally equal.

The other important quantity, which is the quantity measured in all dc magnetometers, magnetic moment μ , in SI has a unit J/T and in CGS erg/G, which is frequently named 'emu'. Strictly speaking, emu is not a single unit and it has different meanings for different quantities. It is 'electromagnetic unit of magnetization' for magnetization and 'electromagnetic unit of susceptibility' for susceptibility, e.g. $\text{emu/Oe} \rightarrow \text{emu}$ for $M/H \rightarrow \chi$.

The susceptibility $\chi = M/H$ in both systems is dimensionless, but to add a label [8], it is often written 'emu/cm³', which gives the emu the dimensions of cm³. Often, the susceptibility is reported as emu/g and emu/mole, and in this Work emu is replaced by cm³, so it gives the molar susceptibility the dimension of cm³/mole.

All the quantities used in this work, CGS and SI units together with the conversion factors are gathered in Table A.1

Quantity	CGS units	Conv. factor	SI units
Magnetic induction, B	G (gauss)	10^{-4}	T (tesla)
Magnetic field strength, H	Oe (oersted)	$10^3/4\pi$	A/m
Volume magnetization, M	emu/cm ³	10^3	A/m
Volume magnetization, $4\pi M$	G	$10^3/4\pi$	A/m
Magnetic moment, m	emu, erg/G	10^{-3}	A · m ² , J/T
Volume susceptibility, χ	dimensionless, emu/cm ³	4π	dimensionless
Molar susceptibility, χ	cm ³ /mol, emu/mol	$4\pi \cdot 10^{-6}$	m ³ /mol
Demagnetization factor, D, N	dimensionless	$1/4\pi$	dimensionless

Table A.1: Conversion between CGS and SI units for magnetic quantities (source: [37])

Demagnetization

From the experimental point of view, it is important to realize the existence of demagnetization. This correction should be especially considered if the material exhibits strong magnetization.

When a material orders magnetically, uncompensated moments appear on the surface. Therefore, the field H inside the sample depends on its shape. Demagnetization is usually described in terms of so-called *demagnetization field* H_D which results from the separation of hypothetical magnetic charge associated with the sample's magnetization. The total field in the sample can then be described as:

$$H = H_{ext} + H_D \equiv H_{ext} - NM$$

where H_{ext} is the external field applied to the sample, M is sample's magnetization and N is the shape-dependent demagnetization factor. The value of N in CGS can change in the range $0 \leq N \leq 4\pi$. For a long, thin sample with the field applied along its long axis, N is close to zero, while for a short, flat sample in a perpendicular field the demagnetization factor can be close to 4π .

To be able to accurately apply this correction, the demagnetization has to be uniform throughout the sample, which is the case of an ellipsoid. The common practice is to approximate N for a sample by considering the case for an ellipsoid with shape and dimensions allowed to enclose the maximum volume of the sample. Most samples are of different shapes, so this correction is only approximate in most cases [37].

Tables and plots of calculations of the value of N for ellipsoids are widely available [38], [39].

This correction was calculated for the single crystal investigated in Chapter 3.1.

Bibliography

- [1] M. Ruben, *Synthesis of Molecular Magnets*, Institute of Nanotechnology, Research Centre Karlsruhe, Germany [cited on page(s) 5, 6]
- [2] T. Lis, *Preparation, Structure and Magnetic Properties of a Dodecanuclear Mixed-Valence Manganese Carboxylate*, Acta Crystallogr. B, Vol. 36, P. 2042-2046 (1980) [cited on page(s) 5]
- [3] D. Gatteschi, R. Sessoli, *Molecular nanomagnets: the first 10 years*, Journal of Magnetism and Magnetic Materials, 272 - 276, P. 1030 - 1036 (2004) [cited on page(s) 6, 119]
- [4] B. Odom, D. Hanneke, B. D'Urso and G. Gabrielse *New Measurement of the Electron Magnetic Moment Using a One-Electron Quantum Cyclotron*, Phys. Rev. Lett. Vol. 97, P. 030801-1-4 (2006) [cited on page(s) 7]
- [5] O. Kahn, *Molecular Magnetism*, John Wiley & Sons (1993) [cited on page(s) 8, 9, 10, 11, 13, 14, 20]
- [6] G. A. Bain and J. F. Berry, *Diamagnetic Corrections and Pascal's Constants*, J. Chem. Edic., Vol. 85, P. 532-536 (2008) [cited on page(s) 9]
- [7] J. M. D. Coey, *Magnetism and Magnetic Materials*, Cambridge University Press (2010) [cited on page(s) 13, 20]
- [8] Ed. by F. Palacio, E. Ressouche and J. Schweizer, *Introduction to Physical Techniques in Molecular Magnetism*, University of Zaragoza Press (2001) [cited on page(s) 14, 21, 23, 24, 25, 109]
- [9] D. Gignoux, M. Schlenker, *Magnetism Fundamentals*, Springer (2005) [cited on page(s) 16, 17, 18]
- [10] J. A. Mydosh, *Spin Glasses/ An Experimental Introduction*, Taylor & Francis Ltd. (1993) [cited on page(s) 19]

- [11] K. Binder, A. P. Young, *Spin glasses: Experimental facts, theoretical concepts, and open questions*, Reviews of Modern Physics, Vol. 58, P. 801-976 (1986) [cited on page(s) 19]
- [12] M. Sorai, M. Nakano, Y. Miyazaki, *Calorimetric Investigation of Phase Transitions Occurring in Molecule-Based Magnets*, Chem. Rev., Vol. 106, P. 976-1031 (2006) [cited on page(s) 21]
- [13] O. Sato, T. Iyoda, A. Fujishima, K. Hashimoto, *Photoinduced magnetization of a cobalt-iron cyanide*, Science, Vol. 272 P. 704-705 (1996) [cited on page(s) 22]
- [14] G. Rombaut, C. Mathonière, P. Guionneau, S. Golhen, L. Ouahab, M. Verelst, P. Lecante, *Structural and photo-induced magnetic properties of $M_2^{II}[W^{IV}(CN)_8] \cdot x H_2O$ ($M = Fe$ and $x=8$, Cu and $x=5$). Comparison with $Cu_2^{II}[Mo^{IV}(CN)_8] \cdot 7.5 H_2O$* , Inorg. Chim. Acta, Vol. 326, P. 27-36 (2001) [cited on page(s) 22, 98, 101]
- [15] E. Breuning, M. Ruben, J.-M. Lehn, F. Renz, Y. Garcia, V. Ksenofontov, P. Gutlich, E. Wegelius, K. Rissanen, *Spin Crossover in a Supramolecular $Fe_4^{II} [2 \times 2]$ Grid Triggered by Temperature, Pressure and Light*, Angew. Chem., Vol. 39, P. 2054-2057 (2000) [cited on page(s) 22]
- [16] B. D. Josephson, *Possible new effects in superconductive tunneling*, Phys. Lett., Vol. 1, P. 251 (1962) [cited on page(s) 23]
- [17] B. D. Josephson *The discovery of tunneling supercurrents*, Nobel Lecture (1973) [cited on page(s) 23]
- [18] P. Anderson and J. M. Rowell, *Probable observation of the Josephson superconducting tunneling effect*, Phys. Rev. Lett., Vol. 10, P. 230-232 (1963) [cited on page(s) 24]
- [19] R. C. Jaklevic, J. Lambe, A. H. Silver, and J. E. Mercereau, *Quantum interference effects in Josephson tunneling*, Phys. Rev., Lett., Vol. 12, P. 159-160 (1964) [cited on page(s) 25]
- [20] Quantum Design, *MPMS MultiVu Application User's Manual* [cited on page(s) 26]
- [21] Quantum Design, *MPMS Reciprocating Sample Option User's Manual* [cited on page(s) 27]
- [22] D. Martien, *Introduction to: AC susceptibility*, Quantum Design [cited on page(s) 27]
- [23] Quantum Design, *MPMS AC Option User's Manual* [cited on page(s) 27]

- [24] Quantum Design, *The MPMS Horizontal Sample Rotator User's manual 1067-100A* [cited on page(s) 27]
- [25] Quantum Design, *FOSH User's Manual* [cited on page(s) 30]
- [26] Quantum Design, *PPMS Heat Capacity Option User's Manual* (2009) [cited on page(s) 33]
- [27] D. Pinkowicz, R. Podgajny, W. Nitek, M. Rams, A. M. Majcher, T. Nuida, S. Ohkoshi and B. Sieklucka, *Multifunctional Magnetic Molecular $\{[\text{Mn}^{\text{II}}(\text{urea})_2(\text{H}_2\text{O})]_2[\text{Nb}^{\text{IV}}(\text{CN})_8]\}_n$ System: Magnetization-Induced SHG in the Chiral Polymorph*, Chem. Mater., Vol. 23, P. 21-31 (2011) [cited on page(s) 35, 44, 50]
- [28] S. Chorąży, R. Podgajny, A. M. Majcher, W. Nitek, M. Rams, E. A. Sutura, L. Ungur, L. F. Chibotaruc and B. Sieklucka, *Magnetic anisotropy of Co^{II} - W^{V} ferromagnet: single crystal and ab initio study*, Cryst. Eng. Comm., Vol. 15, P. 2378-2385 (2013) [cited on page(s) 51, 67, 73]
- [29] P. M. Kiernan and W. P. Griffith, J. Chem.Soc., *Studies on transition-metal cyano-complexes. Part I. Octacyanonioabates(III), -nioabates(IV), -molybdates(V), and -tungstates(V)*, Dalton Trans., P. 2489-2494 (1975) [cited on page(s) 55]
- [30] F. Lloret, M. Julve, J. Cano, R. Ruiz-García, E. Pardo, *Magnetic properties of six-coordinated high-spin cobalt(II) complexes: Theoretical background and its application*, Inorg. Chim. Acta, Vol. 361, P. 3432-3445 (2008) [cited on page(s) 55, 71]
- [31] E. Gopal, *Specific Heats At Low Temperatures*, Plenum Press (1966) [cited on page(s) 71]
- [32] B. Nowicka, M. Rams, K. Stadnicka and B. Sieklucka, *Reversible Guest-Induced Magnetic and Structural Single-Crystal-to-Single-Crystal Transformation in Microporous Coordination Network $\{[\text{Ni}(\text{cyclam})]_3[\text{W}(\text{CN})_8]_2\}_n$* , Inorganic Chem. Comm., Vol. 46, P. 8123-8125 (2007) [cited on page(s) 74]
- [33] B. Nowicka, M. Bałanda, B. Gaweł, G. Ćwiak, A. Budziak, W. Łasocha and B. Sieklucka, *Microporous $\{[\text{Ni}(\text{cyclam})]_3[\text{W}(\text{CN})_8]_2\}_n$ affording reversible structural and magnetic conversions*, Dalton Trans., Vol. 40, P. 3067-3073 (2011) [cited on page(s) 74]
- [34] B. Nowicka, M. Bałanda, M. Reczyński, A. M. Majcher, M. Koziel, W. Nitek, W. Łasocha, B. Sieklucka, *A water sensitive ferromagnetic $[\text{Ni}(\text{cyclam})]_2[\text{Nb}(\text{CN})_8]$ network*, Dalton Trans., Vol. 42, P. 2616-2621 (2013) [cited on page(s) 74, 82]

- [35] O. Stefańczyk, A. M. Majcher, M. Rams, W. Nitek, M. Koziel, W. Łasocha and B. Sieklucka, *Incorporation of guanidinium ions in $\text{Cu}^{\text{II}}\text{-}[\text{M}^{\text{V}}(\text{CN})_8]^{3-}$ double-layered magnetic systems*, Dalton Trans., Vol. 42, P. 5042-5046 (2013) [cited on page(s) 83, 95]
- [36] G. Rombaut, M. Verelst, S. Golhen, L. Ouahab, C. Mathonière, and O. Kahn, *Structural and Photomagnetic Studies of Two Compounds in the System $\text{Cu}^{2+}/\text{Mo}(\text{CN})_8^{(4-)}$: From Trinuclear Molecule to Infinite Network*, Inorg. Chem., Vol. 40, P. 1151-1159 (2001) [cited on page(s) 101]
- [37] M. McElfresh, *Fundamentals of Magnetism and Magnetic Measurements*, Purdue University, Quantum Design (1994) [cited on page(s) 110, 111, 125]
- [38] J. Osborn, *Demagnetizing factors of the General Ellipsoid*, Phys. Rev., Vol. 67, P. 351-357 (1945) [cited on page(s) 111]
- [39] E. C. Stoner, *The demagnetizing factors for ellipsoids*, Phil. Mag., Vol. 36, P. 803-821 (1945) [cited on page(s) 111]

List of all publications of the author

1. J. Kjelstrup-Hansen, P. Bøggild, J. Hvam, **A. Majcher**, and H.-G. Rubahn, *Micromanipulation of organic nanofibers for blue light emitting microstructures*, phys. stat. sol. (a), Vol. 203, P. 1459 - 1463 (2006)
2. D. Pinkowicz, R. Pełka, O. Drath, W. Nitek, M. Bałanda, **A. M. Majcher**, G. Poneti, and B. Sieklucka, *Nature of Magnetic Interactions in 3D $\{[M^{II}(\text{pyrazole})_4]_2[\text{Nb}^{IV}(\text{CN})_8] \cdot 4H_2O\}_n$ (M = Mn, Fe, Co, Ni) Molecular Magnets*, Inorg. Chem., Vol. 49, P. 7565 - 7576 (2010)
3. R. Pełka, D. Pinkowicz, O. Drath, M. Bałanda, M. Rams, **A. Majcher**, W. Nitek, and B. Sieklucka, *Octacyanonioabate(IV)-based molecular magnets revealing 3D long-range order*, Journal of Physics: ConferenceSeries, Vol. 303 (2011), Joint European Magnetic Symposia 2010 proceedings
4. D. Pinkowicz, R. Podgajny, W. Nitek, M. Rams, **A. M. Majcher**, T. Nuida, S. Ohkoshi, and B. Sieklucka, *Multifunctional Magnetic Molecular $\{[\text{Mn}^{II}(\text{urea})_2(\text{H}_2\text{O})]_2[\text{Nb}^{IV}(\text{CN})_8]\}_n$ System: Magnetization-Induced SHG in the Chiral Polymorph*, Chem. Mater., Vol. 23, P. 21-31 (2011)
5. T. Korzeniak, B. Nowicka, K. Stadnicka, W. Nitek, **A. M. Majcher**, and B. Sieklucka, *Construction of CN^- -bridged molecular squares employing penta-, hexa- and octa-coordinated metal ions*, Polyhedron, Vol. 52, P. 442-447 (2013)
6. R. Podgajny, S. Chorazy, W. Nitek, M. Rams, **A. M. Majcher**, B. Marszałek, J. Żukrowski, C. Kapusta, and B. Sieklucka, *Co-NC-W and Fe-NC-W Electron-Transfer Channels for Thermal Bistability in Trimetallic $\{\text{Fe}_6\text{Co}_3[\text{W}(\text{CN})_8]_6\}$ Cyanido-Bridged Cluster*, Angew. Chem. Int. Ed., Vol. 52, P. 896 - 900 (2013)

7. B. Nowicka, M. Bałanda, M. Reczyński, **A. M. Majcher**, M. Koziel, W. Nitek, W. Łasocha, and B. Sieklucka, *A water sensitive ferromagnetic [Ni(cyclam)]₂[Nb(CN)₈] network*, Dalton Trans., Vol. 42, P. 2616-2621 (2013)
8. S. Chorąży, R. Podgajny, **A. M. Majcher**, W. Nitek, M. Rams, E. A. Sutura, L. Ungur, L. F. Chibotaruc, and B. Sieklucka, *Magnetic anisotropy of Co^{II} - W^V ferromagnet: single crystal and ab initio study*, Cryst. Eng. Comm., Vol. 15, P. 2378-2385 (2013)
9. O. Stefańczyk, **A. M. Majcher**, M. Rams, W. Nitek, M. Koziel, W. Łasocha, and B. Sieklucka, *Incorporation of guanidinium ions in Cu^{II}-[M^V(CN)₈]³⁻ double-layered magnetic systems*, Dalton Trans., Vol. 42, P. 5042-5046 (2013)

List of Figures

1.1	A schematic picture of the first historic molecular magnet, Mn_{12}Ac . Source: [3]	6
1.2	A schematic drawing of the field-induced magnetic moments in a purely diamagnetic substance, the macroscopic magnetization versus field, magnetization versus temperature and inverse magnetic susceptibility versus temperature.	9
1.3	A schematic drawing of the spin alignment in a paramagnetic substance without (left) and with applied magnetic field (right), together with the macroscopic magnetization versus field, magnetization versus temperature and inverse magnetic susceptibility versus temperature which obeys the Curie law.	12
1.4	A schematic drawing of the spin alignment in a ferromagnetic substance, together with the macroscopic magnetization versus field in different temperatures, magnetization versus temperature and inverse magnetic susceptibility versus temperature which obeys the Curie-Weiss law above T_C	15
1.5	A schematic drawing of a typical ferromagnetic hysteresis loop close to $T = 0$ K. H_C - coercivity field, M_R - remnant magnetization.	15
1.6	A schematic drawing of the spin alignment in an antiferromagnetic substance, together with the macroscopic magnetization versus field in different temperatures, magnetization versus temperature and inverse magnetic susceptibility versus temperature which obeys the Curie-Weiss law above T_N	16
1.7	A schematic drawing of the spin alignment in a ferrimagnetic substance at $T = 0$, together with the macroscopic magnetization versus field in different temperatures, magnetization versus temperature (two typical cases in red and green) and inverse magnetic susceptibility.	18

1.8	Example behaviour of magnetization curves of an anisotropic crystal when field is applied along easy (green) and hard (red) magnetization directions.	20
2.1	A scheme of a Josephson junction.	24
2.2	A scheme of a DC SQUID.	25
2.3	A scheme of a SQUID magnetometer	26
2.4	Photos of the Horizontal Sample Rotator for MPMS.	28
2.5	The magnetic signal from the Horizontal Sample Rotator versus rotation angle in chosen temperatures and fields.	29
2.6	A scheme of the Fiberoptic Sample Holder (FOSH).	30
2.7	A scheme of a sample holder for heat capacity measurements in the PPMS system.	32
3.1	a) packing diagrams of $\text{Mn}_2^{\text{II}} - \text{Nb}^{\text{IV}}$ showing herringbone-like arrangement (urea, terminal cyanides and aqualigands omitted for clarity), b) "local" fragments of the structure.	36
3.2	Fragments of structure of $\text{Mn}_2^{\text{II}} - \text{Nb}^{\text{IV}}$ showing coordination spheres of a) Nb, b) Mn1 and c) Mn2 and the 6:3 connectivity type with the presence of six and three bridging cyanides per Nb^{IV} and Mn_2^{II} , respectively	36
3.3	Fragments of structure of $\text{Mn}_2^{\text{II}} - \text{Nb}^{\text{IV}}$ showing the chirality of the compound along the c axis, viewed along b and a crystallographic axes.	37
3.4	Temperature dependence of the magnetic contribution of a gelatine capsule used as a holder for the powder measurements. Measurement was taken at 1 kOe.	38
3.5	Field dependence of the magnetic contribution of a gelatine capsule used as a holder for the powder measurements. Measurement was taken at 300 K.	38
3.6	Photography of the top-cut pyramidal-shaped single crystal sample of $\text{Mn}_2^{\text{II}} - \text{Nb}^{\text{IV}}$ used for magnetic measurements. The size of the grid on which the crystal was photographed is 1mm.	39
3.7	Method of placing the single crystal sample in the holder for MPMS measurements.	40
3.8	Magnetic signal in 300 K in emu versus field measured for a large piece of plastic used as a holder for the single crystal sample.	40
3.9	Inverse magnetic susceptibility of a powder sample of $\text{Mn}_2^{\text{II}} - \text{Nb}^{\text{IV}}$ measured at $H = 1$ kOe. The blue line represents a Curie-Weiss fit to the data above 120 K. The red line is a fit of a simple ferrimagnet model above 120 K (see text). The mass of the sample used was 20.8 mg.	41

3.10	Zero-field cooling/field cooling curves of a powder sample of $\text{Mn}_2^{\text{II}} - \text{Nb}^{\text{IV}}$ measured at around 10 Oe.	42
3.11	AC measurement of a powder sample of $\text{Mn}_2^{\text{II}} - \text{Nb}^{\text{IV}}$ measured at $H_{AC} = 3$ Oe.	43
3.12	Magnetization field dependence of a powder sample of $\text{Mn}_2^{\text{II}} - \text{Nb}^{\text{IV}}$ measured at 2 K. The dashed line represents the level $M = 9\mu_B$	44
3.13	Magnetization field dependence of the single crystal sample of $\text{Mn}_2^{\text{II}} - \text{Nb}^{\text{IV}}$ measured at room temperature for field parallel to a and c crystallographic directions to test for ferromagnetic contamination. The straight line represents a linear fit to the data.	45
3.14	Magnetization field dependence of a single crystal sample of $\text{Mn}_2^{\text{II}} - \text{Nb}^{\text{IV}}$ measured at 2 and 30 K, for field parallel to a and c crystallographic directions.	46
3.15	Zero-field cooling/field cooling magnetization versus temperature curves measured for a single crystal sample of $\text{Mn}_2^{\text{II}} - \text{Nb}^{\text{IV}}$ for field parallel to a and c crystallographic directions. $H = 10$ Oe.	47
3.16	AC susceptibility versus temperature of a single crystal sample of $\text{Mn}_2^{\text{II}} - \text{Nb}^{\text{IV}}$ for field $H_{AC} = 3$ Oe parallel to a and c crystallographic directions. $f_{AC} = 10$ Hz.	48
3.17	Magnetization versus temperature for a single crystal sample of $\text{Mn}_2^{\text{II}} - \text{Nb}^{\text{IV}}$, a) in four different external fields applied along a axis, b) in fields 100 Oe and 1000 Oe applied along a and c axes.	49
3.18	A formula unit of $\text{Co}_3^{\text{II}} - \text{W}_2^{\text{V}}$. colours: Co(II) (dark blue), W(V) (brown), C and N (green), O (yellow). Hydrogen atoms and crystallized water molecules are omitted for clarity.	51
3.19	The crystal structure of $\text{Co}_3^{\text{II}} - \text{W}_2^{\text{V}}$ along a) c crystallographic axis and b) a crystallographic axis. Colours: Co(II) (dark blue), W(V) (brown), C and N (green), O (yellow). Hydrogen atoms (a) and b)) and crystallized water molecules (b)) are omitted for clarity.	52
3.20	The method of placing the cuboidal $\text{Co}_3^{\text{II}} - \text{W}_2^{\text{V}}$ monocrystal inside the straw used for magnetic measurements with magnetic field along a , b and c crystallographic axes (situation I, II and III, respectively)	54
3.21	A scheme of placing the cuboidal $\text{Co}_3^{\text{II}} - \text{W}_2^{\text{V}}$ monocrystal inside the Horizontal Sample Rotator used for measurements of magnetization versus angle between external field and a (or c) crystallographic axis. Vertical movement (blue) of a thin wire (orange) wound around the rod (transparent for better visibility), on which the sample holder rests, causes angular movement of the sample (green).	54
3.22	Inverse susceptibility of the powder sample of $\text{Co}_3^{\text{II}} - \text{W}_2^{\text{V}}$ versus temperature together with a fit of the Curie-Weiss law (red line) in the range of temperatures 150-300 K.	55

3.23	Zero-field cooling - field cooling magnetization of the powder sample of $\text{Co}_3^{\text{II}} - \text{W}_2^{\text{V}}$ versus temperature. $H = 10$ Oe. The solid lines are to guide the eye.	56
3.24	AC measurement of the powder sample of $\text{Co}_3^{\text{II}} - \text{W}_2^{\text{V}}$ versus temperature. $f_{AC} = 10$ Hz and $H_{AC} = 3$ Oe.	57
3.25	Magnetization of the powder sample of $\text{Co}_3^{\text{II}} - \text{W}_2^{\text{V}}$ versus applied field in 2 K. Inset: magnification of the data in the 0-500 Oe range.	58
3.26	Magnetic susceptibility of the powder sample of $\text{Co}_3^{\text{II}} - \text{W}_2^{\text{V}}$ versus temperature in various fields: 4, 24, 100, 300 and 1000 Oe.	59
3.27	Magnetization of a single crystal sample of $\text{Co}_3^{\text{II}} - \text{W}_2^{\text{V}}$ versus field at 2 K along a , b , and c crystallographic axes.	60
3.28	Magnetization of a single crystal sample of $\text{Co}_3^{\text{II}} - \text{W}_2^{\text{V}}$ versus field at 2K along a , b and c crystallographic axes in the field range between -1000 and 1000 Oe.	61
3.29	AC susceptibility of a single crystal sample of $\text{Co}_3^{\text{II}} - \text{W}_2^{\text{V}}$ versus temperature along a , b and c crystallographic axes. $H_{AC} = 3$ Oe, $f_{AC} = 10$ Hz.	62
3.30	Magnetic susceptibility of a single crystal sample of $\text{Co}_3^{\text{II}} - \text{W}_2^{\text{V}}$ versus temperature measured at fields of 10, 30, 100, 300 and 1000 Oe, along a (top), b (middle) and c (bottom) crystallographic directions. The data for $H \parallel b$ are shifted due to a small ferromagnetic impurity visible in this scale.	63
3.31	Magnetization of a single crystal sample of $\text{Co}_3^{\text{II}} - \text{W}_2^{\text{V}}$ versus angle of rotation around the b crystallographic axis taken at $H = 1$ kOe. Line: fit of $M = M_0 \sin(\alpha - \alpha_0) $ to the data.	64
3.32	Magnetization of a single crystal sample of $\text{Co}_3^{\text{II}} - \text{W}_2^{\text{V}}$ in 2 K versus field measured along easy and hard magnetization axes found by the means of Horizontal Sample Rotator. Magnetization along a , b and c crystallographic directions added for reference (empty points).	65
3.33	Magnetization of a single crystal sample of $\text{Co}_3^{\text{II}} - \text{W}_2^{\text{V}}$ in 2 K versus field along the easy magnetization axis in the field range -500 to 500 Oe. Magnetization along a , b and c crystallographic directions added for reference (empty points).	66
3.34	The magnetic structure of $\text{Co}_3^{\text{II}} - \text{W}_2^{\text{V}}$	69
3.35	The placing of the polycrystalline sample of $\text{Co}_3^{\text{II}} - \text{W}_2^{\text{V}}$ on the sample platform.	70
3.36	Molar heat capacity of a polycrystal sample of $\text{Co}_3^{\text{II}} - \text{W}_2^{\text{V}}$ in different magnetic fields. The solid lines are to guide the eye.	71
3.37	Molar heat capacity of a polycrystalline sample of $\text{Co}_3^{\text{II}} - \text{W}_2^{\text{V}}$ in zero magnetic field with Debye fit in the range 26-40 K.	72
3.38	Method of placing $\text{Ni}_2^{\text{II}} - \text{Nb}^{\text{IV}}$ powder samples inside an MPMS holder. 75	75

3.39	Zero-field cooling/field cooling magnetic susceptibility of samples 1-5 versus temperature. Inset: magnification of the data for samples 2, 4 and 5 . $H = 20$ Oe. The solid lines are to guide the eye.	76
3.40	Top: AC in-phase susceptibility of samples 1, 3, 4 and 5 versus temperature. Inset: magnification of the data for samples 3, 4 and 5 . Bottom: AC out-of-phase susceptibility of samples 1, 3, 4 and 5 versus temperature. Inset: magnification of the data for samples 3, 4 and 5 . The solid lines are to guide the eye.	77
3.41	Magnetic susceptibility in 1 kOe versus temperature for samples 1-5 (top) with derivatives of the susceptibility along with Lorentzian fits (bottom). $d\chi/dT$ was multiplied by a factor of 10 for samples 2 and 4 for better visibility.	78
3.42	Magnetic susceptibility times temperature versus temperature for samples 1-5 . Inset: high temperature data with the expected value (red line).	79
3.43	Magnetization of samples 1-5 versus field in $T = 2$ K. Sum of Brillouin functions for this spin configuration added for reference (red line). . .	81
3.44	Magnetization of samples 1-5 versus field in $T = 2$ K (magnified in the range -2 to 2 kOe). The solid lines are to guide the eye. Inset: magnification of the data for samples 2 and 4	81
3.45	The structure of $\text{Cu}^{\text{II}} - \text{Mo}^{\text{V}}$ and $\text{Cu}^{\text{II}} - \text{W}^{\text{V}}$ (viewed along b). Colours: Cu^{II} ions - orange, M^{V} ($= \text{W}^{\text{V}}$ or Mo^{V}) - blue.	83
3.46	Comparison of reciprocal susceptibilities versus temperature for samples $\text{Cu}^{\text{II}} - \text{Mo}^{\text{V}}$ and $\text{Cu}^{\text{II}} - \text{W}^{\text{V}}$ measured at fields 1, 3 and 5 kOe. Inverse of the subtracted susceptibility of 5 and 3 kOe added for comparison (empty symbols).	85
3.47	Reciprocal subtracted susceptibilities versus temperature for samples $\text{Cu}^{\text{II}} - \text{Mo}^{\text{V}}$ and $\text{Cu}^{\text{II}} - \text{W}^{\text{V}}$ with the fits of the Curie-Weiss law in the range 200-300 K.	85
3.48	Magnetic zero-field cooling/field-cooling susceptibility for samples $\text{Cu}^{\text{II}} - \text{Mo}^{\text{V}}$ and $\text{Cu}^{\text{II}} - \text{W}^{\text{V}}$. $H = 20$ Oe.	86
3.49	AC magnetic susceptibility versus temperature for samples $\text{Cu}^{\text{II}} - \text{Mo}^{\text{V}}$ and $\text{Cu}^{\text{II}} - \text{W}^{\text{V}}$: a) in-phase susceptibility, b) out-of-phase susceptibility. $H_{AC} = 3$ Oe and $f_{AC} = 10$ Hz.	87
3.50	a) The magnetization in $T = 2$ K versus field of $\text{Cu}^{\text{II}} - \text{Mo}^{\text{V}}$ and $\text{Cu}^{\text{II}} - \text{W}^{\text{V}}$ for different types of fixing the samples within the gelatine capsule. Loose - pressed loosely within the capsule, pressed: pressed tightly in the capsule, glued: flooded with glue and dried inside the capsule. b) The magnetization versus field of $\text{Cu}^{\text{II}} - \text{Mo}^{\text{V}}$ and $\text{Cu}^{\text{II}} - \text{W}^{\text{V}}$. Inset: hysteresis loops magnified for both the samples.	89

3.51	Hysteresis measured in temperatures 2, 10, 20 and 30 K for samples $\text{Cu}^{\text{II}} - \text{Mo}^{\text{V}}$ (top) and $\text{Cu}^{\text{II}} - \text{W}^{\text{V}}$ (bottom).	90
3.52	AC magnetic susceptibility versus temperature for $\text{Cu}^{\text{II}} - \text{Mo}^{\text{V}}$ in various DC fields. $H_{AC} = 3$ Oe, $f_{AC} = 10$ Hz.	91
3.53	DC magnetic susceptibility versus temperature for $\text{Cu}^{\text{II}} - \text{Mo}^{\text{V}}$ and $\text{Cu}^{\text{II}} - \text{W}^{\text{V}}$ in fields below (50 Oe, filled symbols) and above (450 Oe, empty symbols) the spin-flip transition.	92
3.54	Molar heat capacity of $\text{Cu}^{\text{II}} - \text{Mo}^{\text{V}}$ in external fields of 0, 10, 30 and 90 kOe.	93
3.55	Top: molar heat capacity of $\text{Cu}^{\text{II}} - \text{Mo}^{\text{V}}$ in zero magnetic field together with a Debye model fit to the data. Bottom: magnetic heat capacity of $\text{Cu}^{\text{II}} - \text{Mo}^{\text{V}}$ over temperature versus temperature.	94
3.56	The crystal structure of $\text{Cu}_2^{\text{II}} - \text{Mo}^{\text{IV}}$ viewed along crystallographic a axis. colours: Cu - orange, Mo - blue.	96
3.57	UV - visible absorption spectrum for $\text{Cu}_2^{\text{II}} - \text{Mo}^{\text{IV}}$ (courtesy of O. Stefańczyk)	97
3.58	Top: magnetization of $\text{Cu}_2^{\text{II}} - \text{Mo}^{\text{IV}}$ versus field in $T = 2$ K. Bottom: reciprocal susceptibility of $\text{Cu}_2^{\text{II}} - \text{Mo}^{\text{IV}}$ in $H = 1$ kOe with a Curie law fit (red line)	98
3.59	Magnetization of $\text{Cu}_2^{\text{II}} - \text{Mo}^{\text{IV}}$ while irradiated with different wavelengths (all measurements taken at 1 kOe and 20K).	99
3.60	Magnetization versus field of $\text{Cu}_2^{\text{II}} - \text{Mo}^{\text{IV}}$ measured in 2 K before and after irradiation with different wavelengths. Brillouin function was added for reference (red line).	100

List of Tables

3.1	Calculated magnetic moments of $\text{Co}_3^{\text{II}} - \text{W}_2^{\text{V}}$ along a , b^* and c crystallographic directions.	68
3.2	Critical temperatures in samples 1-5 with the probable distinction of phases.	79
3.3	Curie-Weiss temperatures, Curie constants and probable diamagnetic contributions of samples 1-5	80
3.4	The values of the spin-flip field in 10, 20 and 30 K for $\text{Cu}^{\text{II}} - \text{Mo}^{\text{V}}$ and $\text{Cu}^{\text{II}} - \text{W}^{\text{V}}$	91
3.5	Results of photomagnetic measurements for $\text{Cu}_2^{\text{II}} - \text{Mo}^{\text{IV}}$. P means the estimated power of the light irradiating the sample. ΔM means the rise of the magnetic signal after the irradiation compared with the initial value before the irradiation (highest obtained values in bold). * - lost temperature control of the diode, power may have fluctuated. . .	100
4.1	A brief summary of magnetic properties of all the molecular magnets researched in this work.	104
A.1	Conversion between CGS and SI units for magnetic quantities (source: [37])	110